ECAP-2020-011

Design and characterization of a portable Talbot interferometer for imaging high energy density experiments

Master's Thesis in Physics

Presented by
Stephan Schreiner
03 November 2020

Erlangen Centre for Astroparticle Physics
Department of Physics
Friedrich-Alexander-Universität Erlangen-Nürnberg

Supervisor: Prof. Dr. Gisela Anton

Contents

Contents 2

1 Scientific case 3

2 Fundamentals and methods 4
2.1 Interaction of x-ray radiation with matter 4
2.2 X-ray sources and detection 9
2.2.1 X- ray tubes and backlighters 9
2.2.2 Detection of x-rays with scintillation detectors and imaging plates . 9
2.3 Grating based interferometry 11
2.3.1 The Talbot effect and interferometry 11
2.3.2 Image retrieval, the moiré effect 15
2.3.3 Image reconstruction 19

3 Design of the interferometer 25
3.1 Classification and goal of the experimental setup 25
3.2 Mechanical required specifications 28
3.3 Theory based specifications 29
3.4 Conceptualization 32
3.5 Concluding remarks and outlook 40

4 Characterization of the interferometer 42
4.1 Evaluating possible grating combinations 42
4.2 Curved grating frames 47
4.3 Comparing reconstruction methods 51
4.4 Optimizing the visibility of the moiré fringes 59
4.5 Area of reconstruction and the impact on the reconstructed images 63

5 Application at the beam time experiment 69
5.1 Mechanical reliability of the portable setup 69
5.2 Shadowing, noise and the visibility 73
5.3 Backlighter measurements 78

6 Conclusion 80

Acknowledgements 82

A Appendix 83

Bibliography 90

1 Scientific case

High power lasers are often used in the field of material processing. These lasers can cut steel with a thickness of 25 mm [WGLC]. The beam intensity reaches up to $10^9\,\mathrm{W/cm^2}$ [HG09]. The Petawatt High-Energy Laser for Heavy Ion EXperiments (PHELIX) at the GSI Helmholtzzentrum in Darmstadt is also classed as a high power laser. The maximal intensity of this laser reaches even $10^{21}\,\mathrm{W/cm^2}$ [Gö20]. But with the repetition rate of approximately 1.5 h and a pulse duration of 0.5 to 20 ps, the laser is not even capable of cutting a 1 mm thick aluminum sheet. However, if the laser pulse hits a micrometer-thick wire, it literally explodes. During this, an x-ray flash with a duration of below 1 ns is emitted [BAB+10]. This x-ray flash can be used in science. Rapid processes, for example, can be imaged sharply. This basic principle of x-ray imaging is used in the research field of high-energy-density (HED) physics (see e.g. [MMD+09, THH+11]). But there is a difficulty with these measurements. Usually, the examined object is of low absorption. Therefore, absorption-based x-ray imaging can have a lack of contrast.

When x-rays pass matter they are not only absorbed but also gain a phase shift. This phase shift can be measured using grating-based x-ray phase-contrast imaging (GBPCI). Measuring the phase shift implies a higher sensitivity to density variations in the target [SLA+19]. The output is directly proportional to the electron number density ρ_e [Sei20]. This value is of interest in the field of HED science [FRS04]. The capability of GBPCI for imaging plasma density distributions in shocked matter at such facilities was tested. For that purpose, a grating interferometer was specifically designed for the experimental conditions present at the PHELIX facility. A particular key feature is the portability of the interferometer and the mechanical rigidity it requires.

This thesis covers the whole conceptualization and characterization process of the interferometer. With data acquired during the experiment at the PHELIX facility, it is evaluated whether the assumptions made for conceptualizing the interferometer were correct. Furthermore, the mechanical design of the device is evaluated.

2 Fundamentals and methods

Radio waves, visible light and x-rays are types of electromagnetic radiation. They differ in their associated wave length ranges. Visible light ranges in between 400 nm and 700 nm, x-ray radiation between 0.01 nm and 10 nm [Dem18]. The energy of electromagnetic radiation can be calculated by $E = {}^{h \cdot c}/_{\lambda}$, with the Planck constant h, the light velocity in vacuum c and the wavelength λ of the radiation [Mes15]. Therefore x-rays range from 10^2 eV to 10^5 eV, visible light is in the range of a few eV. This has an effect on the interaction of the radiation with matter [Pag06]. X-rays can propagate through matter which is opaque for visible light.
This chapter discusses the theoretical fundamentals and methods used in this thesis. At first the interaction of x-ray radiation with matter is explained. Section 2.2 addresses x-ray sources and the detection of x-rays. In section 2.3 Talbot-Interferometry is introduced, starting with the Talbot effect, followed by the moiré effect and the image retrieval.

2.1 Interaction of x-ray radiation with matter

The following sections deals with the interaction of x-ray radiation with matter is discussed. The main focus is the description of phase shifts and attenuation due to matter. If not marked otherwise, the equations, values and explanations are adapted from [Pag06].
Two wave equations can be derived from Maxwell's equation. One for the electric field strength $\vec{E}(\vec{r}, t)$ and one for the magnetic flux density $\vec{B}(\vec{r}, t)$. These two fields form in conjunction the electromagnetic radiation. The radiation can be described by one scalar field $\psi(\vec{r}, t)$, which depends on the position $\vec{r}$ and time t by the wave equation:

$$\left(\frac{n^2}{c^2} \cdot \frac{\partial^2}{\partial t^2} - \nabla^2 \right) \psi(\vec{r}, t) = 0, \tag{2.1}$$

with the speed of light in vacuum c and the refractive index n. The refractive index n depends on the material and the wavelength of the radiation. For vacuum $n = 1$ applies, and in presence of matter the refractive index can be written as

$$n = 1 - \delta - i\beta, \tag{2.2}$$

with δ being the refractive index decrement and β the extinction coefficient. In the x-ray regime the values, δ and β, are $\ll 1$. Values can be found in online databases, for example in [HGD93]. There, δ and β are tabulated for elements and compounds in an energy range of 50 eV to 30 keV.

If the wave equation is solved, as stated in Equation 2.1, for an arbitrarily shaped medium with a refractive index $n(\vec{r})$, usually the projection approximation is used. It is assumed, that the ray path is negligible perturbed during passing the medium. So, the phase and amplitude shifts can be calculated using the trajectory along the initial propagation direction. With this approximation, the wave equation can be solved with a plane wave ansatz

$$\psi(\vec{r}, t) = \psi_0 \cdot e^{-i(n\vec{k}\vec{r}-\omega t)}, \tag{2.3}$$

with the amplitude ψ_0 and the angular frequency ω. The wave vector $\vec{k}$ points into the propagation direction of the wave. The absolute value of the wave vector, the wave number, connects the angular frequency ω and the velocity of light c, $|\vec{k}| = \omega/c$. For the sake of clarity it is assumed that the plane wave propagates along the z-axis, which means $\vec{k} = (k_x = k_y = 0, k_z = k)$. Equation 2.3 becomes

$$\psi(z, t) = \psi_0 \cdot e^{-i(nkz-\omega t)}. \tag{2.4}$$

If the wave enters a medium at $z = 0$, the refractive index n changes from 1 to $(1 - \delta) - i\beta$. Inserting this into the plane wave ansatz, the equation becomes

$$\psi(z, t) = \psi_0 \cdot e^{-i[((1-\delta)-i\beta)kz-i\omega t]} \tag{2.5}$$

$$= \underbrace{\psi_0 \cdot e^{-i(kz-\omega t)}}_{\text{vaccum propagation}} \cdot \underbrace{e^{-\beta kz}}_{\text{damping-term}} \cdot \underbrace{e^{i\delta kz}}_{\text{phase-term}} . \tag{2.6}$$

The propagation of a plane wave in a medium can be described via three terms. The first term is the same as the propagation in vacuum. The second term describes an exponential decay of the amplitude ψ_0, which depends on the propagation length in matter. The last term is a phase term. It describes the additional phase, which an electromagnetic wave acquires due to the propagation in a medium. In the following the damping and phase term is discussed in detail.

Damping-term

In experiments only the intensity I of the electromagnetic wave can be measured. The intensity of a wave is the second power of the scalar field $\psi(z, t)$

$$I(z) = |\psi|^2 = \psi_0^2 \cdot e^{-2\beta kz}. \tag{2.7}$$

By using the relation $2\beta k = \mu$ the Lambert-Beer law can be retrieved:

$$I(z) = \psi_0^2 \cdot e^{-\mu z}, \tag{2.8}$$

with the attenuation coefficient μ. The intensity of the wave is decreasing exponentially with the thickness of the penetrated material. In case of an inhomogeneous attenuation coefficient along the propagation direction, Equation 2.8 becomes

$$I(z) = \psi_0^2 \cdot e^{-\int_0^z \mu(\tilde{z})\,\mathrm{d}\tilde{z}} \tag{2.9}$$

In online databases, like [Cha00], the mass attenuation coefficient is tabulated for elements and compounds on a broad energy spectrum. The mass attenuation coefficient is given by μ/ρ, with ρ the density of the material. In Figure 2.1 the mass attenuation coefficient is plotted for carbon over the x-ray energy spectrum. Three effects contribute additively to the attenuation coefficient in this energy regime:

$$\mu(E) = \mu_{\text{coh.}} + \mu_{\text{ph.}} + \mu_{\text{comp.}}, \tag{2.10}$$

with coherent scattering $\mu_{\text{coh.}}$, photoelectric absorption $\mu_{\text{ph.}}$ and the Compton effect $\mu_{\text{comp.}}$. A description of these effects can be found e.g. in [Pag06, DM11].

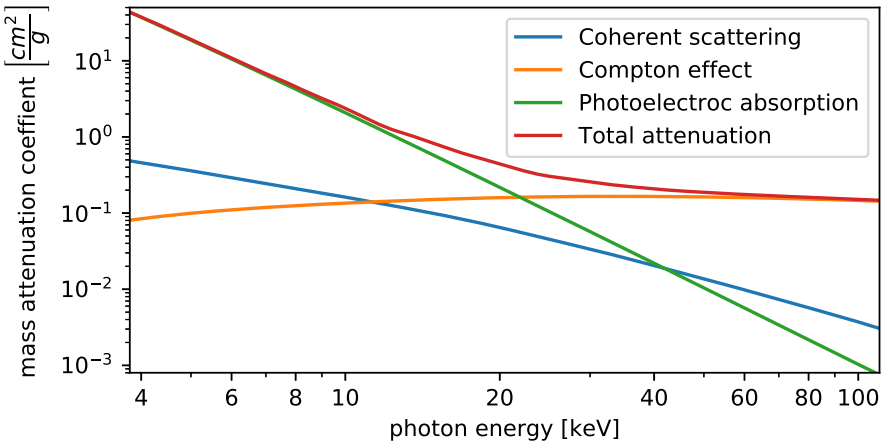

Fig. 2.1: Mass attenuation coefficient of carbon versus photon energy. In the plotted energy range the photoelectric absorption (green), the Compton effect (orange) and the coherent scattering (blue) add up to the total attenuation (red). Values are taken from [Cha00].

Phase-term

When an electromagnetic wave propagates through a medium, an additional phase is acquired. Assume a material without damping and a thickness d. That way, the wave which propagates through this medium can be written as

$$\psi(z,t) = \psi_0 \cdot e^{-i(kz+\Delta\varphi)} \cdot e^{i\omega t} \qquad \text{for } z > d,$$

with the constant phase term $\Delta\varphi$. The phase term is given by

$$\Delta\varphi = -k\delta \cdot d. \tag{2.11}$$

This phase shift $\Delta\varphi$ is a measure of the shift relative to a wave, which would propagate the same distance in vacuum. For an inhomogeneous medium the phase shift can be calculated by

$$\Delta\varphi = -k \int_0^d \delta(z)\,\mathrm{d}z. \tag{2.12}$$

Under consideration of Figure 2.2 a plane wave hits an object with a thickness profile $d_{\mathrm{obj}}(x)$. Due to the change of the refractive index, the wavelength changes, $\lambda_{\mathrm{med}} = \frac{\lambda_{\mathrm{vac}}}{n}$. As n is smaller than one for x-rays, the wavelength gets enlarged. Hence, the phase front is shifted ahead. This leads to an x dependent disturbance of the phase front $\varphi(x)$, which can be calculated by

$$\Delta\varphi(x) = k \cdot \int_0^{d_{\mathrm{obj}}(x)} \delta(x,z)\,\mathrm{d}z. \tag{2.13}$$

Note that Equation 2.12 holds true for a phase shift along a certain path, whereas a phase front is calculated in Equation 2.13. In Figure 2.2 the wedge-shaped object imprints a comparable shape onto the phase front. The tilting of the phase front, relative to the former plane wave, can be quantified with an angle $\alpha(x)$. This angle is identical with the angle that describes the deviation between the current direction of propagation and the original one.

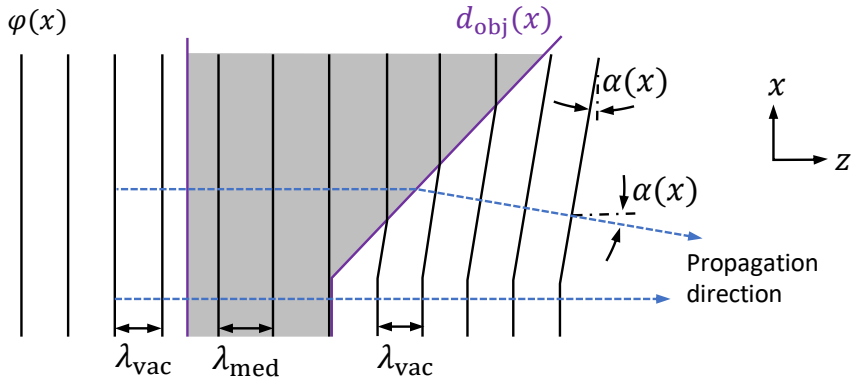

Fig. 2.2: Modification of a plane phase front $\varphi(x)$ due to an object with a thickness-profile $d_{\mathrm{obj}}(x)$. The tilting of the phase front and therefore the change of the propagation direction is quantified with the angle $\alpha(x)$.

After [Hof18] this angle $\alpha(x)$ can be calculated as follows. As mentioned, the $\vec{k}$-vector indicates the propagation direction of the wave. So, the angle $\alpha(x)$ is given by

$$\tan\left(\alpha(x)\right) = \frac{k_x}{k_z} \tag{2.14}$$

With k_z and k_x as the z and x-component of the $\vec{k}$-vector, respectively. The deviations of the propagation direction, caused by an object, are in the mrad range, see [Pag06]. So k_z can be approximated by $k_z \approx |k| = {}^{2\pi}/_{\lambda}$. The propagation direction of the wave is perpendicular to the phase front. Hence, the $\vec{k}$-vector is given by

$$\vec{k}(x) = \nabla\varphi(x). \tag{2.15}$$

For the k_x component follows

$$k_x = \frac{\partial\,\varphi(x)}{\partial x} \tag{2.16}$$

By inserting Equation 2.16 and the approximation for k_z into Equation 2.14, $\alpha(x)$ is given by

$$\tan\left(\alpha(x)\right) = \frac{\lambda}{2\pi} \cdot \frac{\partial\,\varphi(x)}{\partial x} \tag{2.17}$$

$$= \frac{\partial \int_0^{d_{obj}(x)} \delta(x,z)\,\mathrm{d}z}{\partial x}. \tag{2.18}$$

In Equation 2.18 the phase front $\varphi(x)$ was replaced with Equation 2.13.

2.2 X-ray sources and detection

2.2.1 X- ray tubes and backlighters

X-ray tubes consist mainly of three parts. A filament and a metal anode placed in an evacuated tube. Between the filament and the anode a high acceleration voltage U_A is applied. The filament is heated and causes electrons to escape. Due to the applied voltage, the electrons get accelerated towards the anode. In the metal anode the electrons get decelerated and emit x-ray radiation.[Dem18] The emitted x-ray spectrum depends on the anode material and the acceleration voltage. The spectra can be divided into an part caused by bremsstrahlung and by a characteristic line emission [DM11]. The bremsstrahlung forms a continuous spectrum with a maximal x-ray energy of $E_\gamma = eU_\mathrm{A}$, with e being the elementary charge[Dem18]. The characteristic line emission is caused by fluorescent radiation of the metal [DM11].
The x-ray tube used during the experiments is a microfocus x-ray tube from the company Yxlon with the designation Fxe-160.51 . The data sheet can be found in [YXL] and a detailed characterization of this tube in [Sch16]. Within this thesis an acceleration voltage of 45 keV was not exceeded. This is according to [TV09] below the characteristic line energies of the tungsten anode. Hence, no characteristic line emission appears in the spectra.

X-ray backlighter sources consist of a high power laser and a target on which the laser is focused. This target consists, for example, of a wire with a diameter of a few micrometers. When the laser, focused onto the target, reaches sufficient high intensities, electrons inside the material get accelerated up to MeV energies [MPR$^+$11]. These electrons propagate through the target material and emit bremsstrahlung and a material depended line emission.[NRE$^+$09] The duration of the x-ray flash can be as short as a few picoseconds. The focal spot size is limited to the solid density part of the target.[BAB$^+$10]

2.2.2 Detection of x-rays with scintillation detectors and imaging plates

In this thesis two different methods of x-ray detection are used. In the x-ray laboratories at the Ecap facility a digital Cmos detector is used and during the beam time experiment at the Phelix facility analog Imaging plates (Ips). The underlying principle and key data of the used x-ray detectors are outlaid in this section.
Digital Cmos detectors consists of a scintillator screen and a photodiode array. The x-rays which enter the detector are converted to visible light in the scintillator screen. For x-ray energies below 100 keV the scintillator material absorbs the photons via the photoelectric effect [Buz11]. The ionized scintillator material emits visible light via fluorescence [Imaa]. The light is subsequently detected and digitalized with the photodiode array [Imaa].

The detector used at the ECAP facility is a Teledyne Dalsa Shad-o-Box 6k-HS with a pixel sized of 49.5 μm and an active area of 114×146 mm. The detector can detect in an energy range of 10-225 kV. [Imab]

IPS consist of three layers. A carrier foil on which a layer of x-ray detecting photostimulable phosphorus crystals is applied, covered with a thin protective layer. When the IP is exposed to x-ray radiation, some of the electrons in the crystals are liberated and get trapped in metastable lattice defects. For the read out process, the IPS have to be brought to a special scanner. This scanner stimulates the emission of trapped electrons. During the recombination process of the electrons with the crystal, visible light is emitted. The emitted light is proportional to the incident radiation light and is detected in the scanner. [FMMS12]
During the PHELIX experiment Fuji BAS type SR Imaging plates are used. The images are scanned with a pixel size of 50 µm. The resolution of the IPS was in [FMMS12] determined to 109 µm.

2.3 Grating based interferometry

Measuring the attenuation of x-ray radiation in matter is done since 1896, the year of it's discovery [Rön96]. Medical applications of x-rays started already one year after [Kev97]. The phase shift induced by matter was first measured in 1965 by Bonse and Hart [BH65]. Since then day numerous techniques had been invented to measure the phase shift [DBC12]. In the experiment at the PHELIX facility GBPCI is used to measure the phase shift. The basis of this method is the Talbot effect, which is described in subsection 2.3.1. In the following subsections the moiré effect is introduced, a method of retrieving sub pixel scale fringes. In subsection 2.3.3 the image retrieval process is described. Three image modalities are presented and their physical meaning explained.

2.3.1 The Talbot effect and interferometry

The Talbot effect is a near-field effect that can be observed when an electromagnetic wave hits a periodic structure, e.g. a grating, see [Pag06]. This is visualized for an absorption grating in Figure 2.3 a). There, the grating was cut perpendicular to the grating bars. A plane-, monochromatic wave propagates undistorted along the z-axis and hits the absorption grating G_1. The intensity pattern of the grating is repeated after a certain distance d_T behind the grating. An absorption grating absorbs all intensity where the grating bars are. Thus, the intensity pattern is maximal in between the grating bars and zero behind them. The intensity pattern at the so called Talbot distance d_T is named Talbot pattern.
In a second scenario, an object, for example a wedge, is positioned in front of the grating G_1. See Figure 2.3 b). This wedge has got a refractive index which is different from the surrounding medium. A phase shift is accumulated by passing the wedge. Parts of the plane wave are not perfectly parallel to the grating anymore. Hence the wave does not hit the grating parallel. In this case the intensity pattern of the grating is not repeated perfectly as on contrast to the previous case. Therefore, the area under consideration must be divided into parts which are parallel to the grating, and the ones which are not. The parallel parts form the same intensity pattern as in the previous case. The grating bars which are obliquely irradiated also form a Talbot pattern. But the pattern is shifted along the x-axis compared to the previous case. So, the Talbot pattern depends on the shape of the phase front of the incident wave.
In grating based interferometry, the Talbot effect is the basis to measure the phase-shift caused by an object. This requires two measurements. The first measurement needs to be without any distortions stemming from the object, as described in the first case. This measurement is called the reference. The second measurement is done with an object in the beam path, referred to as the object measurement. By comparing these two measurements the part of the distortion of the pattern that is caused by the object can be identified. This distortion is proportional to the phase-shift caused by the object. But the Talbot

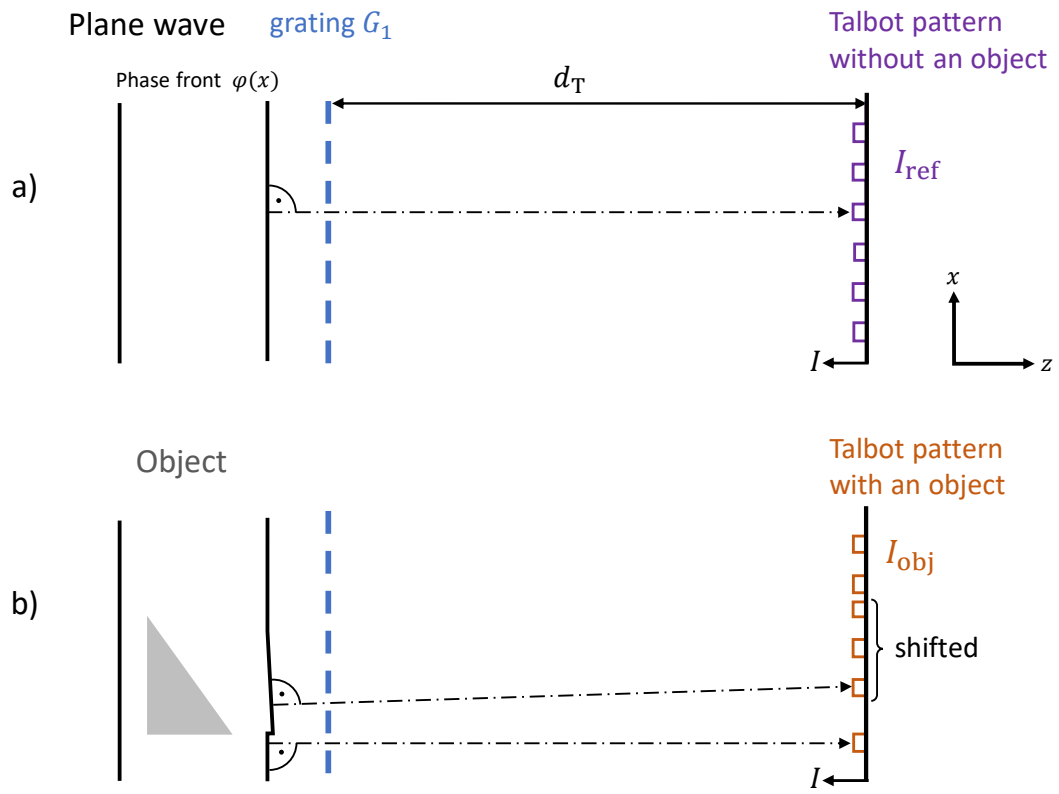

Fig. 2.3: Visualization of the effect of an object to the Talbot pattern. The Talbot pattern is visualized as an intensity plot along the x-axis. A plane wave with phase fronts $\varphi(x)$ propagates along the z-axis. In a) the plane wave hits the periodic structure and gets repeated downstream at the Talbot distance. In b) the plane wave gets distorted by a wedge. As a result a part of the periodic structure gets shifted along the x-axis. Own figure, adapted from [Gal17].

effect on its own is not sufficient to make the phase-shift visible. Two further steps are necessary. In the x-ray regime one detector pixel is typically much larger than the period of the Talbot pattern. Hence the pattern can not be resolved. Therefore the Talbot pattern must be made visible in a additional prior step. The moiré effect provides one possible way to overcome the limitation of the detector resolution. This effect is examined in subsection 2.3.2. But the phase-shift information is still divided into object and reference measurements. In a second step a computer program can be used to obtain an image that can be interpreted by the human eye. This program is based on Fourier imaging and will be described in subsection 2.3.3.

As a next step, the Talbot effect is examined more closely and described mathematically.

Mathematical description of the Talbot effect

The mathematical description of the Talbot distance d_T, by Lord Rayleigh [Ray81], goes as far back as 1881:

$$d_\mathrm{T} = \frac{2m \cdot p^2}{\lambda} \qquad m \in \mathbb{N}, \tag{2.19}$$

with the grating period p, the wavelength λ of the incoming wave and m, an integer that numbers the order of the Talbot distances. The whole diffraction pattern behind the grating can be calculated by using the Fresnel diffraction theory, see [Pag06]. This pattern is called Talbot carpet.

In Figure 2.4 three different Talbot carpets are mapped. They are induced by a plane, monochromatic wave with an intensity I_0 which propagates from left to right. This wave hits gratings which differ in their characteristics. The carpet in a) is induced by an absorption grating. Carpet b) and c) by phase gratings.

The bars of absorption gratings are highly absorptive. Therefore, ideally, all electromagnetic radiation is blocked at the bars locations. In contrast to this, an ideal phase-grating does not block any radiation. Such a phase grating only modifies the phase front. The plane wave accumulates a phase shift where the grating bars are located. The amplitude of the phase shift is determined by the height of the grating bars and the wavelength of the electromagnetic radiation. Hence the phase shift is only valid for one single wavelength. Usually the wavelength is described by the corresponding energy $E = {}^{h \cdot c}/_{\lambda}$, named design energy. The phase shift of a phase grating is given in multiples of π. This means, a π-shifting grating imprints a phase shift of half the wavelength onto the phase front.

The Talbot carpet is, besides the type of used grating, also dependent on the ratio of the gap width w between the grating bars as compared to the period p of the lattice. The period p of a lattice is the length of the repeated structure, the sum of the gap width and the grating bar width. This ratio is defined as the duty cycle $Dc = {}^{w}/_{p}$. Only gratings with a Dc of 0.5 are considered here, because only such gratings are used in this thesis.

The Talbot carpet in Figure 2.4 a) is induced by an absorption grating. The carpet shows two repeated intensity patterns. One at the Talbot distance d_T and one at half the Talbot distance $\frac{d_\mathrm{T}}{2}$. The pattern at half the Talbot length is shifted lateral by half a grating period. This was first examined by [BK96, CGM+97].

Talbot carpets, induced by phase gratings, displayed in b) and c), have an uniformly distributed intensity at multiples of the Talbot distances d_T. This is in agreement with the Talbot formula, as the intensity directly behind the gating is also uniformly distributed. The intensity pattern, which can be used for phase-contrast imaging, only occurs at fractions of the Talbot distance, see [Sul97]. These distances are called fractional Talbot distances $d_{\mathrm{f}\Gamma}$.

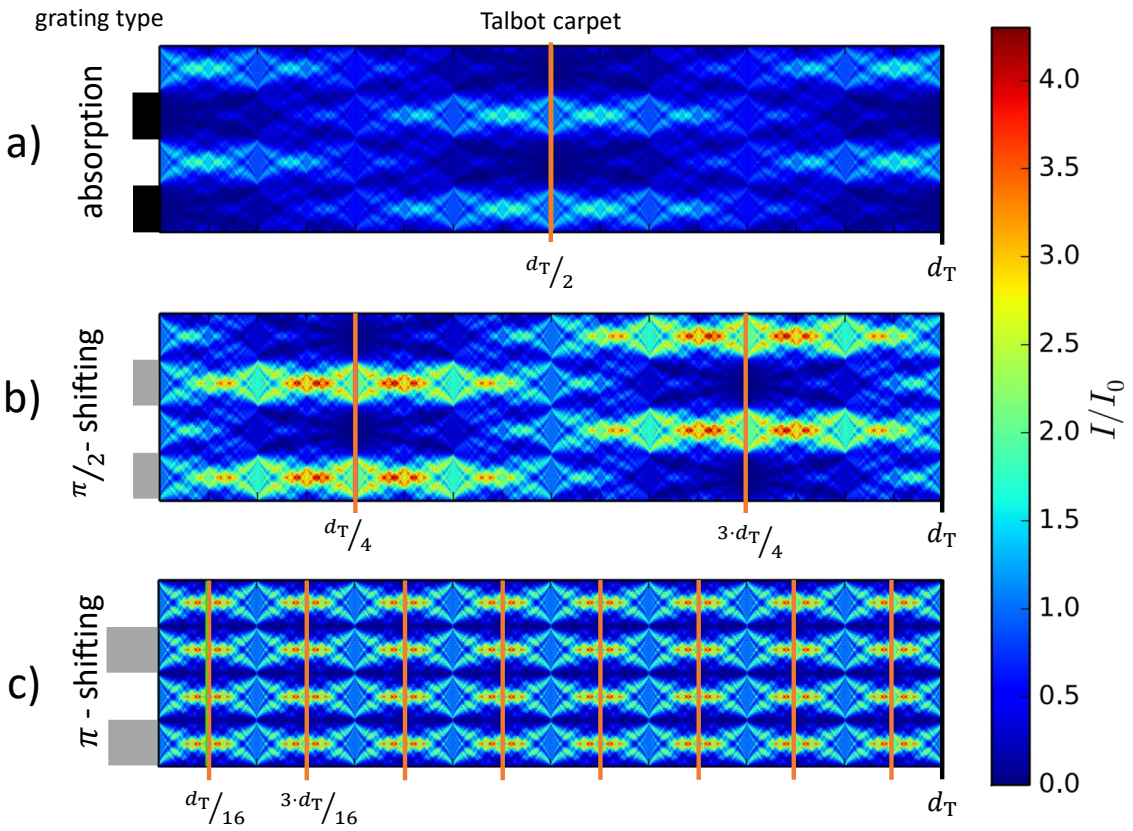

Fig. 2.4: Simulation of Talbot carpets for different types of gratings and a monochromatic plane wave. The colorbar represents the normalized intensity. In a) the grating is an absorption grating, in b) a $\pi/2$-shifting grating and in c) a π-shifting phase grating. The Talbot carpet is plotted vertically for two periods of the grating. The black boxes on the left side indicate the grating bars. The horizontal dimension is normalized to one full Talbot distance d_T. The orange lines indicate the fractional Talbot distances d_{fT}. Image was taken from [Wol16] and modified.

These distances can be calculated after [YL15] to:

$$d_{fT} = \frac{(2m-1)p^2}{2\eta^2\lambda} \qquad m \in \mathbb{N}, \tag{2.20}$$

with the intrinsic grating parameter η given by:

$$\eta = 1 \qquad \text{for } Dc = 0.5 \text{ and } \frac{\pi}{2}\text{-shifting grating}$$
$$\eta = 2 \qquad \text{for } Dc = 0.5 \text{ and } \pi\text{-shifting grating}$$

In Figure 2.4 b), for a $\pi/2$-shifting grating, the repeated intensity pattern occurs the first time at $d_T/4$ and repeats in multiples of $d_T/2$. The Talbot carpet of the π-shifting grating in c) looks different, compared to a) and b). The repeated intensity pattern has got half the period of the grating. This phenomenon is called frequency doubling. The pattern occurs

the first time at $^{d_T}/_{16}$ and is repeated every eighth of a Talbot distance without changing the vertical position of the maximal intensity. It is worth mentioning that the maximal relative intensity of the phase gratings b) and c) are significantly higher than the one of the absorption grating a). This is based on the fact that an absorption grating blocks part of the radiation and a phase grating is only modulating the phase front.

Common x-ray sources, like x-ray tubes, emit a broad frequency spectrum. The Talbot and the fractional Talbot distances are after Equation 2.19 and Equation 2.20 wavelength dependent. Hence, the Talbot carpet of a polychromatic source is a superposition of many single Talbot carpets. This results in a blurred carpet with reduced contrast, see [Lud20]. X-ray tubes and backlighters have a diverging beam. A plane wave, which hits the grating, as assumed for Figure 2.4, is not anylonger a realistic assumption for these x-ray sources. A cone beam is more appropriate. As a consequence the Talbot carpet is stretched in length and width, see [EBS+07]. This means the Talbot pattern as well as the (fractional) Talbot distances get magnified with a factor M

$$d_{\mathrm{fT,cone}} = M \cdot d_{\mathrm{fT}}. \tag{2.21}$$

2.3.2 Image retrieval, the moiré effect

For the aforementioned grating based interferometer, the period of a Talbot pattern is smaller than one detector pixel. Hence the Talbot pattern can not be resolved directly. With the help of a second grating G_2 the Talbot pattern can be analyzed. This grating is placed where the Talbot pattern is visible, e.g. the Talbot distance d_T, see Figure 2.5 a). There are two methods to retrieve the Talbot pattern using the analyzer grating G_2: phase stepping (see [WDD+]) and moiré imaging (see [TIK82]). In this thesis only moiré imaging is relevant. As outlined in the introduction, the main goal of the experiment, at the PHELIX facility, will be imaging plasma density distributions in shocked matter. The phase stepping method requires at least three images per reference and object measurement, see [Sei20, Lud20]. It is not feasible to generate an identical plasma shock twice. Hence the aforementioned phase stepping is not an option. Moiré imaging requires only one image per reference and object measurement [SGL+18].
By overlaying two similar periodic structures a new pattern is generated, even though it is not present in the original structures [Ami09]. This is called the moiré effect, see Figure 2.5 b). The period of the new pattern depends on the angle between the two periodic structures and on their periods, see [Ami09]. Compared to the grating periods p_T and p_G of the two gratings, the period p_m of the moiré pattern is larger. This larger moiré pattern can be detected by x-ray detectors.
In the case of the Talbot interferometer one periodic structure is the Talbot pattern, the other one the analyzer grating G_2. If the Talbot pattern changes locally due to an object in front of G_1, see subsection 2.3.1, the moiré pattern will change locally too. The change

of the moiré pattern is then detected. With the, in subsection 2.3.3 introduced, Fourier image reconstruction method, the phase shift can be retrieved. Subsequently the moiré effect is described mathematically.

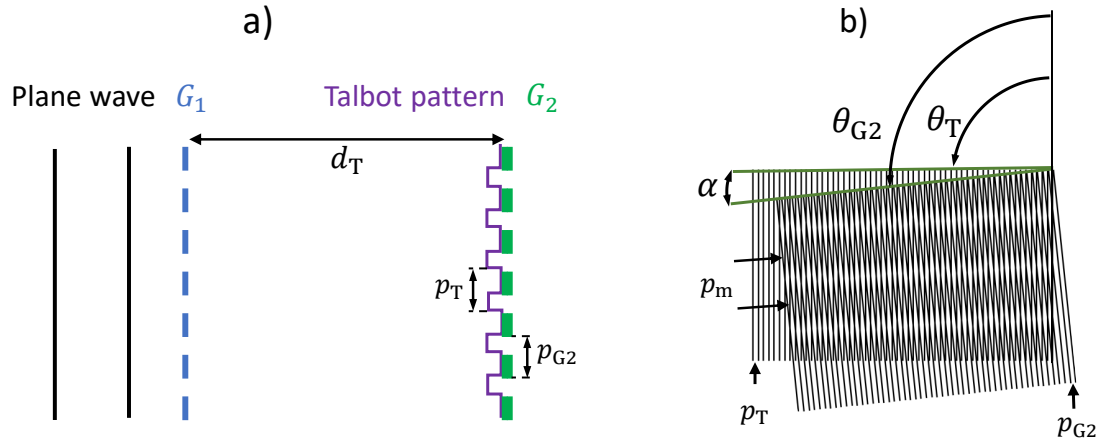

Fig. 2.5: a) Setup of a Talbot interferometer for the x-ray regime. The plane wave hits the grating G_1 which generates a Talbot pattern at the Talbot distance d_T. There, an analyzing grating G_2 is placed to retrieve the Talbot pattern.
b) Visualization of the moiré effect. Two binary gratings with periods p_{T} and p_{G2} are superposed under an angle α. The resulting moiré period p_{m} is larger than both periods of the initial gratings. The idea of moiré imaging can be visualized by increasing the distance between the reader and this image. At a distance of $1-4$ m, the grating pattern p_{T} and p_{G2} disappears, whereas the moiré pattern is still visible. Image b) was taken from [Ami09] and modified.

Mathematical description of the moiré pattern

The moiré pattern depends on the angle α of the two gratings and on the periods of the overlaid structures. If the periods of the gratings are approximately the same, the moiré period p_m can be calculated, according to [Ami09], to

$$p_{\mathrm{m}} = \frac{p_{\mathrm{T}} p_{\mathrm{G2}}}{\sqrt{p_{\mathrm{T}}^2 + p_{\mathrm{G2}}^2 - 2 p_{\mathrm{T}} p_{\mathrm{G2}} \cos(\alpha)}}, \tag{2.22}$$

with p_{T} and p_{G2} being the period of the Talbot pattern and the period of the Grating G_2, respectively. α is the relative tilting angle between the gratings. All variables are additionally visualized in Figure 2.5. The angle of the moiré pattern α_m is given, according to [Ami09], by

$$\alpha_{\mathrm{m}} = \arctan\left(\frac{p_{\mathrm{G2}} \sin\theta_{\mathrm{T}} - p_{\mathrm{T}} \sin\theta_{\mathrm{G2}}}{p_{\mathrm{G2}} \cos\theta_{\mathrm{T}} - p_{\mathrm{T}} \cos\theta_{\mathrm{G2}}}\right), \tag{2.23}$$

with θ_T and θ_{G2} being the angle of the associated gratings to an arbitrary axis. $|\theta_T - \theta_{G2}|$ is then equal to the relative tilting angle α. Without loss of generality θ_{G2} can be chosen

to be 0. This means that θ_T is equal to α and thus α_m represents the angle between the moiré pattern and the grating bars of G_2.
In Figure 2.6 a color coded visualization of the theoretical moiré period p_m and the moiré angle α_m can be seen. The influence of the deviation of p_T and p_G2 on the grating is printed on the horizontal axis. Therefore, the period p_T is varied relative to p_G2. The dependence of the angle between the gratings α is printed on the vertical axis. The moiré period p_m (Equation 2.22), was normalized with the grating period p_G2. The plot in Figure 2.6 a) shows the period of the moiré pattern in multiples of the initial grating period. The better the gratings match in their periodicity and the overlay angle, the larger the moiré period. For a slight misalignement the magnification is in the hundreds. This is sufficient to resolve the Talbot pattern with a periodicity in the 10 µm range with detector pixels in the 100 µm range. The possible angular orientation of the moiré pattern α_m ranges from $-90°$ to $90°$, see Figure 2.6 b). This is because gratings are symmetric by 180°. Hence, the angular orientation can be in any direction. This means that the orientation of the two overlaid gratings can not be retrieved by only observing one single moiré pattern.

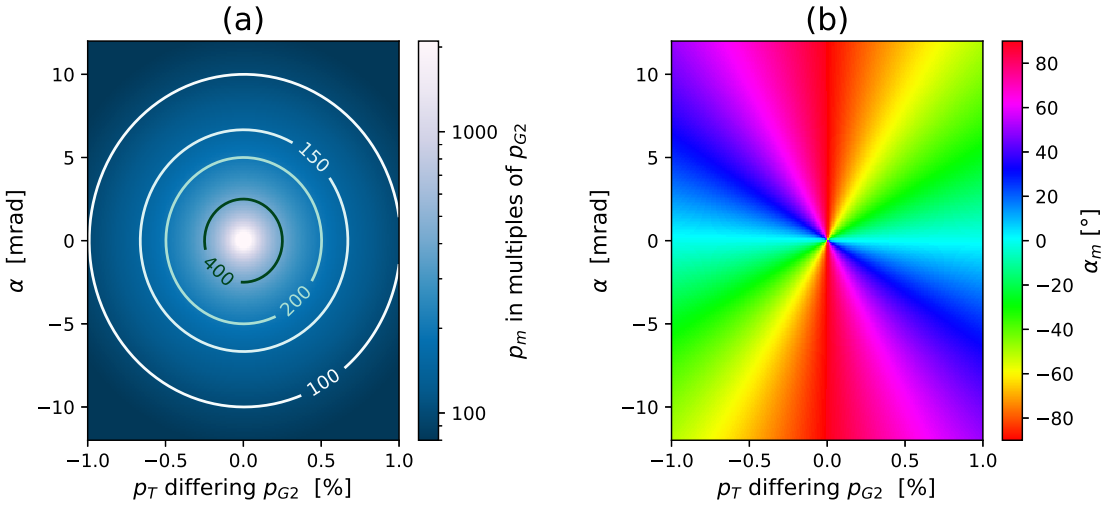

Fig. 2.6: Plot of the moiré period p_m relative to the G_2 period (a) and plot of the moiré angle α_m (b). The values resulting from Equation 2.22 and Equation 2.23 are plotted against the relative tilting angle α and the deviation of p_T to p_G2.

By placing an x-ray detector behind the grating G_2, the moiré pattern can be detected. Besides the moiré pattern a constant offset will be measured, see [Ami09]. To quantify how visible the moiré fringes are, relative to the constant offset, the visibility can be used. The visibility V is defined after [Pag06]:

$$V = \frac{I_\mathrm{max} - I_\mathrm{min}}{I_\mathrm{max} + I_\mathrm{min}}, \tag{2.24}$$

with the maximal and minimal intensity I_{max} and I_{min}, respectively, see Figure 2.7. For a sinusoidal intensity pattern the visibility can be calculated with

$$V = \frac{\mathrm{A}}{I_{\mathrm{mean}}}, \tag{2.25}$$

with the amplitude of the fringe pattern A and the constant offset I_{mean}. The visibility is in the range between zero and one. The larger the DC offset, compared to the amplitude of the Talbot pattern, the lower the visibility and vice versa.

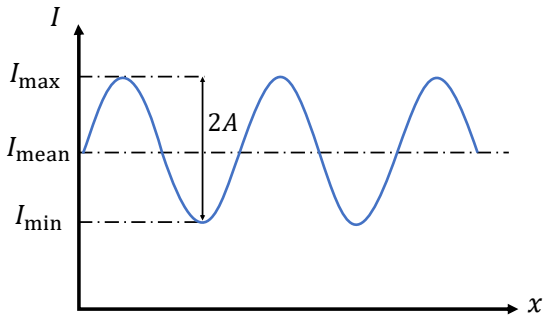

Fig. 2.7: Sinusoidal oscillation with a constant DC offset. The visibility V of the oscillation can be calculated using the amplitude A and I_{mean}, or I_{max} and I_{min}.

2.3.3 Image reconstruction

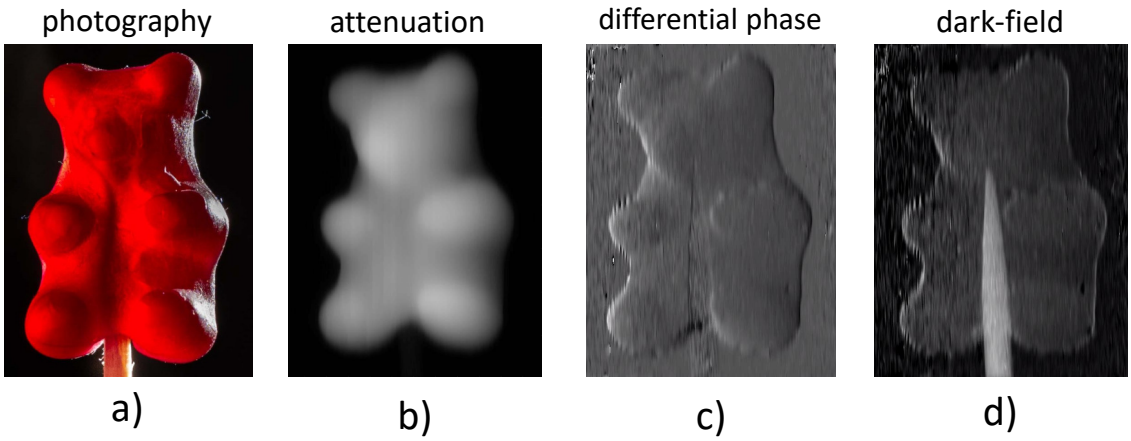

Fig. 2.8: Direct comparison of the three image modalities resulting from the grating based phase contrast measurements. A photography of the probed sample can be seen in a), the attenuation image in b), the DPC image in c), and the dark-field image d). Own measurements, idea adapted from [Zan13].

Grating based phase contrast imaging provides three image modalities: The attenuation image, the differential phase-contrast image (DPC image) and the darkfield image [Sei20]. In order to demonstrate the respective advantages of the image modalities, a gummy bear, penetrated by a wooden stick, is imaged. A photograph of the prepared gummy bear can be seen in Figure 2.8 a). An image modality, comparable to classical radiograph in medicine, can be seen in b). This is called the attenuation image. In this modality the wooden stick is almost not visible. In contrast to this, the wooden stick is clearly visible in c), the DPC image. Here the edges and the contours of the bear can also be seen well. The dark and bright areas, especially on the left and right side of the bear, give the image a three-dimensional appearance. In the dark-field image d), both the contour of the bear and the wooden stick can be seen.

A large part of the image reconstruction is done in the Fourier space. Therefore the Fourier representation of the object frame is discussed exemplarily. Figure 2.9 shows the object measurement first, its Fourier transform and two back transformations. The object measurement is a superposition of a gummy bear radiograph and the moiré pattern. By performing a Fourier transform, the object frame can be decomposed into its spectral components. The result of the transformation can be seen in the image $\mathcal{F}_{\text{obj}}$. The spectrum shows three peaks. One in the middle and two symmetrically orientated around the middle. The peak in the middle, called the zeroth peak $\mathcal{F}_0$ refers to low frequencies. The other peaks, called first order harmonic peaks $\mathcal{F}_1$ refers to higher frequencies. As the peaks are separated, an area around the peaks can be defined. These areas can be transformed back separately. A back transformation of these selected areas can be seen on the right side

of Figure 2.9. By performing a back transformation of the green framed areas (the high frequencies), the moiré pattern can be retrieved. The back transformation of the blue area (the low frequencies) results in the radiograph of the bear. This means the moiré fringes and the radiograph can be treated separately using the Fourier transform.

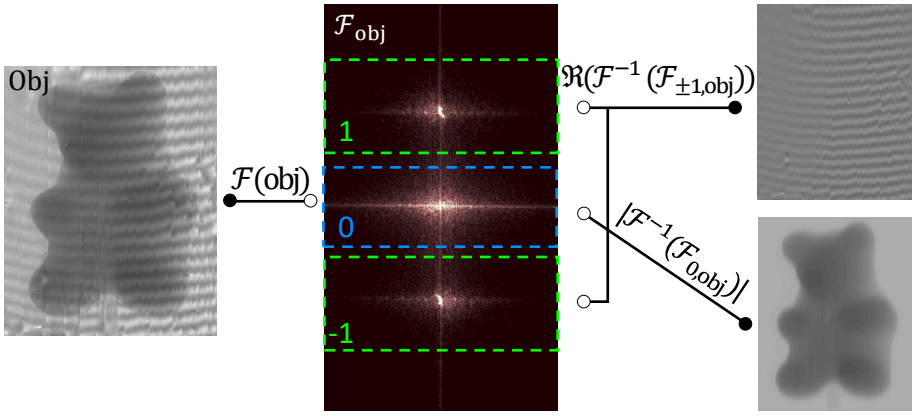

Fig. 2.9: Explanation of the Fourier transform of the object frame. The period of the moiré fringes of the object measurement are enlarged for a better understanding. The figure in the center shows the Fourier transform of the object measurement. The right figures is the back transformation of only the marked area in $\mathcal{F}_{obj}$. Adapted from [BKSW10].

The process of image reconstruction is visualized in Figure 2.10. This method was described for visible light by [TIK82]. For the x-ray regime [BZL+12, BKSW10] applied the method first.

This process can be divided into three stages. In the first stage the object and reference measurement are 2D-Fourier transformed. As can be seen in Figure 2.10, the Fourier transformation of the object and reference measurement leads to a similar frequency spectrum, $\mathcal{F}_{obj}$ and $\mathcal{F}_{ref}$. In a second stage two relevant areas are selected in the Fourier space. Due to the symmetrical properties of the Fourier transform, it is not relevant which first order peak $\mathcal{F}_1$ is selected. Then, in the third stage, the selected areas are back transformed and the three image modalities calculated. The last step of processing the selected area around the peaks is different for the thee image modalities and will be discussed separately.

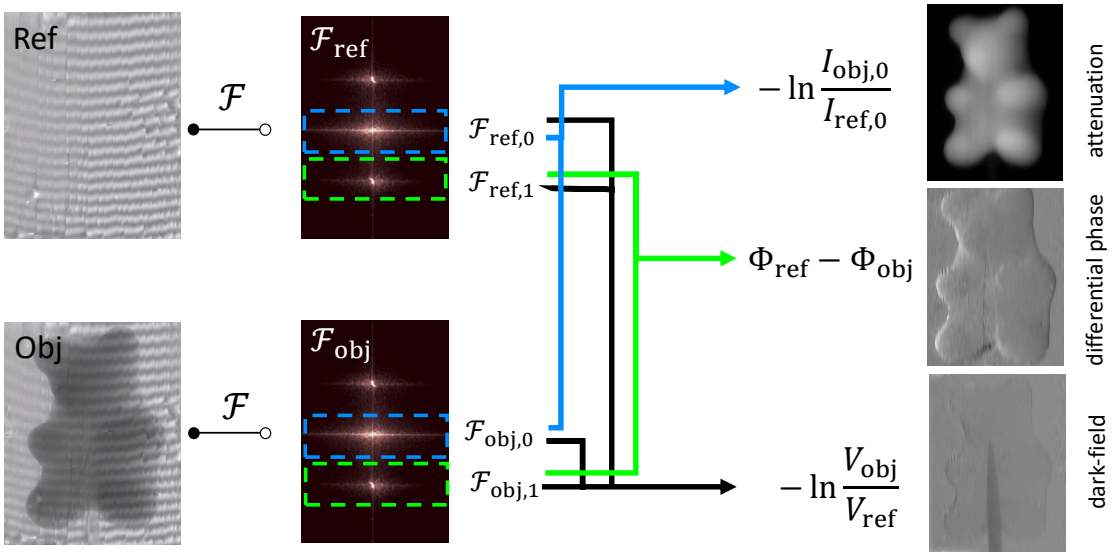

Fig. 2.10: Schematic of the Fourier reconstruction process. On the left side the object and reference measurements can be seen. The corresponding Fourier transformed images are on their right side. The colored frame indicates which areas are used for the generating the final images on the right side. The equations are presented in the corresponding image modality. Adapted from [Sei20].

Attenuation image

The attenuation image is given according to [BZL+12] by:

$$\Gamma = -\ln\left(\frac{\left|\mathcal{F}_{0,obj}^{-1}\right|}{\left|\mathcal{F}_{0,\text{ref}}^{-1}\right|}\right) = -\ln\left(\frac{I_{0,\text{obj}}}{I_{0,\text{ref}}}\right). \tag{2.26}$$

With $\left|\mathcal{F}_0^{-1}\right|$ as the absolute value of the inverse Fourier transform of the blue area around the zeroth order harmonic. $\left|\mathcal{F}_0^{-1}\right|$ is also denominated as the mean intensity I_0 of the measurement. To normalize the intensity over the whole image, the object measurement is divided by the reference. The negative logarithm is used to adapt the attenuation image to the well-known radiograph, used in medical imaging technology. Highly absorbing material appears bright, whereas low absorbing material appears dark.

The attenuation image describes the damping of the electromagnetic wave in the probed sample. The attenuation is correlated with the imaginary part β of the refractive index, see Equation 2.8. By again regarding the attenuation image of the gummy bear, Figure 2.8 b), it can be seen that thicker parts look slightly different. The wooden stick is hardly visible, because the absorption coefficient of the material does not differ enough from the surrounding jelly.

Differential phase contrast image

The DPC image is given according to [BZL+12] by:

$$\begin{aligned}\Delta\Phi &= \arg\left(\mathcal{F}^{-1}_{1,\mathrm{ref}}\right) - \arg\left(\mathcal{F}^{-1}_{1,\mathrm{obj}}\right) \\ &= \Phi_{1,\mathrm{ref}} - \Phi_{1,\mathrm{obj}},\end{aligned} \tag{2.27}$$

with

$$\arg\left(\mathcal{F}^{-1}_{1,ref}\right) = \arctan\left(\frac{\Im(\mathcal{F}^{-1}_{1,ref})}{\Re(\mathcal{F}^{-1}_{1,ref})}\right) \tag{2.28}$$

as the argument of the inverse Fourier transform of the green area around the first order harmonic in the reference frame or object respectively. This refers to the phase $\Phi_{1,\mathrm{ref}}$ of the moiré pattern of the reference or object respectively. By subtracting the phase of the reference from the object, the differential phase $\Delta\Phi$ can be calculated. Note that $\Delta\Phi$ is not the phase shift $\Delta\varphi$ of the object. Due to the periodical, sinusoidal character character of the moiré fringes, the differential phase $\Delta\Phi$ can only be determined modulo 2π. This means, if the differential phase exceeds 2π, the differential phase starts at 0 again. This phenomenon is called phase wrapping and can be corrected afterwards by software.

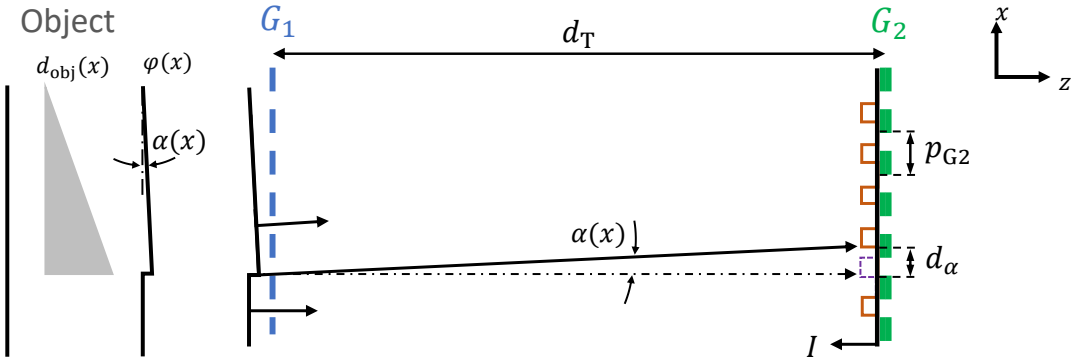

Fig. 2.11: Visualization of all relevant constants for the calculation of the differential phase $\Delta\Phi$. The angle α describes the tilting of the phase front $\varphi(x)$ and the associated deviation of the propagation direction. The brown pattern on the right side indicates the intensity pattern at the Talbot distance d_{T}. The purple dashed line indicates the position of an undistorted intensity pattern.

The DPC image $\Delta\Phi$ can be used to calculate the 2D projection along the sight line of the real part of the refractive index [BZL+12]. Therefore the change of the Talbot pattern has to be observed, when an object is placed into the incoming plane wave. This is visualized in Figure 2.11. The object with a thickness profile $d_{\mathrm{obj}}(x)$ distorts the phase front $\varphi(x)$. This distortion causes the tilting, quantified by the angle $\alpha(x)$. Due to this tilting angle $\alpha(x)$, the observed moiré pattern is shifted by d_α. This is visualized in Figure 2.11 with the help of the dashed purple intensity peak. This peak represents a part of the undistorted moiré

pattern. The shift d_α can be expressed as

$$d_\alpha = \tan(\alpha(x)) \cdot d_\mathrm{T}, \tag{2.29}$$

with the Talbot length d_T. According to Equation 2.18 and Equation 2.17 the tilting angle of the phase front $\alpha(x)$ is given by

$$\tan(\alpha(x)) = \frac{\lambda}{2\pi} \cdot \frac{\partial\, \varphi(x)}{\partial x} = \frac{\partial \int_0^{d_\mathrm{obj}(x)} \delta(z)\, dz}{\partial x}. \tag{2.30}$$

The differential phase $\Delta\Phi$ and the real part of the refractive index δ are connected via the relation

$$\frac{\Delta\Phi}{2\pi} = \frac{d_\alpha}{p_\mathrm{G2}}, \tag{2.31}$$

whereas δ is hidden in the relative shift of the Talbot pattern d_α. p_G2 denominates the grating period of the analyzer grating G_2. Combining this equation, with Equation 2.30 and Equation 2.29 leads to:

$$\Delta\Phi = \frac{d_\mathrm{T} \cdot \lambda}{p_{G2}} \cdot \frac{\partial\, \varphi(x)}{\partial x} \tag{2.32}$$

$$= \frac{d_\mathrm{T} \cdot 2\pi}{p_\mathrm{G2}} \cdot \frac{\partial \int_0^{d_\mathrm{obj}(x)} \delta(z)\, \mathrm{d}z}{\partial x}. \tag{2.33}$$

The derived equation can be used for an arbitrarily formed body. The DPC image is connected via an integral to $\delta(z)$, the real part of the refractive index. According to [Pag06] the real part of the complex refractive index depends on the electron density of the material

$$\delta(z) = \frac{r_e}{2\pi} \cdot \rho_e(z)\lambda^2, \tag{2.34}$$

with r_e being the classical electron radius, the electron number density ρ_e and the wavelength λ. Hence the DPC provides information about the projected electron density of an sample. Again referring back to the gummy bears in Figure 2.8. The DPC image of the bear c) seems to be illuminated from the left. This effect can be explained with Equation 2.33. According to this equation, the DPC image is proportional to the derivative of a thickness profile d_obj perpendicular to the grating bars. Hence, the dark and bright areas result from the positive and negative gradients of the thickness profile, respectively. Further Equation 2.33 implies that the DPC is only sensitive to deviations along the $x-$axis, perpendicular to the grating bars. The wooden stick is visible in the DPC image as noise. This is because the wooden stick has a fibrous structures and this disturbs the Talbot pattern. This leads to the noisy appearance. A way to quantify the disturbance of the Talbot pattern is the dark field image.

Darkfield image

The darkfield image is given according to [BZL+12] by:

$$\Sigma = -\ln\left(\frac{V_{\text{obj}}}{V_{\text{ref}}}\right), \tag{2.35}$$

with the visibilities V_{obj} and V_{ref} of the object and reference frame. The visibility can be calculated using

$$V = \frac{\left|\mathcal{F}_1^{-1}\right|}{\left|\mathcal{F}_0^{-1}\right|}, \tag{2.36}$$

with $\left|\mathcal{F}_1^{-1}\right|$ and $\left|\mathcal{F}_0^{-1}\right|$ as the absolute value of the inverse Fourier transformed green and blue area, respectively. This is definition equivalent to $V = {}^{A}/_{I_{\text{mean}}}$ (Equation 2.25), which can be used for the visibility of a sinusoidal signal.
The dark field is a measure of the decrease of the visibility. The decrease occurs mainly due to small angle scattering at edges and due to porous or fibrous structures of even sub pixel dimesions, see [LSH+19]. A more detailed investigation of the darkfield can be found in [Lud20].

3 Design of the interferometer

Two interferometers will be used during the beam time experiment. These interferometers only differ in the type of installed linear actors. The interferometer which images the shocked targets has linear stages, driven by stepper motors. For the other interferometer manually adjustable stages are used. As these interferometers only differ in this element, the whole design will be performed exemplarily for the setup, which images the shock.
As a first step, the basic concept of the experiment is explained. This includes an overview and a short explanation of the portable interferometer. The mechanical and theory based required specifications are outlaid in the subsequent sections. With this done, every component of the interferometer is discussed in detail. In the end of this chapter possible improvements are proposed, which could not be implemented within the framework of this work.

3.1 Classification and goal of the experimental setup

The Phelix laser at the Gsi Helmholtzzentrum (Darmstadt) is a laser with which backlighter experiments can be performed. Near the short laser pulse for the backlighter, a longer pulse is available too. This enables so called pump-probe experiments. Such an experiment was carried out at the Phelix facility between February 10 and February 28 in 2020. The main goal of this experiment was to test single shot GbPci concerning the imaging of Hed plasma density distributions in shocked matter. A schematic sketch of the experimental setup in the Phelix target chamber can be seen in Figure 3.1. The whole laser setup was installed and aligned by the GSI institute. The dark red laser beam has got a long pulse, which induces the plasma density distributions in the sample. The light red laser pulse has got a short duration and is used to generate the backlighter flash. The upper portable interferometer is used to to image the induced plasma density distribution. The second greyed-out interferometer does not see the induced plasma. It is instead used to gain data to get a deeper understanding of backlighter imaging.
The long pulse with a duration of $3 - 10\,\mathrm{ns}$ and an energy between $23 - 43\,\mathrm{J}$ is focused onto a sample (measured values during the beam time). This induces a plasma density shock in the material. The short pulse with a duration of 700 fs and energies between $20 - 35\,\mathrm{J}$ is focused onto the 5 µm tungsten backlighter wire (measured values during the beam time). The resulting x-ray flash propagates through the induced plasma density shock. By propagating through the shock, the phase front and the intensity changes, see section 2.1. As the delay time between the long and the short pulse can be adjusted between $1 - 7.7\,\mathrm{ns}$, different steps in the time evolution of the plasma can be observed.

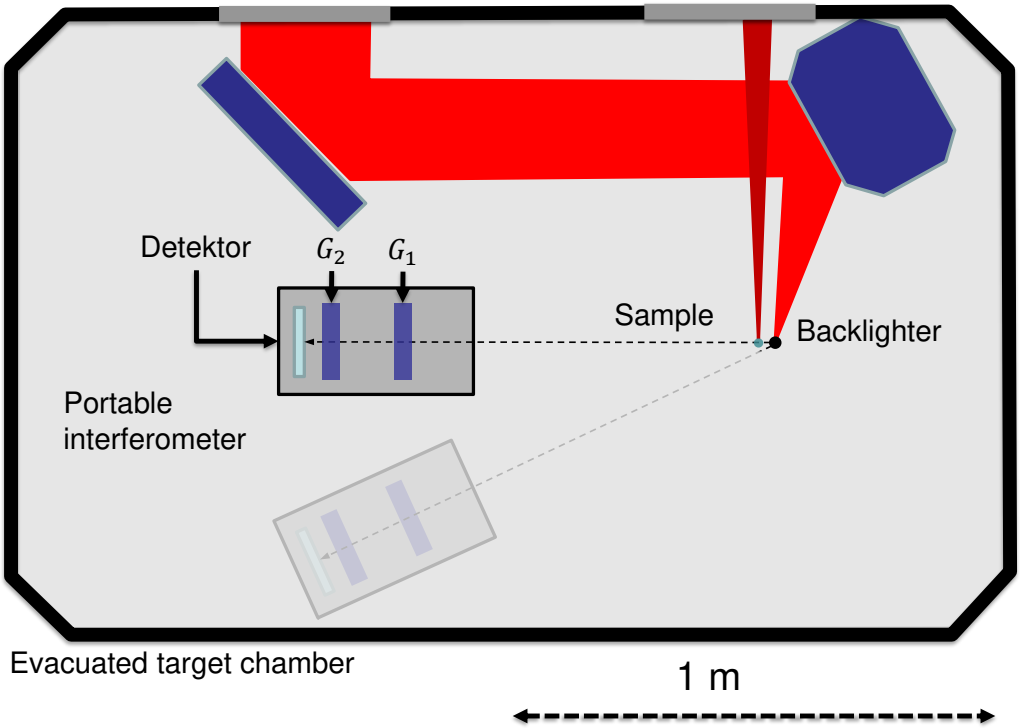

Fig. 3.1: Schematic sketch of the setup at the PHELIX facility. The light gray bars in the target chamber walls are the inlet flanges for the two laser beams. The dark red is the pumping beam. It gets already focused down outside of the target chamber. The light red the probing beam is guided via an flat mirror to the off-axis parabola which focuses the beam onto the backlighter target. With the upper portable interferometer the plasma density distribution is imaged. The second greyed-out interferometer does not see the shocked target.

The portable interferometer is a Talbot interferometer, which is realized with two precisely aligned gratings, G_1 and G_2. The x-ray photons are detected with analog imaging plates. The adjusting process of the two gratings G_1 and G_2 is a time consuming process, where the distance between the two gratings as well as the angles between them need to be adjusted accurately. As this has to be done iteratively, performing this process is neither feasible nor economic at backlighter sources like PHELIX, where the time between shots is approximately 2 hours, see [SLA+19]. As the distance between the two gratings is in the magnitude of 100 mm, it is possible to build a portable Talbot interferometer, which can be adjusted at the ECAP facility and transported to the research facility, see [SLA+19]. As mentioned in the introduction, the design and characterization of this portable interferometer is one of the key points of this thesis. Before explaining the conceptualization in detail, an overview over the portable interferometer is given, which is shown in Figure 3.2.

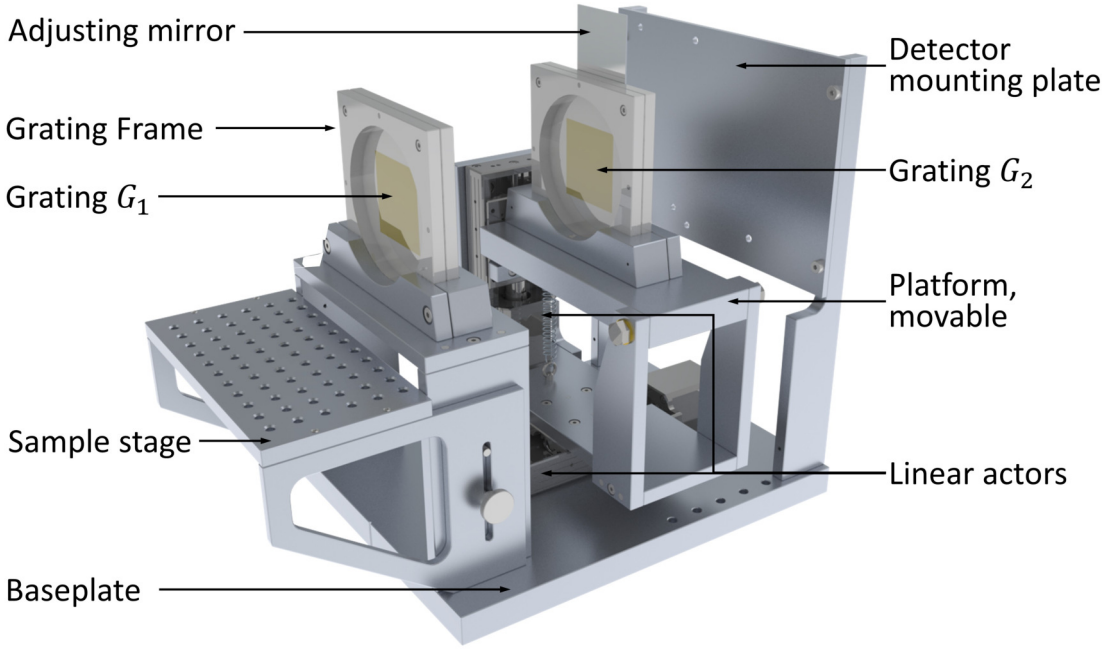

Fig. 3.2: 3D-render of the portable Talbot interferometer. The sketches of the linear actors were taken from [Phy20].

With its dimension of (390 × 230 × 320) mm, L × W × H and a weight of under 10 kg the interferometer is compact. It consists of five main components:

- The gratings G_1 and G_2, mounted in grating frames.
- Two platforms, on which the grating frames are mounted. The one for G_1 is fixed onto the baseplate, the G_2 platform is movable.
- The detector mounting plate
- A large sample stage
- An alignment mirror

The grating frames are used to hold the gratings, protect and stiffen them to avoid any kind of damages. With two linear actors the platform of G_2 can be tilted and moved relative to G_1. Due to the stepper motor and a reference switch, the installed linear actors allow a highly precise and reproducible positioning. The tilting angle of G_2 can be adjusted in the range of mrad. The inter-grating distance can be adjusted in the order of sub mm. This allows a flexible and precise adjustment of the moiré fringes. The detector mounting plate is designed in such a way, that different types of detectors can be mounted easily. Only new holes have to be drilled into the large aluminum plate so that the detector can be bolted into place. The distance between the detector mounting plate and the grating G_2 can be adjusted in a 20 mm spacing. So the optimal distance between the grating G_2 and

the detector can be found easily at any time. With the height adjustable sample stage, samples of various dimensions can be investigated without having to make major changes to the setup. Due to the precise grid of 5 mm fits, samples and object mounts can easily be positioned flexible and precise. For an easy alignment during the beam time experiment, a mirror is mounted on the top of the G_2 grating frame.

3.2 Mechanical required specifications

A Talbot interferometer consists of two gratings G_1 and G_2. To acquire the desired moiré pattern, the distance between the two gratings as well as the angles between them need to be adjusted accurately. This is an iterative process which is controlled by evaluating the observed moiré pattern after every adjustment step. That means a large number of images have to be taken during the adjustment process. This is neither feasible nor economic at backlighter sources like PHELIX, where the time between shots is approximately 2 hours, see [SLA+19]. So, the interferometer needs to be portable.
The adjusted Talbot interferometer will be transported form the ECAP facility in Erlangen to the GSI facility in Darmstadt over 200 km by car. Thus a robust setup is mandatory, where the performed adjustments do not get altered due to vibration or small impacts. To damp these disruptive factors, the interferometer will be put into a wooden transport box, lined with polystyrene. To increase the handiness, a compact and lightweight setup is striven for.
At the PHELIX facility, the interferometer will be put into a vacuum chamber with an ambient pressure of approximately 10^{-6} mBar. So, according to [Zie20] the whole setup including all components and materials have to meet high-vacuum standards regarding cleanliness, outgassing of materials, lubrication, as well as venting of internal cavities.
The beam height at PHELIX is 360 mm, whereas the beam height of the x-ray tube used for the adjustment process is 225 mm. The interferometer has to cover both heights and should be firmly lockable at both heights, to prevent any movements during the experiment. Near the correct height, the setup has to be correctly aligned to the beam. A good alignment avoids shadowing and a loss of visibility in the moiré pattern, see [Sch16]. Therefore a good and reliable routine has to be found to properly align the setup to the backlighter at the PHELIX facility.
The mounting method for the gratings should have a high repeated accuracy. This is based on the circumstance that multiple grating sets are available. Depending on the imaging performance of the preselected grating at the backlighter, they maybe have to be changed during the experiment. But by changing the gratings, the adjustments which were made for the former gratings are worthless. If the mounting method of the gratings has a high repeated accuracy, the Talbot interferometer could be adjusted once for all relevant grating combinations. The final distances and angles could be measured and saved. This allows

a huge flexibility concerning the use of the gratings without wasting any time for the adjustment process.
For the experiment at PHELIX facility imaging plates, are used as an x-ray detector. For read out the IPs have to be brought to a special scanner (see subsection 2.2.2). Thus the IPs have to be exchanged after every shot. A high repeated accuracy for the placement of the IPs is beneficial for image reconstruction [Sch21]. Near the x-ray radiation, the backlighter emits charged particles. These particles generate secondary radiation when hitting matter, e.g. the walls of the target chamber. This radiation is also detected by the IPs. To reduce this background signal on the images a shielding is required.

3.3 Theory based specifications

For the portable interferometer a π-shifting phase grating will be used as a G_1. Compared to $\pi/2$-shifting phase gratings and absorption gratings this choice has got a few advantages. As stated in section 2.3.1, phase gratings ideally do not absorb any radiation, whereas absorption gratings reduce the mean intensity by a factor of ≈ 0.5. So, phase gratings are preferable in terms of maximizing the photon flux. Compared to $\pi/2$-phase gratings, π-shifting phase gratings form a Talbot pattern with doubled frequency. To generate a Talbot pattern with the same period, the period of the π-shifting grating can be twice as large as the $\pi/2$-phase gratings. A larger period is beneficial concerning production uncertainties during the process of grating fabrication. For $\pi/2$-phase gratings the first moiré pattern appears already at $d_T/16$ (see Figure 2.4). So, $\pi/2$-shifting phase gratings provide more possible geometries compared to π-shifting phase gratings where the first repeated structure appears at $d_T/4$.

	Grating specifications				Waver specifications	
	type	period [µm]	material	height [µm]	material	thickness [µm]
G_1	π-shifting	10	SU-8	25	polyimide	500
G_2	absorption	6	Gold	150	graphite	500

Tab. 3.1: Overview over the specifications of the grating G_1 and G_2. Note that three G_2 wavers are made from graphite and one from conductive varnish.

As the induced phase shift of a phase grating is wavelength dependent, the grating has to meet the correct dominating energy. According to [SWC+], the expected dominant energy at the PHELIX facility is between 11 keV and 12 keV. So, hereinafter all theory based calculations are performed with an energy of 12 keV.
The chosen grating G_1 has a period of 10 µm and consist of photoresist. All specifications are tabulated in Table 3.1. The design energy of this grating can be calculated to 11.2 keV, see fig. A.1 on page 83 in the appendix. This is well suited for the expected dominating energy. As stated in section 2.3.1 the Talbot period p_T as well as the fractional Talbot

distances d_{fT} get magnified in a cone beam geometry. So, the analyzer grating G_2 needs a period of $\gtrsim \frac{p_{\mathrm{G1}}}{2} = 5\,\mu\mathrm{m}$. The only suitable and available absorption grating has a period of 6 µm. Now, that the gratings are chosen, all distances for conceptualizing a Talbot interferometer can be calculated.

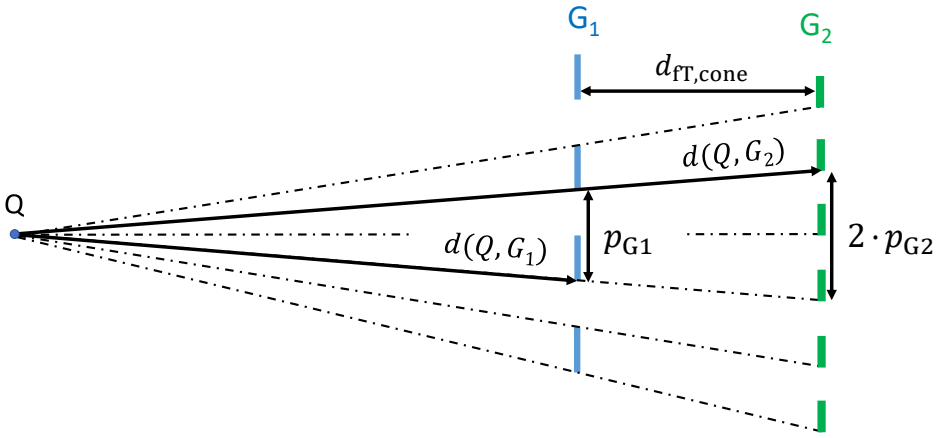

Fig. 3.3: Schematic sketch of the Talbot setup in a cone beam geometry. All relevant distances to calculate the final dimensions of the setup are indicated. The period p_{G2} of the grating G_2 does not follow a simple magnification of G_1. This is due to the frequency doubling character of a π-shifting grating, see Figure 2.4 .

In Figure 3.3 a schematic sketch of a Talbot interferometer in a cone beam geometry can be seen. On the left side is the point like source Q located. The grating G_1 is placed in a distance $d(Q, G_1)$ to the source and the grating G_2 in a distance $d(Q, G_2)$. To observe the desired moiré pattern, the periods of the Talbot pattern and the period of G_2 need to be approximately the same. Hence, for the magnification M must hold

$$p_{\mathrm{fT,cone}} \stackrel{!}{=} p_{\mathrm{G2}} \tag{3.1}$$

$$\frac{p_{\mathrm{G1}}}{2} \cdot M = p_{\mathrm{G2}}, \tag{3.2}$$

where p_{T} was replaced with the period of the chosen G_1 grating. Inserting the tabulated periods results in a required magnification M of 1.2. According to the intercept theorem, the magnification of the setup sketched in Figure 3.3 is calculated by

$$\frac{d(Q,G_2)}{d(Q,G_1)} = \frac{2\cdot p_{\mathrm{G2}}}{p_{\mathrm{G1}}} = M = 1.2 \tag{3.3}$$

As the Talbot pattern appears and disappears periodically, the grating G_2 needs to be placed ideally where the Talbot pattern is visible. So, for the distance between the gratings must hold

$$d(G_1,G_2)_{\mathrm{opt}} \stackrel{!}{=} M \cdot d_{\mathrm{fT}} = M\frac{(2m-1)p_{\mathrm{G1}}^2}{8\lambda} \qquad m \in \mathbb{N}, \tag{3.4}$$

with d_{fT} as the fractional Talbot distances, see Equation 2.20. Rewriting Equation 3.3 with $d(Q, G_2) = d(Q, G_1) + d(G_1, G_2)$ and inserting Equation 3.4 leads to an expression for $d(Q, G_1)$

$$d(Q, G_1)_{\mathrm{opt}} = \frac{d(G_1, G_2)}{M-1} = \frac{M}{M-1} \cdot \frac{(2m-1)p_{\mathrm{G1}}^2}{8\lambda} \qquad m \in \mathbb{N}. \tag{3.5}$$

With Equation 3.4 and Equation 3.5 two expressions were derived to calculate the distances of the interferometer. In Table 3.2 the distances are tabulated for the first three orders $m = 1, 2, 3$ and a wavelength λ corresponding to a photon energy of 12 keV. As the target chamber at the PHELIX facility is 2040 mm wide and 1280mm deep, only the first order $m = 1$ can be used.
With the theory based and mechanical specifications outlaid, the portable interferometer is designed in the following.

order m	$d(Q, G_1)_{\mathrm{opt}}$ [mm]	$d(G_1, G_2)_{\mathrm{opt}}$ [mm]	$d(Q, G_2)_{\mathrm{opt}}$ [mm]
1	726	145	871
2	2178	436	2613
3	3629	726	4355

Tab. 3.2: Overview over the three shortest distances which fulfill all theory based requirements. The overall dimensions of the Petawatt target chamber at the PHELIX facility only allow the first order configuration.

3.4 Conceptualization

Positioning of the gratings

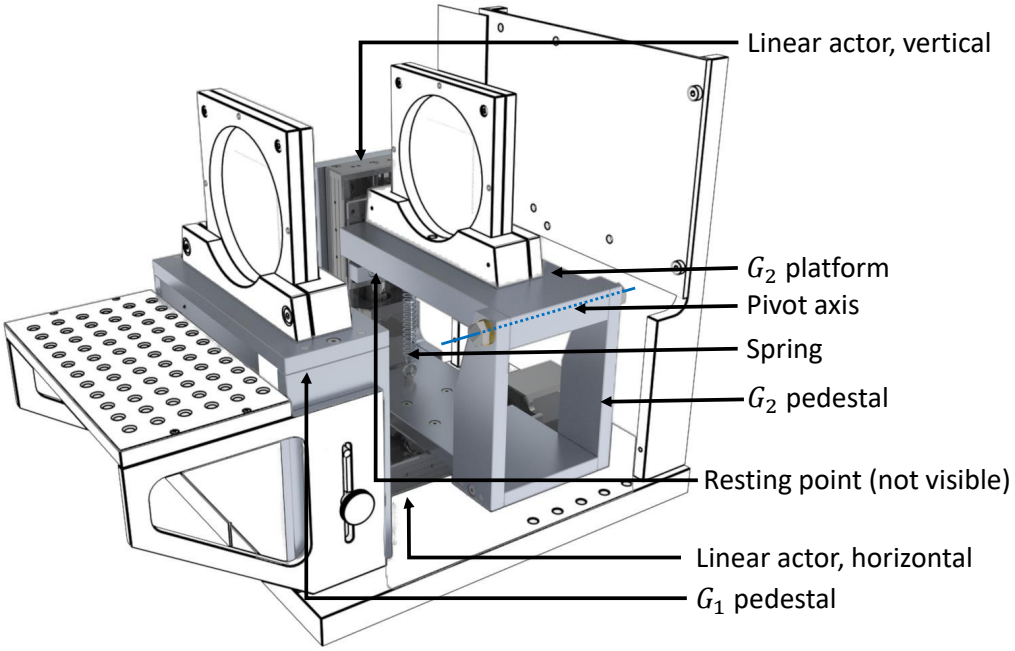

Fig. 3.4: 3D-render of the portable setup. The parts discussed in this section are highlighted. The whole G_2 pedestal can be moved with the horizontal linear actor. The G_2 platform can be tilted with the vertical mounted linear actor. The G_2 rests on a rigid pedestal.

To adjust the periodicity and the angle of the moiré pattern, two parameters need to be tunable. Namely the relative tilting angle α and the deviation of the periods $p_{\mathrm{fT,cone}}$ to p_{G2}, see Figure 2.6. These parameters can be changed in various ways. In Figure 3.4 the relevant components for the grating adjusting mechanism can be seen. As the grating period of G_2 is fixed, only the period of the Talbot pattern $p_{\mathrm{fT,cone}}$ can be changed. This can be done, according to the intercept theorem (see Equation 3.3), by changing either the distance $d(Q, G_1)$ or $d(G_1, G_2)$. As the Talbot distance $d_{\mathrm{fT,cone}}$ depends on $d(Q, G_1)$, the grating G_2 would move out of the Talbot distance when the grating G_1 is moved. This will result in a reduction of visibility, as the Talbot pattern is best visible in the Talbot distance. So, changing the distance $d(G_1, G_2)$ and keeping the distance between the source Q and the Grating G_1 constant is the better choice. A linear stage with a stepper motor and a reference switch provides an easy to use, precise and higly repeatable accuracy in positioning the grating G_2. The portable interferometer should be flexible in the ability of using different gratings with various periods. This dictates that the Grating G_2 must be positionable at different optimal Talbot distances. A linear stage with a travel range of 50 mm provides a sufficently large range of adjusting range. With this stage, the distance $d(G_1, G_2)$, is adjustable between 120 mm and 170 mm.

Near the deviation of the periods, the angle between the periods of the Talbot pattern and the G_2 needs to be adjustable. This can be done by either tilting G_1 or G_2. The effect of either tilting G_1 or G_2 on the visibility was tested by [SGH+17] for a Talbot-Lao setup. The visibly is higher when the grating G_2 is rotated and the G_1 stays fixed. The easiest and most reliable way to achieve a tilting of G_2 is, to mount the grating onto a tiltable platform. This platform can rotate around a tilting axis, marked with a blue line. The other side of the platform rests on a bearing point (not visible in the figure). This bearing point can be moved up and down, as it is mounted on the vertical linear actor. This vertical movement translates to a tilt of G_2. The spring between the platform and the bottom of pedestal ensures a constant and continuous positioning of the platform on the bearing point. The chosen linear stage has a travel range of 25 mm. This covers an angular range, wider than that required for adjusting the desired moiré pattern. But as the orientation of the grating bars of the G_2 are not known exactly, it is beneficial to be able to set a wider angular range.
Previous experiments have shown, that an accuracy of at least 0.32 mrad for the tilting and a step width of 0.25 mm for the horizontal movement is required. The chosen linear stages are purchased from Physik Instrumente. A full list of all relevant specifications can be found in the appendix A on page 87. The design resolution of the stage is 0.005 mm. This is sufficient for the horizontal positioning. The resolution for the tilting is 0.028 mrad. This results from the tangent of the bidirectional repeatability and the distance between the tilting axis and the supporting pin, which is 174, 6 mm.
To be able to meet the beam height at the PHELIX facility and the one in the ECAP facility, the height of the pedestal is optimized for the lower one. Hence, the center of the grating is at 225 mm, the beam height of the ECAP facility. To meet the height at the PHELIX facility the interferometer is put onto a pedestal with a height of $\Delta h = 135$ mm. This pedestal consist of a breadboard and 1" optical post assembly that can be built with an accuracy of 1 mm steps. This accuracy is acceptable, as the gratings have a larger field of view than required for the experiment.

Grating mounting bracket

The gratings, used for the experiment at the PHELIX facility, are fabricated by the Karlsruhe Nano Micro facility. The grating structures are built on a substrate with a diameter of 100 mm, see Figure 3.5 (a). These gratings are placed into a clamping frame. This reduces the risk of possible damages. Further more the clamping surface of the frames can be fabricated with a radius. This allows to imprint a curvature onto the gratings. These grating frames will be investigated in section 4.2. Due to the rectangular shape of the clamping frame, the position in the mounting socket is always the same. So, the clamping frame with the grating can be removed without loosing the parameters for the adjustment. The mounting socket is bolted onto the platform. The through-hole in the platform has got a slight play. This play allows the correction of slight miss alignments of the gratings, regarding their parallelism.

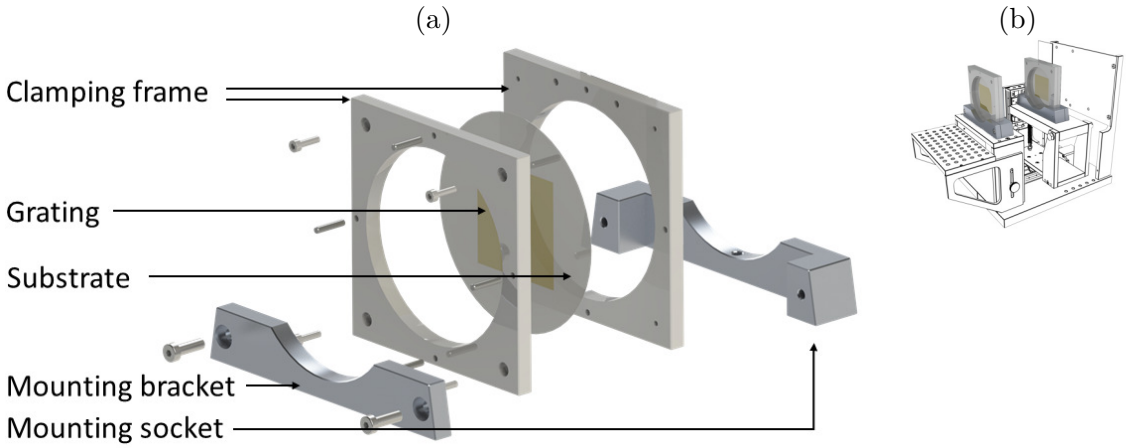

Fig. 3.5: (a) Exploded assembly view of the grating frame and the mounting socket. The gratings are put into a clamping frame. This frame is in turn fastened to the platforms of the setup with the mounting socket. (b) Mini map of the portable setup.

Detector mounting

The detector mounting has to to be capable of holding at least two different detectors. A digital CMOS detector for the measurements in the ECAP facility and analog IPS at the PHELIX facility. A detailed description of the functionality of these detectors can be found in subsection 2.2.2.

The detector mounting is realized with a 2 mm thick sheet of aluminum, see Figure 3.6. Various detectors can be mounted easily onto this sheet. Therefore, new holes have to be drilled in the positions, where the mounting holes from the detectors are.

With its overall large dimesnions of 230×300 mm even detectors with a large field of view can be mounted to the sheet. The sheet is mounted onto two posts. These posts are not bolted onto the baseplate. Instead, the posts are connected via four positioning pins with

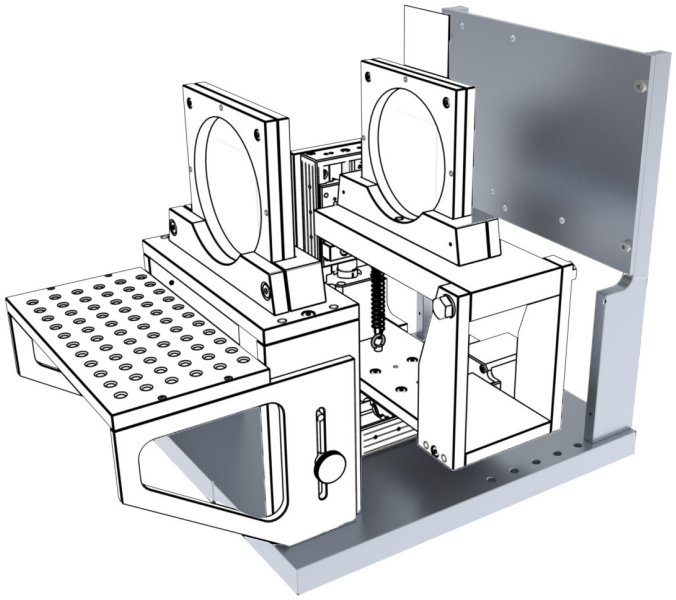

Fig. 3.6: Detector mounting concept. Various detectors can be bolted onto the large detector mounting plate. Only new holes have to be drilled in the required positions. The hole grid allows a flexible positioning of the gratings.

the base plate. As the holes in the baseplate are designed as a clearance fit, the detector mounting can be removed. Due to the spaced hole grid, the detector can be placed in 20 mm increments to the grating G_2. This is beneficial, when different distances between G_1 and G_2 are required.

As the digital detector is ready to use, it only needs to be bolted into place. Because IPS are erased by exposure to visible light, they have to be stored, before, after and during the exposure of x-rays, in a light-sealed enclosure. Figure 3.7 shows, an individually designed case for storing and transporting the IPS.

The Fuji BAS type SR Imagine plates are $\approx 0.5\,\mathrm{mm}$ thick and come in sheets of $200 \times 400\,\mathrm{mm}$. These sheets can be cut in the desired dimension. The required active area for the experiment can be estimated using

$$A_{\mathrm{Ip}} \gtrsim M_{\mathrm{d(G2,IP)}} \cdot \underbrace{\left[(M \cdot A_{G1}) \cap A_{G2}\right]}_{A_{\mathrm{overlap}}}. \tag{3.6}$$

With a magnification factor $M_{\mathrm{d(G2,IP)}}$ and the overlap area of the active areas of the two gratings A_{overlap}. Here $M \cdot A_{G1}$ denominates the active area of the grating G_1 in the G_2 plane. The magnification factor $M_{\mathrm{d(G2,IP)}}$ comes from the fact, that A_{overlap} is further magnified into the detector plane. $M_{\mathrm{d(G2,IP)}}$ can be calculated using the intercept theorem and by assuming a distance of ≈ 75 mm for $d(G_2, \mathrm{IP})$. An area of 100×80 mm provides enough area of the image, as well as features such as the ECAP logo and the placing jag. These features are used to match the digitized object and reference measurement. As the

whole IP holder is brought to a special read out scanner, a fast and reliable way to place the IP holder in the setup is required. The whole IP holder is placed with two dowel pins onto the plug-in mount. This mount is firmly bolted onto the detector plate. This method provides a positioning precision in the µm range.

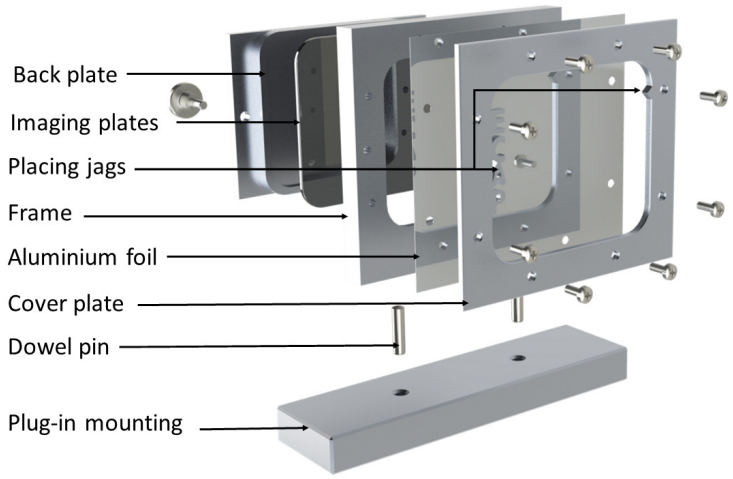

Fig. 3.7: Exploded assembly view of the IP holder and the plug-in mounting socket. The IPS are put into the frame and held with the back plate in place. The thin aluminum is used to protect the IPS from visible light.

As the Imaging plates do not absorb all x-ray photons, further IPS can be used to detect the remaining photons. The presented IP holder is flexible enough to hold up to five IPS. This is achieved by a picture frame like setup. Multiple IPS can be put into the frame and are pressed by the back plate against the front of the frame. To remove the IPS, only the back plate needs to be unbolted with two knurled thumb bolt. The IP needs to be protected from visible light. According to [Saf20] a higher photon flux increases the signal to noise ratio of the images. So, a low absorbing and opaque cover is required. A 0.008 mm thick aluminum foil is, with a relative transmission of $\approx 96\,\%$, compared to other opaque and available materials, the one with the lowest absorption. A plot of the relative transmission of different materials can be seen in fig. A.2 on page 84.

Sample Stage

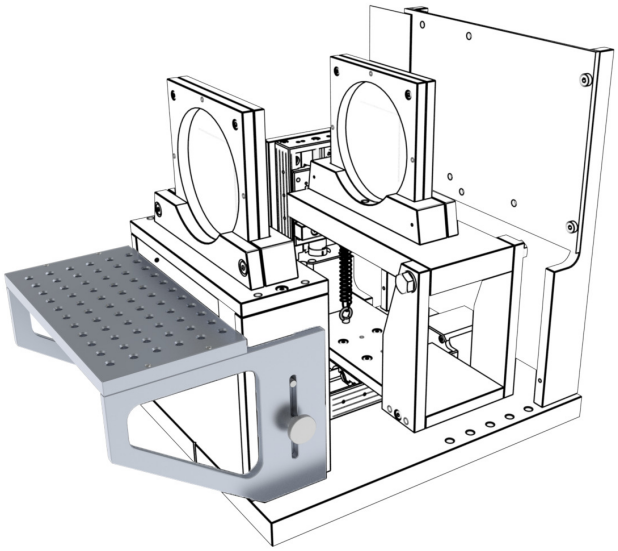

Fig. 3.8: The concept of the positioning of the sample stage is adapted from optical breadboards. The precise grid of 5 mm fits provides a flexible and precise positioning of different samples.

As this portable interferometer will be used after the experiment at the PHELIX facility, the sample stage should provide a huge flexibility concerning mounting various samples. The platform has a dimension of $187 \times 95\,\text{mm}$. So large objects and linear stages can be placed safely onto the stage. With the slotted holes on the side the stage can be moved up and down by $\approx 40\,\text{mm}$. This helps to position the objects vertically in the desired height. As the stage provides a grid of 5 mm fits, specifically designed object mounts can repeatably and accuratly be placed at the exact same location.

Alignment mirror

Near the correct adjustment of the gratings, the whole setup needs to be aligned correctly into the beam, as a slight missaligned G_2 causes a reduction of visibility, see [Sch16]. If the incident angle ϑ of the x-rays is 90°, the G_2 is perfectly aligned, see Figure 3.9 (b) case I. In case II, the grating G_2 is rotated and the incoming x-rays will hit the grating bars. This will happen even at very small rotations, as the used G_2 has a period of 6 µm and a height of 150 µm. This will decrease the intensity as these bars are highly absorbing. This effect is called shadowing. This effect reduces the visibility of the moiré pattern. The alignment process, which is explained later in detail, is an iterative process. The adjusting steps are controlled by evaluating the intensity distribution. This is, similar to the grating adjusting process, not feasible at backlighter sources. So, the correct alignment has to be determined at the ECAP facility and transferred to the PHELIX facility. This is done with

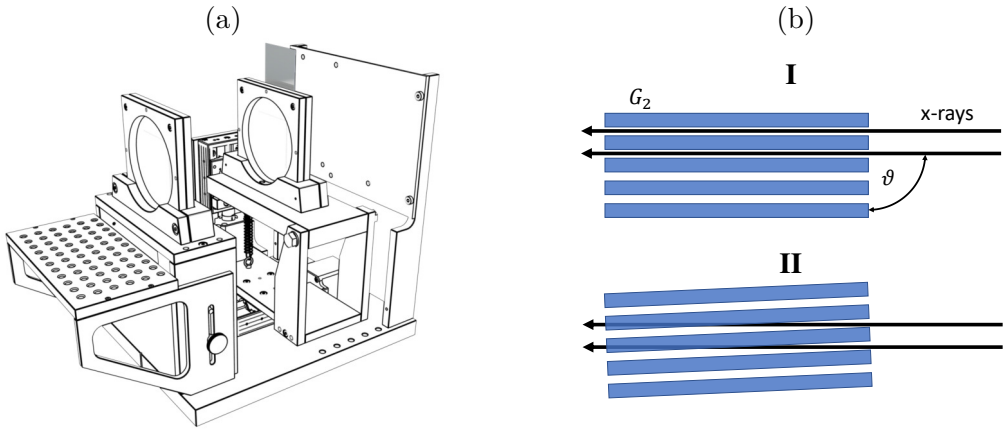

Fig. 3.9: (a) Render of the portable Talbot interferometer. The highlighted mirror is used to align the setup correctly into the x-ray beam. (b) Visualization of a good and a bad aligned G_2 (not to scale). In case I, the x-rays don't hit the grating bars when they enter a gap. In case II, they will hit the bars and thus the intensity gets reduced.

the adjusting mirror, which is mounted on top of G_2, see Figure 3.9. According to Snell's law, the angle of incidence is equal to the angle of reflection. So, if e.g. a laser beam gets reflected into the source point the incident angle is exactly 90°. This is exploited for the alignment process. A commonly available cross-line laser is set up in a manner, that the laser follows the propagation path of the x-ray beam. Then the whole setup is rotated in such a way, that the reflected beam falls back into the source point. If the mirror is parallel to the grating bars, the interferometer can be aligned even without presence of x-ray radiation.

As the grating surface is sensitive, the parallelism of the mirror to the grating surface can't be measured with at the ECAP facility available mechanical devices. So another way has to be chosen to ensure the parallelism. As an initial step, the correct alignment of the portable setup has to be found iterative. To ensure that the measured intensity only depends on the orientation of the G_2, the grating G_1 is removed. Then the whole setup is rotated slightly. This changes the incident angle ϑ of the x-ray, see Figure 3.9 (b). When the incident angle is 90°, the intensity reaches a maximum. When the optimal orientation is found, a cross-line laser is set up in a way, that it follows the path of the x-ray beam. The mounted mirror will reflect parts of the laser light. As the setup is aligned correctly, the mirror has to be mounted in a way, that the location of the back reflection is the same as the source of the laser. To achieve this, the mirror can be shimmed with thin metal plates. As the mirror is mounted on top of G_2, a later adjustment at the PHELIX facility can be performed, without removing the grating G_1.

Shielding of the Interferometer

As mentioned in section 2.2, the backlighter emits x-ray photons up to 10^3 keV and charged particles. If these particles hit e.g. the walls of target chamber, secondary x-ray radiation is generated. This secondary radiation is also detected by the IPS. This radiation only contributes to the background, as the radiation is not emitted from the backlighter itself. To avoid noise, originated from the secondary radiation, the angle of acceptance has to be narrowed down, so that only the relevant area is in the field of view of the IPS. This was accomplished by using a box, which covers parts of the interferometer. The outer side of the box is covered with 2 mm of lead. This layer has got a relative transition of less than 0.0001 % up to a photon energy of 70 keV, see fig. A.3 on page 84 in the appendix. But when high energy photons hit matter, secondary x-ray photons can be produced, the so-called x-ray fluorescence. According to [XRL20] the characteristic photon energies for lead are 9.18 keV, 10.55 keV, 12.61 keV and 14.76 keV. In this energy range the aluminum has a relative transmission of less than 0.0001 %, see fig. A.3 on page 84. Thus almost all primary and secondary radiation gets blocked by the shielding.
This box fits between the grating G_1 and G_2, see Figure 3.10. As the Imaging plates have to be exchanged after every shot, the rear side is kept open. From the front side, radiation can only enter through a hole. So, the Imaging plates are almost exclusively irradiated by the backlighter.

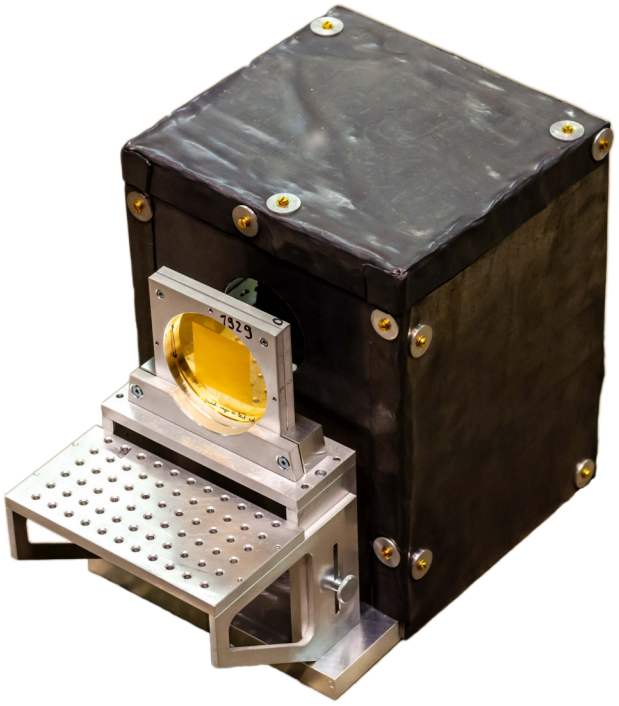

Fig. 3.10: Photography of the portable setup, covered by the designed shielding. The covering side is made of 2 mm lead which is bolted onto a construction of 2 mm aluminum.

3.5 Concluding remarks and outlook

In this chapter, all steps that have to be considered to design a portable Talbot interferometer have been explained. All requirements which were stated in section 3.2 and section 3.3 can be met with this setup. During the extensive usage at the experiment at the PHELIX facility a few improvements were developed, which could be realized for further experiments. Following these ideas are presented briefly.
For optomechanical components devices 6 mm dowels and bolts are state of the art. In the sample stage (see Figure 3.8) only 5 mm though holes are available. This prevents an easy use of these components. So 6 mm fittings would be beneficial for the sample stage.
The motorized axes have an analog scale that indicates the current position. In case of a break down of the digital read out, there are no good positions available where the current positions can be measured. A simple pointer bolted onto the G_2 pedestal and the platform (see Figure 3.4) can solve this problem. At the ECAP facility all relevant positions can be set and marked. Then the actual position of the pointer can be marked with a permanent marker.

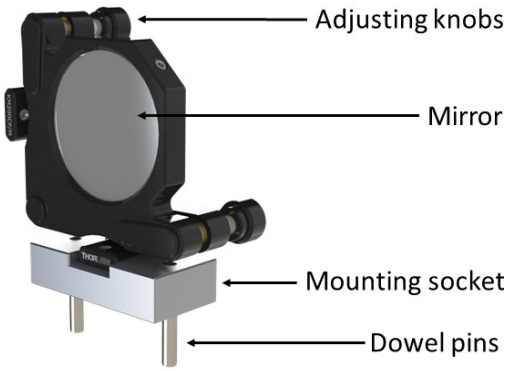

Fig. 3.11: Alternative to the adjusting mirror, placed above the grating G_2 (see Figure 3.9 (a)). The mounting socket connects the sample stage with a precise adjustable mirror. These so called kinematic mirror mounts can be purchased at any optic supplier. The sketch of this mirror mount was taken from [Tho20].

The position of the adjusting mirror (see Figure 3.9 (a)) is not optimal. All other optical devices which were needed during the experiment are aligned using a laser pointer. This laser pointer irradiates in the height of the backlighter beam. As the position of the mirror is ≈ 60 mm higher, there is no way the laser pointer can be used. So the cross-line laser has to be set up precisely. This is, besides the laser safety requirements at the PHELIX facility, challenging. Further more the adjusting of the mirrors using shims is a time consuming and tricky process. In Figure 3.11 an alternative realization of the concept of the adjusting mirror can be seen. With the dowel pins the component can be placed onto the sample stage. With the adjusting knobs the mirror can be easily and precisely adjusted in the x-ray laboratory of the ECAP facility. The principle of adjusting the mirror stays the same,

as explained in section 3.4. With positioning the component onto the sample stage, the center of the mirror coincides with that of the gratings. So, the adjusting laser pointer can be used.

A further feasible improvement can be a modified IP holder. The proposed concept of this holder differs from the used one significantly and only works when the lights can be turned of in the target area. The used IP holder, see Figure 3.7, is designed to serve as a holder as well as a carrying cassette. The holder will be brought to the IP scanner, which is located in another building. There, the IPS are exchanged and the holder is brought back. As long as this procedure lasts, the target chamber needs to stay opened. This time vanished, when the proposed holder is used. As in Figure 3.12 (a) shown, the holder consists of a spacer tube, an IP frame and a back plate. The IPS frame is bolted firmly onto the rear grating frame of G_2. The spacer tube provides enough space between the IP frame and the rear grating frame, so that it can be clamped onto the mounting socket (see Figure 3.5). The IP frame fits snugly in the notch between the IP frame and the Back plate. The slit between the back plate and IP frame, see Figure 3.12 (b) can be sealed when a small L-shaped aluminum sheet.

To exchange the IP, it has to be pulled out and put into an x-ray cassette. During this process the lights in the target chamber have to be turned off to avoid an extinction of the IP. Another advantage is the absence of any further covering material. The 8 µm thick aluminum foil is replaced with the waver of the grating G_2. So, the absorption of $\approx 4\,\%$ can be avoided.

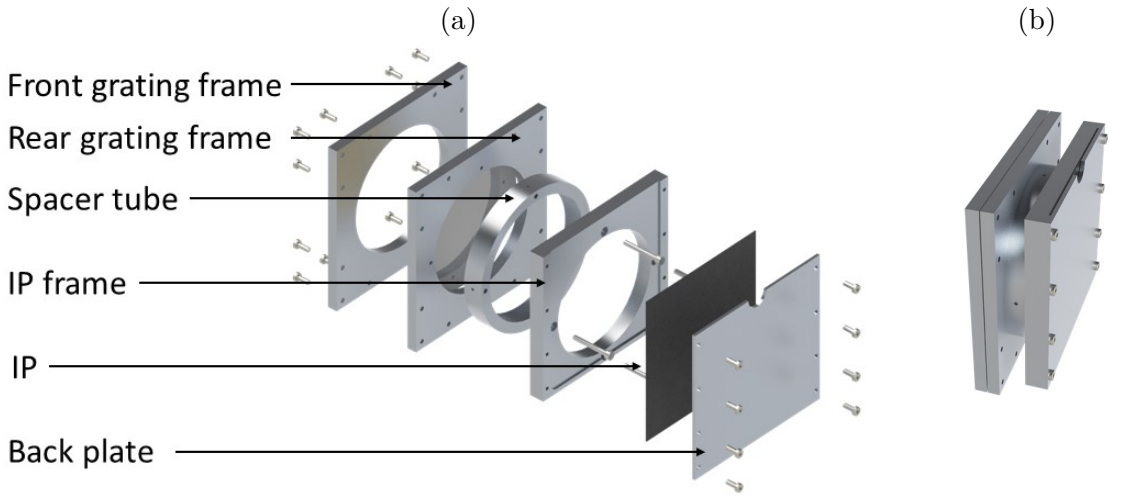

Fig. 3.12: (a) Expansion view of a possible improved IP holder. (b) Render of the assembled view of the improved IP holder.

4 Characterization of the interferometer

A newly designed interferometer, equipped with gratings never tested before, is not ready to use. It has to be tested and characterized before making quantitative investigations. This requires a large number of different measurements. Two main focuses are set here. The first focus is a general characterization of the interferometer and the gratings so that the interferometer is brought to a level where it is ready to use. These experiments are adapted to beam time experiment and aim to improve the imaging quality of the setup. The second focus is the investigation of the reconstruction process for moiré imaging. These experiments are independent from a specific application, and focus on a deeper understanding of the moiré reconstruction process. The experiments build on each other and use the results of the previous ones. At the end of each subsection a short summary of the findings is given.

4.1 Evaluating possible grating combinations

For the portable interferometer two G_1 gratings and four G_2 gratings are available. The gratings only differ in the used waver material and their characteristics, caused by the fabrication process. An overview over all grating parameters can be found in table A.3 on page 88 in the appendix. With these gratings eight combinations are possible. Each combination is investigated regarding their imaging quality. As a measure for the quality, the visibility of the moiré fringes is chosen. The visibility of a moiré pattern depends on the period (see [SGH+17]). By comparing the same relative positions between the gratings G_1 and G_2, the best grating combination cen be determined. These measurements and evaluations are performed for every grating combination with the acceleration voltages 25 kVp and 45 kVp. This makes it possible to check which effects different acceleration voltages and thus different x-ray spectra have onto the visibility of the moiré pattern.
At first the interferometer needs to be adjusted. The actual grating structure is applied to a thin waver that is ideally invisible to x-rays. To mount the grating into the frame, the grating is clamped between two clamping frames (see Figure 3.5). The grating bars have to be parallel to one side of the frame. The direction of the grating bars is marked on the waver. The prepared grating frames are mounted into the interferometer. The calculated distances between the source and the grating G_1, $d(Q, G_1)$ and the distance between the grating G_1 and G_2, $d(G_1, G_2)$ need to be adjusted (see section 3.3). The distance $d(Q, G_1)$ is set by placing the whole portable setup relative to the x-ray tube. This can be done on a mm scale by measuring the distance with a measuring tape. To get the correct distance between the two gratings, G_2 can be moved with the horizontal linear stage. Now a moiré pattern should be visible when the x-ray tube is turned on. If not, the distances are wrong

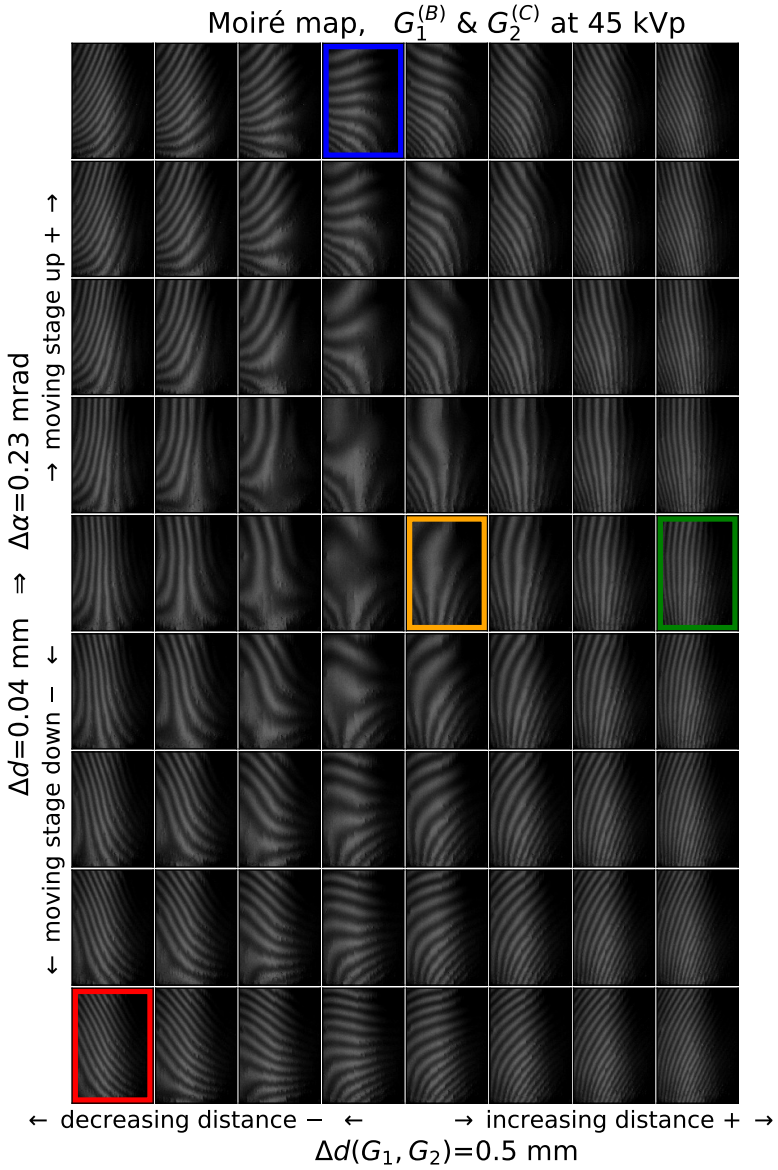

Fig. 4.1: Moiré map of the grating combination $G_1^{(B)}$, $G_2^{(C)}$. The horizontal axis shows the change of distance between $G_1$and G_2. The grating G_2 is shifted by 0.5 mm between each horizontal image. The vertical axis shows the relative angle α between the grating bars of G_1 and G_2. G_2 was tilted by 0.23 mrad between every vertical image. The colored frames indicate which frames are used to determine the best grating combination. Own figure and measurements, adapted from [SLA+19].

or the angle between the grating bars is too large. Assuming the distances are correct, the angle between the grating bars has to be adjusted. The portable interferometer allows a fine adjusting range of 8.1° by tilting the grating G_2 with the vertical linear stage. If the moiré periods get larger and smaller again, the grating is placed correctly into the frame and the interferometer can be further adjusted. If the moiré period only gets larger, smaller or is not visible at all, the grating G_2 has to be rotated manually in the grating

frame. The correct angle is found where the moiré period is at its maximum. Further, the grating distance can be varied to enlarge the moiré period. This variation is usually in the order of mm. The angle and the distances can be varied iteratively until the moiré period does not get larger. In the following experiment, the positions of the correctly adjusted interferometer are also called the optimal setting, $d(G_1, G_2)_{\text{opt}}$ and α_{opt}.
This process is performed for all eight grating combinations. With the adjusted interferometer a moiré map can be acquired. The moire map gives a structured arrangement of reference frames for one specific set of gratings (see [SLA+19]). Exemplarily a moiré map for the grating combination $G_1^{(B)}$ and $G_2^{(C)}$ is shown in Figure 4.1. The map covers a deviation in the grating distance of 3.5 mm on the horizontal axis and a change in the grating angle of 2.06 mrad on the vertical axis. To acquire these images, the grating G_2 is shifted by 0.5 mm between each horizontal image and tilted by 0.23 mrad between each vertical image. By taking a look at a single reference frame it can be seen that not all moiré fringes are straight. The period of the pattern also changes within one image. This distortion is caused by small inaccuracies in the parallelism of the grating planes. In addition it unfolds that due to the distortion of the moiré pattern the real optimal position is hard to determine. For the shown moiré map the orange boxed image was taken to be the maximum. Comparing this image with the one to the left side, the real maximum could be in between.
Four points or relative axis positions were selected from the moiré maps to determine the visibility. These selected points are colored and selected due to their position in the moiré map. The orange framed image is the position, where the interferometer is best adjusted. The green image shows a relative shift of G_2 to the orange one, the blue one a tilting and the red a combination of tilting and shifting. The periodicity of the moiré pattern is large. The zeroth and first order peaks in the frequency spectra (see Figure 2.10) can not be separated. The visibility can not be determined using the reconstruction algorithm. For the selected reference frames the visibility is determined using Equation 2.24

$$V = \frac{I_{\text{max}} - I_{\text{min}}}{I_{\text{max}} + I_{\text{min}}}.$$

I_{max} and I_{min} were calculated by taking the average of four maxima and minima, respectively. The error of the visibility was calculated by the standard error of the mean intensity values. As can be seen in the reference images in Figure 4.1, shadowing occurs (see section 3.4). Due to this effects the mean intensity is not constant over the whole image of the grating surface. This effects the standard deviation and thus the standard error of I_{max} and I_{min}. Thus the error of the visibility is also effect from the shadowing of the grating. All derived visibility values are visualized in two bar charts in the appendix, fig. A.4 on page 85. But as an equivalent result can be drawn from comparing only one specific reference frame, for the sake of clarity only the image marked red in Figure 4.1 is used. The visibility of this frame

is shown in Figure 4.2 for all grating combinations. The vertical axis shows the visibility, the horizontal axis all possible grating combinations. The blue bars show the visibility of the moiré pattern with an acceleration voltage of 45 kVp and the orange bars the visibility gained with the 25 kvP. For the first four bar combinations the $G_1^{(A)}$ was used. For the remaining four combinations the $G_1^{(B)}$ was used. It can be seen that visibilities gained with the phase grating $G_1^{(A)}$ tends to be lower. By comparing the combinations with $G_1^{(B)}$, it can be seen that $G_2^{(B)}$ has, for both acceleration voltages the highest visibility. The moiré pattern resulting from $G_2^{(B)}$ and $G_2^{(D)}$ has a cloudy appearance (see table A.3 on page 88). At these cloud structures the moiré pattern has small discontinuities. It is not known how much these discontinuities affect the imaging at a backlighter source. Hence, the gratings $G_2^{(B)}$ and $G_2^{(D)}$ are not considered any further. Due to fabrication issues the grating $G_2^{(A)}$ only has got a reduced grating surface and a wavy thickness. This renders the grating, besides the lower visibility, less than ideal. The last remaining grating is the $G_2^{(C)}$. So, the combination $G_1^{(B)}$ and $G_2^{(C)}$ is chosen for the experiment at the PHELIX facility.

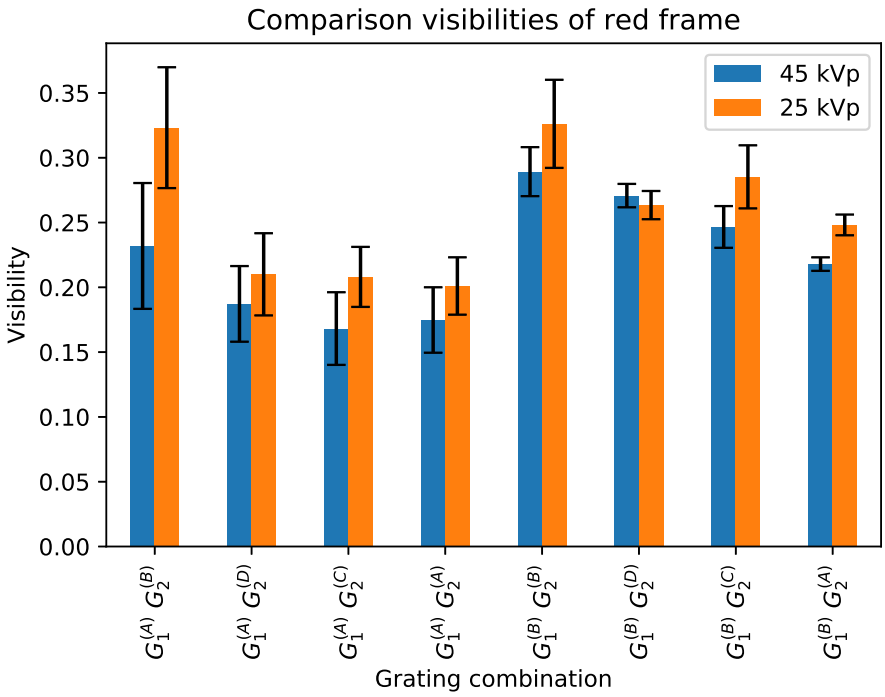

Fig. 4.2: Bar chart of the visibility of the red marked reference frame. The blue bars show the visibility of the moiré pattern with an acceleration voltage of 45 kVp. The orange bars mark the visibility gained with the 25 kVp. The error bars show the error of the visibility.

Looking back, it can be said that the choice was the right one. The cracks, in the grating structure, can be removed almost completely during the reconstruction process (see [Sch21]). The visibility values during the beam time experiment were $\approx 10\%$, low but, as will be shown in section 5.3, sufficient to perform reconstructions. The apparent best grating combination $G_1^{(B)}$, $G_2^{(B)}$ was also used to image objects in the x-ray laboratory of the

Ecap facility and during the beam time. In the x-ray laboratory of the Ecap facility the cloudy appearance did not influence the quality of the recunstructed image. The cloudy appearance could be removed completely during the reconstruction process. This did not work for the images taken at the backlighter source. This is due to the fact, that the position of the focal point of the backlighter source has a shot to shot fluctuation. For further details and explanations see [Sch21].
In Figure 4.2 can be seen, that the visibility tends to be higher for the lower acceleration voltage (orange bars) compared to higher 45 kVp measurement (blue bars). This tendency can be verified for all examined frames, see Figure A.4. The x-ray spectrum with the 25 kVp acceleration voltage has a lower energy spectrum compared to the 45 kVp [DM11]. This lower energy spectrum has a higher photon flux at 12 keV, which is the design energy of the interferometer. This observation indicates that the visibility is probably even higher at the backlighter, where the dominant energy is between 11 keV and 12 keV (see section 3.3). As the tendencies of the visibility is the same for the hight voltage, all following experiments are done with a high acceleration voltage. At higher acceleration voltages a higher power and thus a higher photon flux can be achieved. So, the measurement time can be reduced by at least a factor two at even a higher photon flux.
For similar selection measurements in the future, the process described here could be optimized. The visibility of the area on the moiré map, which is also used for imaging, would be a more appropriate basis for selection. As will be derived in section 4.4, a tilting of the grating G_2, which is placed in the Talbot distance, provides moiré fringes with the highest visibility. So, a moiré period of ≈ 5 pixel per period (ppp) adjusted by tilting the G_2 is an adequate area to compare the gratings adequatly. So, the reconstruction algorithms could be used to determine visibility, which is, in comparison to the manual determination, more percise.

4.2 Curved grating frames

In Figure 4.1 further observation can be made in addition to the change of the moiré pattern. Every single image turns black towards the right side. The measured intensity decreases towards this side. This effect can be explained by shadowing effects from the grating G_2 (see section 3.4). X-ray backlighter and common x-ray sources have a focal spot. They emit the x-ray radiation in a cone beam geometry. So, a flat G_2 grating, as it was used for acquiring the moiré map, does not match the geometry of the x-ray beam. The incident angle of the x-rays is not constant over the whole grating surface. For a round grating with a diameter of 70 mm and a distance to the source of 871 mm, the incident angle would be 90° in the middle and 87.4° on the edge. Due to the 150 µm high grating bars and the period of 6 µm even small deviations from a perpendicular incident angle causes shadowing (see Figure 3.9 (b)). To avoid this, the G_2 grating has to be bend. With this setting the photon flux at the edges of the grating is increased. This increases the area of high visibility (see [Sch16]). In this section flat and curved grating frame are investigated regarding their effect on shadowing. This is done with the chosen grating $G_2^{(C)}$. For this experiment the grating G_1 is removed. The grating G_2 is placed at the optimal of 871 mm in front of the x-ray source. The detector is placed 200mm behind the grating.
The flat grating frame is investigated in two orientations. In one orientation the grating surface faces towards the detector and in the other towards the x-ray tube. This makes it possible to check whether the grating in the flat grating frame is also flat. Figure 4.3 shows this comparison. On the left side two radiographies can be seen. The upper shows the configuration, where the grating faces the detector. The lower shows the x-ray tube facing configuration. The colorbar to the right shows the color code of the intensity. The grating and the relevant area is delimited by the yellow circle. Comparing the inner circle with the color bar, it can be seen tat the intensity values are not uniformly distributed. This is caused by the grating. On the horizontal axis, the intensity is low on the left and right side and increases torwards the middle. This is the shadowing effect (see section 3.4). Along the vertical axis the intensity is almost constant over the entire grating surface. This effect can be explained with the geometry of the grating. The grating bars and the gaps between the grating bars are extended along the vertical axis. So, x-rays with any incident angle can pass the grating, as long as they are parallel to the grating bars. Hence, only the incident angle of the ray perpendicular to the grating bars is essential for the arising shadowing. Comparing the two images with the naked eye, it can be seen that the upper figure has a wider range of high intensity. This is investigated in a more quantitative manner with the line plot on the right side. This line plot shows the mean intensity values of the framed area in the radiographs. The blue markers are the detector facing configuration and the red the x-ray tube facing configuration. The error bars indicate the standard deviation. Both configurations have almost the same maximal intensity. But the

intensity distribution of the detector-facing configuration has a wider area of high intensity. The detector facing configuration meets the cone beam geometry better than the x-ray tube facing configuration. With this result it can be assumed that the grating is not flat. The flat grating frame does not manage to straighten the whole grating.

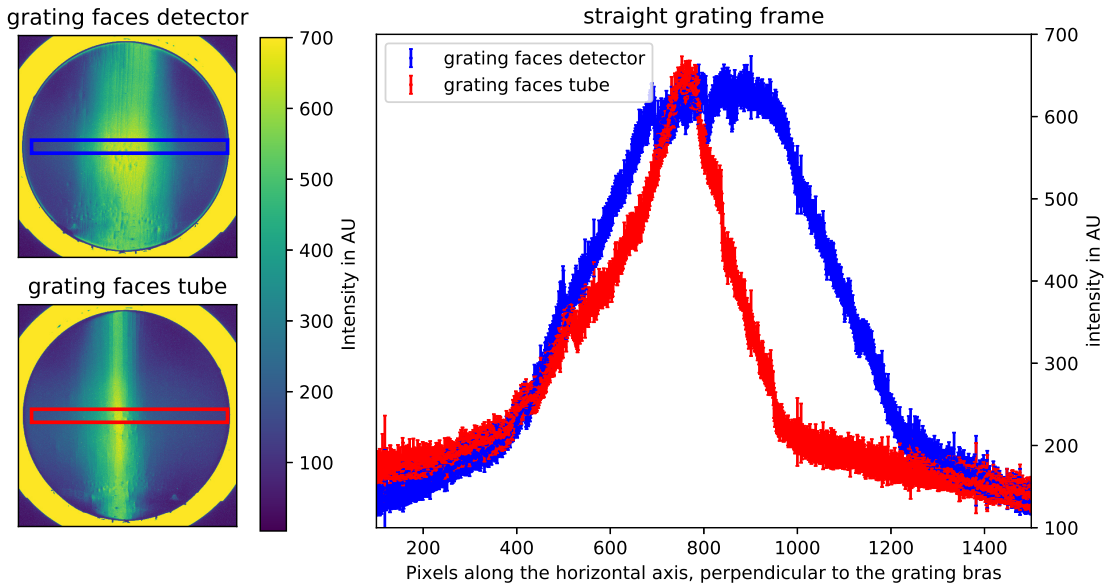

Fig. 4.3: Left side: Radiographs of the grating $G_2^{(C)}$ in a flat grating frame. In the upper figure the grating surface faces the detector, in the lower the x-ray source. The colored frames mark the area used to generate the line plot on the right. This area spans 100 pixels vertically and the whole grating horizontally.
Right side: Mean intensity values of the selected areas. The error bars indicate the standard deviation.

The insights gained will be used for the experiment with the curved grating frame. To increase the intensity and reduce the shading, the already existing curvature of the grating is increased. This should prevent possible damage to the grating. The experiment with the straight grating frame already showed that the grating frame does not influence the shape of the grating sufficiently. The grating frame does not force the grating into a straight shape. Therefore, the clamping surface of the curved grating frame will be increased. For this purpose the recess is reduced from 90 mm to 80 mm. This almost doubles the clamping surface. This may increase the influence on the grating. The shadowing effect only occurs perpendicular to the grating bars. Hence the grating frame must only meet the curvature of the beam perpendicular to the grating bars. The two investigated grating frames have a curvature of 726 and 871 mm. The evaluation is done in the same way as for the straight grating frames. Figure 4.4 shows the results, ordered in a similar way as explained above for Figure 4.3. The left upper image shows the radiograph for the frame with a curvature radius of 726 mm. The lower image for the frame with a radius of 871 mm. The overall appearance of the illumination is the same for both combinations. The whole left side of

the grating is not illuminated well compared to the right side. On the right side an area has formed where the intensity is high. The location of this area is not the same for the two grating frames. For the upper image the area is located in the right upper corner, for the lower image in the center right. Comping these images with the one in Figure 4.3 it can be seen that the dark blue areas become partially light green and yellow. This can be verified with the lineplot on the left side of Figure 4.4. The overall shape of the line plots look the same for both curved grating frame. It is noticeable that there is no longer a prominent maximum in the middle of the grating. The maximum has shifted to the right side and looks like a plateau. On the left half of the grating there is a distinct minimum.

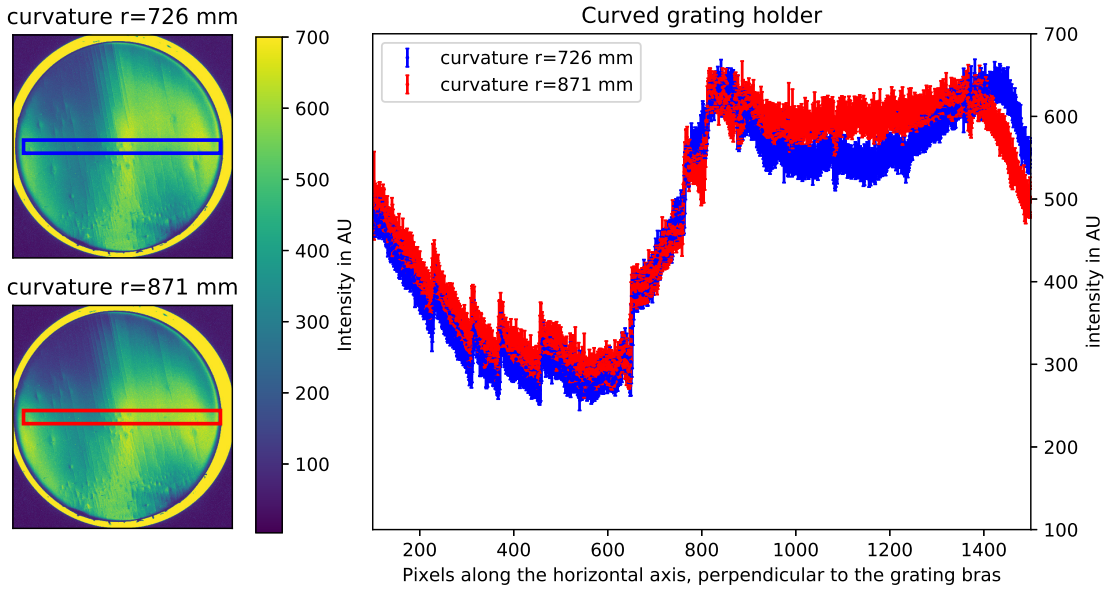

Fig. 4.4: Left side: Radiographs of the grating $G_2^{(C)}$ in the curved grating frame. In the upper image the used grating frame has a radius of 726 mm, in the lower figure 871 mm. The colored frames mark the area used to generate the line plot on the right. This area spans 100 pixels vertically and the whole grating horizontally.
Left side: Mean intensity values along the horizontal axis. The colored boxes in the radiograph mark the plotted RoI. The error bars indicate the standard deviation.

Both curved grating frame increase the mean intensity. But the intensity distribution and thus the curvature of the grating does not follow any obvious rule. Further was observed, that the conductive varnish waver of the grating $G_2^{(C)}$ changed its shape permanently with every clamping trial. This increases the unpredictability of the bending behavior of the grating. Next to the unpredictable bending behavior of the grating, it turned out that the grating frames were not solid enough. While bolting the grating frames together, the aluminum itself starts loose its initial shape. New grating frames are designed to avoid this issue. Due to manufacturing limitations the construction material could no be replaced by a more ductile steel. As the grating mounting socket is able to hold frames of various thicknesses, the thickness of the grating frames was increased by 3 mm (see

Figure 3.5). The bolts, which were initially placed in the corners of the grating frame are placed closer to the grating waver and the number of bolts is doubled. This should lead to a higher and better distributed pressure. The newly designed grating frames weren't manufactured in time to test them before the beam time experiment took place. After the beam time it was not possible to remove the gratings from the used grating frame, as an important comparative measurements still has to be done. So, it was not possible to test the new grating frame within this thesis. For the beam time and further experiments the configuration flat grating frame with the grating surface pointing towards the detector was selected. This choice was made with the focus on the most homogeneous intensity distribution possible.
If similar experiments will be done in the future, the following things should be kept in mind: Reducing the numbers of bending iterations might be beneficial for the grating structure and the predictability of the bending behavior. If gratings are bent, it is conceptional better to bend the grating in such a way, that the grating surface is on the outside of the radius. Therefore, the grating structure gets stretched and not compressed. Maximizing the clamping surface and increasing the stiffness of the grating frames may help to imprint the desired shape onto a grating.

4.3 Comparing reconstruction methods

In this section the performance of two reconstruction methods is compared. To evaluate these methods, the retrieved visibility, the transmission and Dpc images are compared. This is done by comparing the appearance of the images with the naked eye. Followed by a detailed and more quantitative investigation of a selected range of interest (Roi).

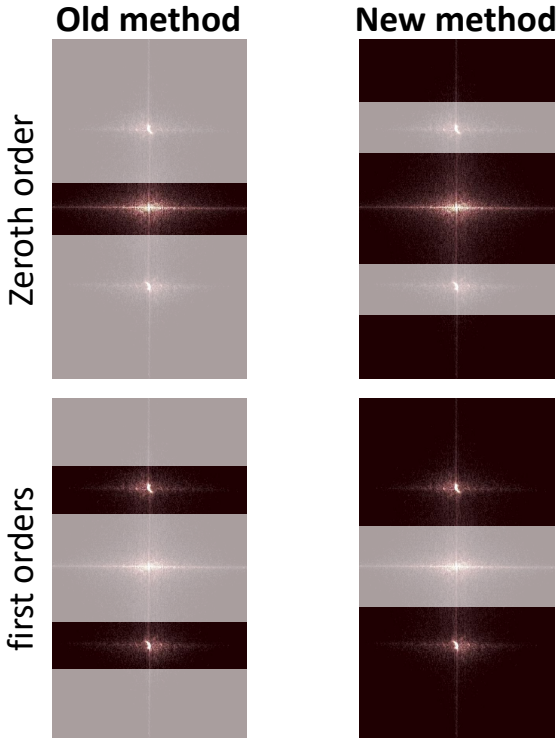

Fig. 4.5: Schematic sketch of the different ways to cut the spectra of the object and reference frames in Fourier space. The left picture shows how Takeda in 1982 suggested the cut (Old method). The right image shows, the method suggested and implemented by Seifert (New method). The grayed out areas of the spectrum are removed. An detailed explanation of the spectra is given in subsection 2.3.3.

To reconstruct the transmission, Dpc and dark-field image, the thereof acquired object and reference frame need to be processed in the Fourier space. This requires isolating specific areas in the Fourier transformed images (see subsection 2.3.3). This isolation is done with masks. Masks are matrices with the pixel dimensions of the image. The values in the mask ranges between zero and one. By multiplying this mask with the image, the pixel values multiplied by zero are set to zero. With specifically designed masks the zeroth and first order peaks are isolated. Two different approaches are available to isolate these required areas. The first approach follows the one published by Takeda in 1982 [TIK82], which in the following is referred to as the old method. The other was invented in 2018 by Seifert [SGL+18], which in the following is referred to as the new method. Figure 4.5 visualizes the areas in frequency space that are selected by the two methods. The left column shows

the approach of the old method, the right column shows the approach of the new method. The first row shows the area, which is selected around the zeroth order peak. The second row shows the same for the first order peaks (see subsection 2.3.3). The old method only selects a small area around the required order. The remaining spectrum is removed. the new method removes the area, which is explicitly not required. If, for example, the zeroth order is required, only an area around the first order peaks is removed. So, the new cut keeps the high frequencies in the spectra.

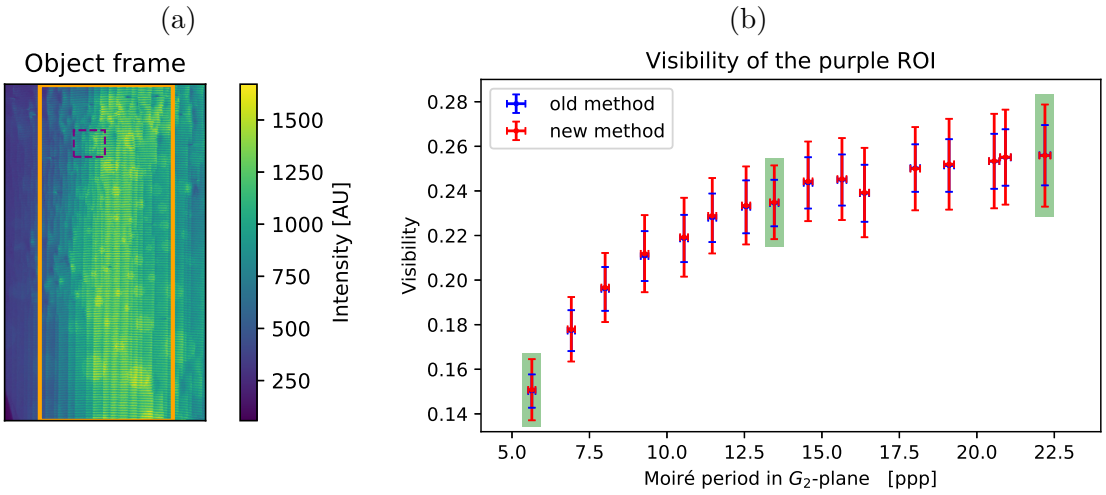

Fig. 4.6: (a) Object measurement of a hole target. The yellow frame marks the area of reconstruction. The purple dashed rectangle marks the RoI which is used for the detailed comparison. (b) Arithmetic mean of the visibility in the in (a) marked purple area, plotted over the moiré period. The error bars indicate the standard deviation of the visibility in the RoI. The green highlighted measurement points are used exemplarily for the further comparisons.

The two methods are compared concerning their performance of reconstructing images, which were acquired at different moiré periods. The performance of the methods is compared by examining the quality of the reconstructed transmission and Dpc images. The transmission image is reconstructed using only the zeroth order. For the Dpc image only the first order is used. By comparing both image modalities, the isolation process of the zeroth and first order can be verified. Therefore a hole target was imaged. The target is made of a polyacrylic mixture and was produced by stereolithography. It measures $40 \times 40\,\mathrm{mm}$ and is 2 mm thick. The through holes in the target have different diameters and rounded edges. A detailed examination and characterization can be found in [Die19]. 16 different moiré periods in the range of 5 to 22 ppp are adjusted. The moiré periods are set by changing the angle α between the gratings while maintaining the optimal distance between the two gratings. For every adjusted moiré pattern a reference and object frame is necessary. The hole target is mounted on a linear stage, so that it can be moved automatically. The acceleration voltage was set to 45 kVp with a power of 4 W in

microfocus mode. For every reference and object measurement 6 frames with an acquisition time of 5 s are taken. Figure 4.6 (a) shows exemplarily one of the 15 object measurements. The moiré stripes are horizontally orientated. The circles in the image are caused by the through-holes of the target. At the left and right side shadowing can be seen (see section 4.2). The yellow rectangle marks the area where the reconstruction is performed. The purple rectangle marks the RoI, which was chosen for the comparison. To assure that only the selection method differs in the reconstruction process, a script is used, that can use both the new and old method. With this script, the visibility, the transmission and the DPC images are reconstructed. In the following the determined visibility of the moiré pattern is compared.

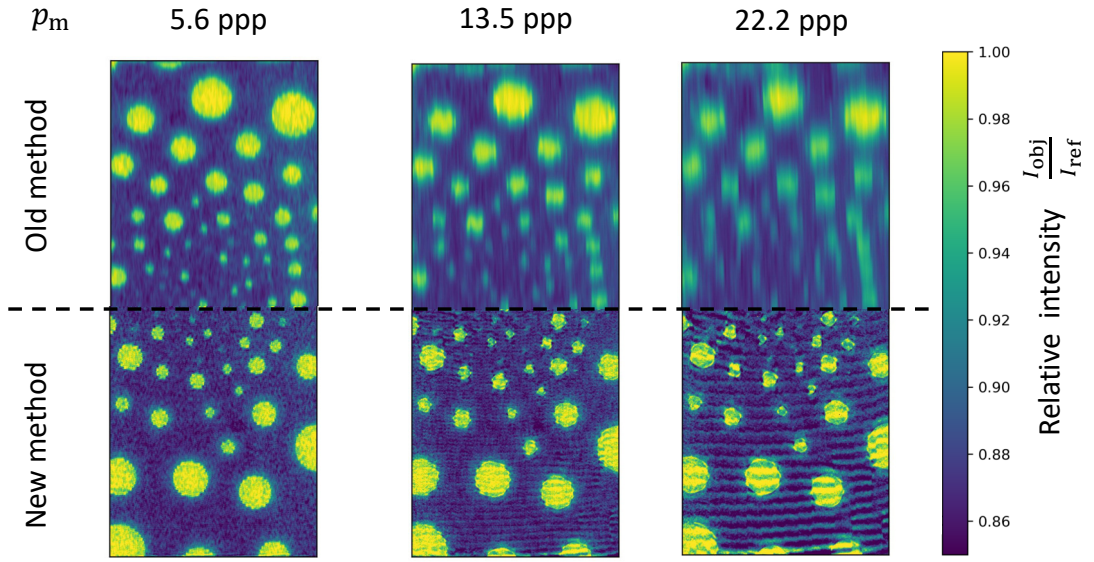

Fig. 4.7: Transmission image of the full reconstruction area. The upper half of the image is reconstructed with the old method, the lower half with the new method. The adjusted moire period increases from left to right.

Figure 4.6 (b) shows the mean visibility of the purple RoI, plotted over the adjusted moiré period. The old method is plotted in blue, the new method in red. The y-error bars represent the standard deviation of the visibility in the purple RoI. The horizontal axis shows the real moiré period $p_m^{G_2}$, back projected into the plane of the G_2 grating. This is calculated according to the intercept theorem by

$$p_m^{G_2} = \frac{p_m^{\mathrm{Det}} \cdot (d(Q, G_1) + d(G_1, G_2))}{d(Q, \mathrm{Det})}, \tag{4.1}$$

with p_m^{Det} being the moiré period in the detector plane, $d(Q, G_2)$ and $d(Q, \mathrm{Det})$ as the distance between the source and the G_2 grating and the source and the detector. The error of the moiré period in the G_2 plane $p_m^{G_2}$ is calculated using Gaussian error propagation. For the determined moiré period p_m^{Det} an error of 0.1 ppp was assumed. For the distances

$d(Q, G_1)$ and $d(G_1, G_2)$ a systematic reading error of 2 mm was assumed. The error of the distance $d(Q, \mathrm{Det})$ was assumed to be 0.3 mm. For the investigated RoI, both methods lead to the same visibility values with a deviation in the promill range. The standard deviation of the visibility is systematically higher for the new method. The sharpness, as will be seen in the comparison of the transmission image, of the images reconstructed with the new algorithm is higher compared to those with the old algorithm. This difference results in a higher standard deviation. The visibility increases with the moiré period, but flattens significantly above a period of 15 ppp. This overall shape is in agreement with the measurements performed in [SGH+17]. Since the visibility does not allow any statement about the image quality, the transmission image is examined in the following. Therefore the three green highlighted measurements in Figure 4.6 (b) are exemplarily compared and investigated.

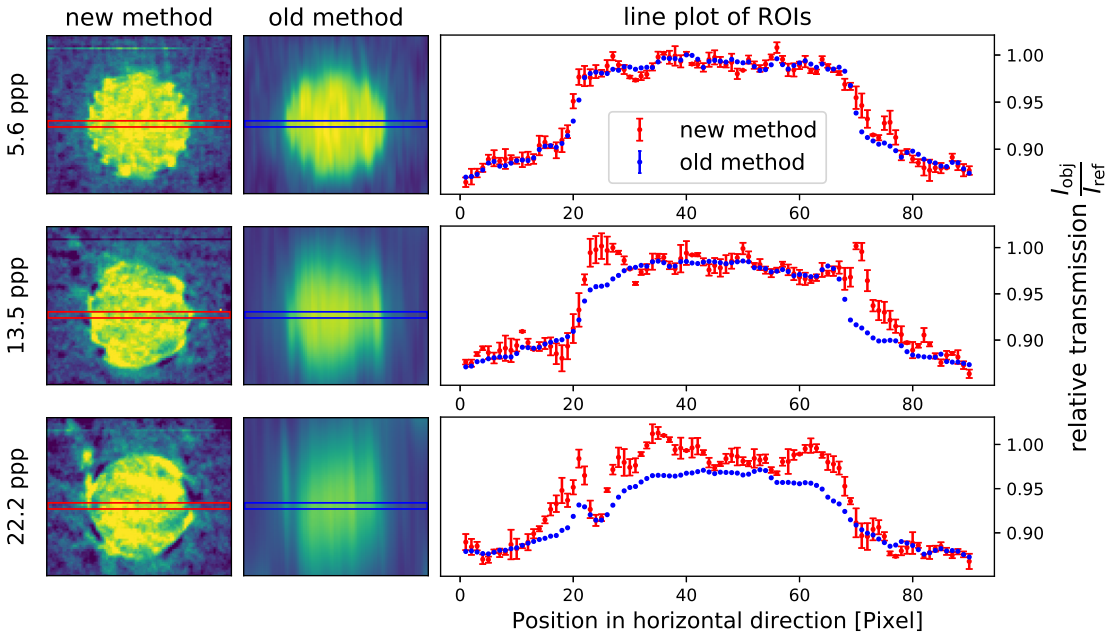

Fig. 4.8: Left: Reconstructed transmission images of purple RoI in Figure 4.6. The left column was reconstructed with the new method, the right column with the old method. The moire period increases from top to bottom. The frames mark the chosen RoI, which is used to generate the line plot on the right side. The RoI spans 3 Pixels vertically and the whole image horizontally.
Right: The line plot shows the arithmetic mean of the RoI. The horizontal axis show the relative transmission $\frac{I_{\mathrm{obj}}}{I_{\mathrm{ref}}}$. The error bars indicate the standard deviation.

The hole target covers the yellow area in Figure 4.6 (a). So, no outer edges will be visible in the reconstructed images. The transmission image should theoretically have the same relative intensity wherever the material of the hole target is. At the positions of the holes the relative intensity should be one. Figure 4.7 shows three transmission images. These images show the yellow RoI in Figure 4.6 and were exemplarily chosen (green frame marks

in (b)). The adjusted moiré period increases from left to right and are stated above the images. Every image is split into an upper and a lower part. The upper half shows the image reconstructed with the old method, the lower half shows the image reconstructed with the new method. Comparing the halves of the left images with the naked eye, the lower image seems to be sharper. By comparing these images with the one in the middle, it can be seen that the image, reconstructed with the old method looses sharpness. The lower half of the image is still sharp, but a periodic structure overlays the whole image. This periodic structure is orientated the same way as the moiré period and has a similar periodicity. By increasing the moiré period to 22.4 ppp these observed effects increase. The upper image seems soft drawn along the vertical axis. Some of the holes are no longer recognizable as such and some smear into each other. The lower image now has a very prominent wave pattern, but the image is still sharp. Comparing all images with the above stated theoretical expectation, the one with the smallest adjusted moiré period is best suited. All holes have a relative transmission of $> 99\,\%$, which is equivalent to full transmission. The material of the hole target shows a uniform absorption of $\approx 13\%$. The periodic structure, which occurs in the transmission image, which was reconstructed with the new method, is an artifact. This artifact can be explained by taking a look into the frequency space (see fig. A.5 on page 86). The chosen size of the mask for isolating the zeroth order is too small. The first order peak is not fully removed.
The large reconstructed area was investigated and compared, now a zoom is made to examine one single hole in a more quantitative manner. Therefore, the purple marked RoI (see Figure 4.6) is investigated. This is done in two steps. First comparing the appearance of the zoomed images. Then comparing the pixel values of a small RoI. This can be seen in Figure 4.8. The figures on the left side, the line plots on the right. The left holes are reconstructed using the new method, the right images with the old method. The period increases from top to bottom. Taking a look at the upper images, it can be seen that even with the smallest adjusted moiré period the right image is clearly fuzzier compared to the left one. This fuzziness leads to a smoothing of the intensity values along the vertical axis. The image on the left is more noisy compared to the right one.
The frame indicates which pixels are used to generate the line plot on the right. In the line plot the horizontal axis indicate the position in the corresponding image on the left. The vertical axis shows the relative transmission. The blue markers are the old method, the red the new one. The relative transmission values are calculated using the arithmetic mean. The errorbars represent the standard deviation. Just as for visibility, the standard deviation is higher with the new method (compare Figure 4.6 (b)). The graphs in the first line match good. The difference between the new and the old method increases for higher adjusted moiré periods. By taking a closer look at the red values in the first line a small oscillation of the values can be seen. Again, this frequency has approximately the same period as the adjusted moiré period.

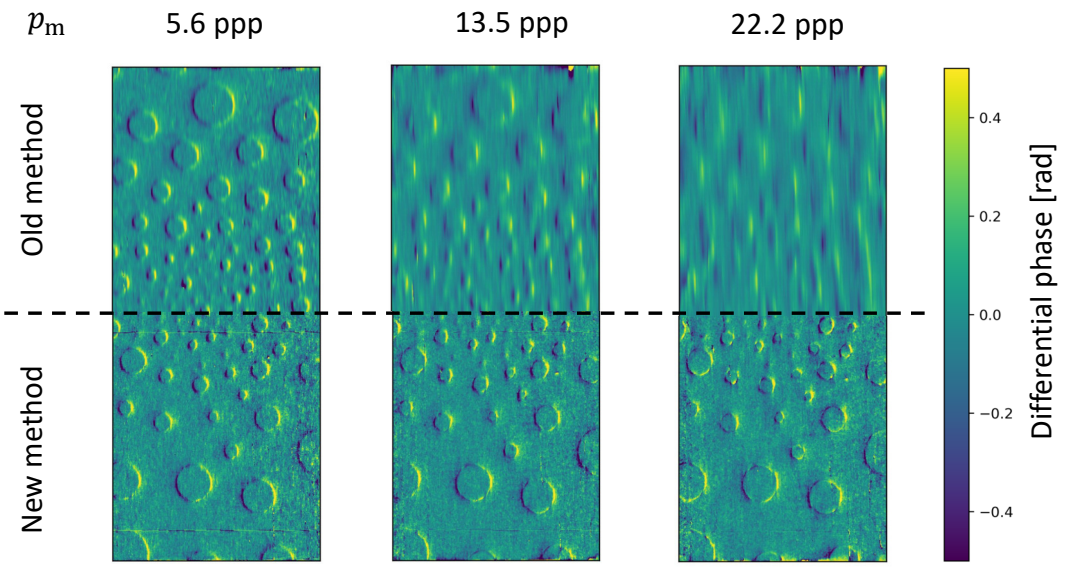

Fig. 4.9: DPC image of the full reconstruction area. The upper half of the image is reconstructed with the old method, the lower half with the new method. The adjusted moire period increases from left to right.

The comparison indicates two tendencies. Smaller moiré periods lead to a better image quality. The given reconstructions allow the assumption that the new method provides clearer images.

With the absorption images, an image has already been isolated that is probably the best. The DPC image is examined below. Since the DPC image is reconstructed only from first order peaks, it can be examined whether the previous result can be confirmed. The DPC measurement is only sensitive to gradients of the electron density perpendicular to the grating bars (see Equation 2.33 and eq. (2.34) on page 23). Assuming a constant electron density for the material, the DPC measurement reacts sensitively to changes in thickness. This means for the hole target, that only the round corners of the holes are visible in the DPC image.

The structure of the two following figures is analogous to the figures of the transmission image comparison. At first a comparison of large field of view images is done, followed by a zoom in to one hole, which is additionally evaluated with a line plot. Figure 4.9 shows the large field of view reconstructed DPC images. The appearance of the images is similar to the transmission images, compare Figure 4.7. The images reconstructed with the old method are not as sharp as the one reconstructed with the new method. The fuzziness of the upper images increases with the period of the adjusted moiré pattern. In the images, reconstructed with the new method, a hardly visible periodic pattern appears for larger moiré periods. As similarly to the transmission image, the reconstructed images with the smalls adjusted moiré period seem to have the best image quality, they are compared with the theoretical expectation. As expected, there is no phase shift apparent, except

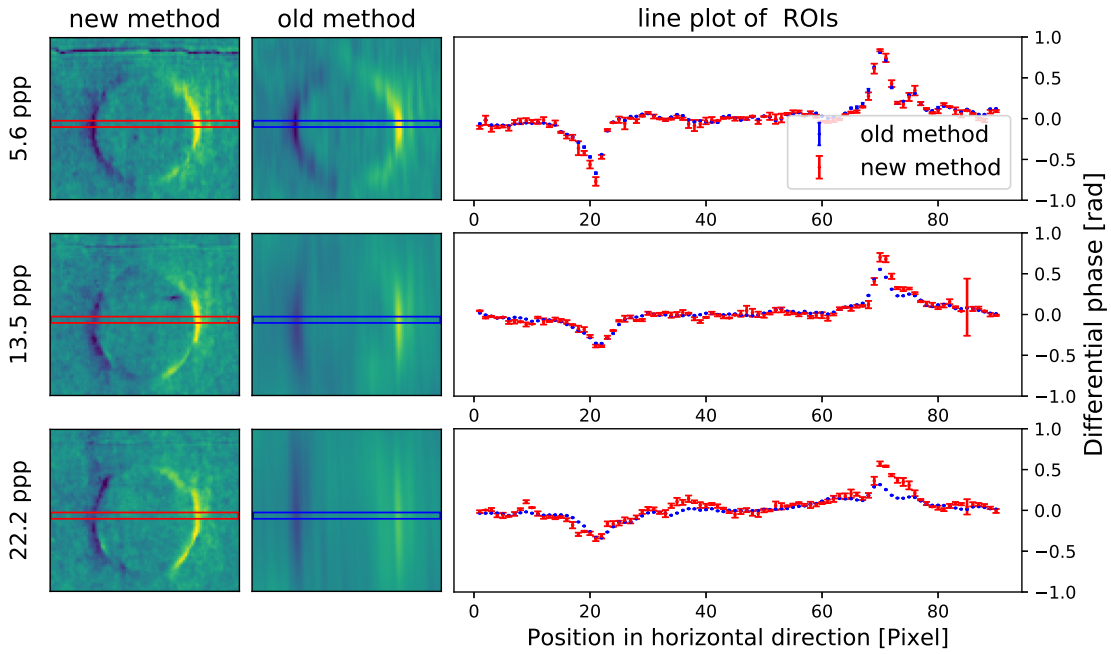

Fig. 4.10: Left: Reconstructed Dpc images of purple Roi. The left column was reconstructed with the new method, the right column with the old method. The moire period increases from top to bottom. The frames mark the chosen Roi, which is used to generate the line plot on the right side. The Roi spans 3 Pixels vertically and the whole image horizontally.
Right: The line plot shows the arithmetic mean of the Roi. The error bars indicate the standard deviation. The large error bar in the middle red line plot comes from a single pixel. At this point the reconstruction did not work.

for the edges of the holes. Apparently there is no difference whether the material has a constant thickness or whether there is no material at all. On one side of the hole a negative Dpc phase shift is measured, on the other a positive phase shift. This means, that the thickness decreases on one side and gets thicker on the other side. This is in agreement with the theoretical expectations of the hole target. The directional sensitivity of the Dpc measurement can be seen in Figure 4.10 on the zoomed images on the left. The black and yellow c-shapes, which form the circle, are most clearly visible at the outer right and left edges. The visibility of the colors decreases towards the top and bottom. The Dpc signal decreases. This can be explained by the orientation of the thickness gradient. The thickness gradients of a through hole with rounded edges point into the center of the hole. As the Dpc measurement is only sensitive perpendicular to the grating bars, only the fraction of the gradient, that is perpendicular to the grating bar can be measured. So, the measured gradient is the strongest in the middle of the circle and decreases to the top and the bottom. The just described black and yellow c-shapes are for the reconstructed images with the old method even for the smallest adjusted moiré period hardly visible. For higher moiré periods the shape is completely lost. With the new reconstruction method,

the circle keeps its shape also for larger adjusted moiré periods. This is investigated in a more quantitative manner with the line plots on the right side of Figure 4.10. The frame indicates which pixels are used to generate the line plot. The graphs match for all adjusted moiré periods good. It is remarkable that the maximum amplitude of the differential phase decreases with increasing moiré period. This phenomenon was also observed and discussed in [SGL+18]. As for the transmission image, a wavy structure is visible in the red graphs too. However, this is not as strong as in the transmission image.
The comparison of the DPC images confirmed the tendencies observed with the transmission image comparison. Smaller moiré periods lead to a better image quality and the new method provides clearer images.
From the comparison it can be concluded, that the new reconstruction method combined with small moiré periods leads for the investigated hole target to the best image quality. For larger moiré periods the images reconstructed with the new method show an artificial periodic structure. The images reconstructed with the old method are generally more fuzzy. For lager moiré periods the initial shape is not identifiable. In this thesis the new method is used for the reconstruction. It is important to keep in mind, that this result can not be extrapolated to a general statement. For other targets the artificial periodic structure may not occur or the old cut is not as fuzzy as it is for this target.
For future measurements with the moiré method the following points should be considered. A moiré period of larger than 5 ppp in the G_2 plane should not be significantly exceeded for both algorithms. This is in agreement with the limit suggested in [SGH+17]. According to [Gal17] the visibility of the moiré pattern decreases in the low range of one digit significantly. So the moiré period should not be chosen much smaller than 5 ppp. If a comparison between the two cut is done for other targets, it is sufficient to do this for one measurement with the optimal moiré period of ≈ 5 ppp.

4.4 Optimizing the visibility of the moiré fringes

According to [Rie17] a high visibility of the moiré fringes increase the image quality. In this section the moiré visibility of the grating combination $G_1^{(B)}$ and $G_2^{(C)}$ is investigated. This is done for a constant moiré period of 6.6 ppp. As the desired period can be acquired with different grating positions, 28 different positions are set.
The investigated moiré period is the same as the one set during the experiment at the PHELIX facility. So, possible systematical effects can be investigated which might also influence the moiré visibility systematically at the PHELIX facility. The experimental parameters as x-ray tube settings, distances and detector parameters are the same as in section 4.3.
There are numerous ways to set the same moiré period using different positions of the linear actors. For this experiment 28 combinations are calculated. The connection between the moiré period p_m and the movement of the grating can be calculated according to Equation 2.22 by

$$p_\mathrm{m} = \frac{p_\mathrm{T} p_\mathrm{G2}}{\sqrt{p_\mathrm{T}^2 + p_\mathrm{G2}^2 - 2p_\mathrm{T} p_\mathrm{G2}\cos(\alpha)}},$$

with p_T as the period of the Talbot pattern, p_G2 as the period of the Grating G_2 and α the relative tilting angle between the grating G_1 and G_2. The Talbot period p_T is adjusted by changing the distance between the two gratings $d(G_1{,}G_2)$. This leads according to the intercept theorem to different magnification and thus to an other period of the Talbot pattern. The Talbot period p_T can be expressed as

$$p_\mathrm{T} = \frac{p_\mathrm{G1}}{2} \cdot \frac{d(Q, G_1) + d(G_1{,}G_2)_\mathrm{opt} + \Delta\mathrm{mov}_\mathrm{horiz}}{d(Q, G_1)}, \tag{4.2}$$

with p_G1 the period of G_1, $d(Q, G_1)$ the distance between the x-ray source and the Grating G_1, $d(G_1{,}G_2)_\mathrm{opt}$ the optimal distance between the two gratings and $\Delta\mathrm{mov}_\mathrm{horiz}$ the movement of the horizontal linear stage. The angle α is changed by tilting the grating G_2. This change can be expressed as

$$\alpha = \arctan\left(\frac{\Delta\mathrm{mov}_\mathrm{vert} + \Delta\mathrm{mov}_\mathrm{offst}}{d(\mathrm{piv}, \mathrm{la})}\right) - \arctan\left(\frac{\Delta\mathrm{mov}_\mathrm{offst}}{d(\mathrm{piv}, \mathrm{la})}\right), \tag{4.3}$$

with $\Delta\mathrm{mov}_\mathrm{vert}$ the movement of the vertical linear stage, $\Delta\mathrm{mov}_\mathrm{offst}$ as a constant offset and $d(\mathrm{piv}, \mathrm{la})$ the distance between the tilting axis of the G_2 platform and the resting point at the linear stage (see Figure 3.4). With the rear therm of the equation, a tilt of the G_2 platform at the optimum point is taken into account. $\Delta\mathrm{mov}_\mathrm{offst}$ corresponds to the required travel distance until the G_2 platform is in horizontal position. By inserting Equation 4.2 and Equation 4.3 into the equation for the moiré period p_m (Equation 2.22), the moiré period can be expressed with movements of the linear stages.

The result of this equation is displayed in Figure 4.11. The horizontal axis shows the relative movement of the horizontal linear stage $\Delta\text{mov}_{\text{horiz}}$, which corresponds to the distance change of the grating. The vertical axis shows the movement of the vertical linear stage $\Delta\text{mov}_{\text{vert}}$. A movement of the vertical linear actor causes a tilting of the grating G_2 and thus the angle changes. The horizontal zero point denotes the distance where the grating is optimally adjusted (see section 4.1). Positive values of $\Delta\text{mov}_{\text{horiz}}$ show an increasing distance between the gratings G_1 and G_2. At the horizontal zero point the angle between the two gratings is zero (see section 4.1). Positive values of $\Delta\text{mov}_{\text{vert}}$ show an movement of the vertical stage upwards. This is in propagation direction of the beam a clockwise tilting of the grating. In this coordinate system the moiré period is shown with a color code. The colorbar is shown on the right side. The measuring points are arranged on the coordinate system depending on the movement. The points are ordered symmetrically around the horizontal and vertical zero axis. They are lined up like a chain on the 6.6 ppp contour line.

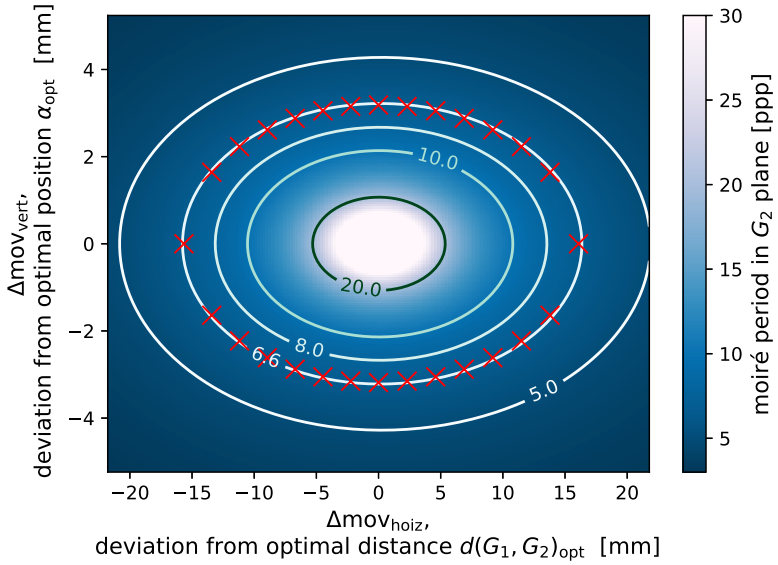

Fig. 4.11: Visualization of the chosen measurement points for the visibility optimization. The plot shows the moiré period p_{m} relative to the movement of the horizontal and vertical linear actor. The red crosses mark the measurement positions. All crosses yield the same moiré period 6.6 ppp, but with different positions of the linear stages.

All measurement points shown in Figure 4.11 are evaluated regarding their visibility. The visibility is evaluated for the RoI, marked yellow in Figure 4.6. The results are shown in Figure 4.12. The horizontal and vertical axis match with the axis in Figure 4.11. The red crosses are replaced with corresponding visibility values, located on the same position in the coordinate system. The color code indicates the mean visibility. To every measurement point the determined moiré period is given nearby. The error to the stated period is 0.1 ppp. This error is calculated using Gaussian error propagation, with the same assumptions

for the uncertainties made in section 4.3. On the left side the visibility is between 0.09 and 0.10. These points have the lowest visibility values in the figure. On the right side the visibility is between 0.11 and 0.12. So, there the visibility is also low, but slightly higher than on the right side. Looking at the range of $\Delta\text{mov}_{\text{horiz}} = [-5\,\text{mm}, 5\,\text{mm}]$, the visibilities tend to be higher. In the upper, middle area, the values reach up to ≈ 0.12. In the lower, middle area the visibility reaches up to ≈ 0.13. These high visibility values are reached when the distance between the grating G_1 and G_2 is slightly larger than the optimal distance. Generally the visibility values decrease with increasing $|\Delta\text{mov}_{\text{horiz}}|$. It is noticeable that the visibility values for $\Delta\text{mov}_{\text{vert}} = 0\,\text{mm}$ deviate from this trend. This can be explained with the cracks in the G_2 grating structure. If the grating G_2 is only shifted, the moiré pattern is parallel to the cracks. Therefore, the moiré pattern overlays with the cracks. The reconstruction algorithm treats these structures as a part of the moiré pattern and the visibility is falsely higher.

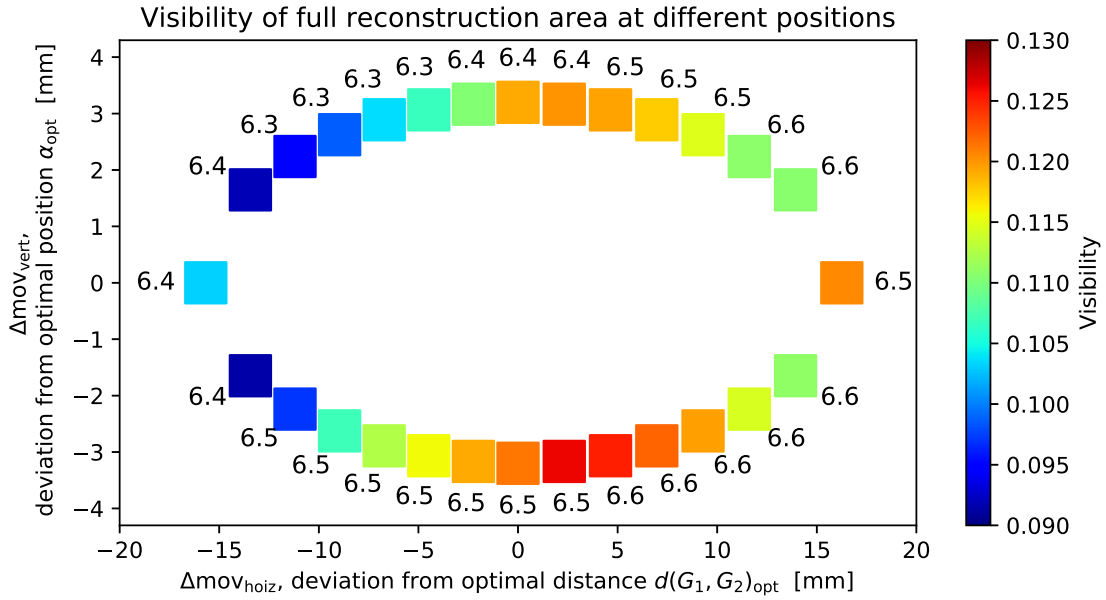

Fig. 4.12: Visualization of the determined visibility values for different grating orientations. The plot shows the moiré visibility relative to the selected positions of the horizontal and vertical linear actor. The numbers show the experimentally determined moiré periods in ppp, back projected in the G_2 plane. The error of the period is calculated to 0.1 ppp.

By taking a look at the determined moiré periods, it can be seen, that the periods differ in some places from the theoretically expected values. In the left upper part of the circle, the theoretically expected value for the moire period is not within the range of the calculated error of 0.1 ppp. One probable explanation for this is that the optimal position $d(G_1, G_2)_{\text{opt}}$ and α_{opt} is not exactly correct. An offset in either the optimal distance and/or the angle result according to Equation 4.2 and Equation 4.3 can cause a shift in the moiré periods. Still, the moiré period is constant constant over a wide range of motion for a negative

values of $\Delta\text{mov}_{\text{vert}}$. Therefore, the difference in the visibility values can not be explained with the differing moiré period. An apparent explanation of the changes in visibility is related to the Talbot carpet. The interferometer is designed in a way, that the Talbot pattern is, for the design energy, the most visible at the optimal distance between the two gratings $d(G_1, G_2)_{\text{Opt}}$ (see section 2.3.1 and section 3.3). By moving away from this optimal distance, the visibility of the Talbot pattern and thus the visibility of the moiré pattern should decrease. Further can be seen that the visibility values are systematically lower for negative values of $\Delta\text{mov}_{\text{horiz}}$, compared to positive values. Two explanations are conceivable. Probably the visibility of the Talbot carpet does not decrease symmetrically around the optimal point $d(G_1, G_2)_{\text{Opt}}$. Alternatively, the magnification of the grating G_1 into G_2 may also play a role. For negative values of $\Delta\text{mov}_{\text{horiz}}$ the period of the Talbot pattern is smaller than the period of the G_2. For positive values of $\Delta\text{mov}_{\text{horiz}}$, the period is larger. This might influence the visibility. The difference between the negative and positive tilt cannot be explained this way. For both positions the distance between the grating G_1 and G_2 is identical. A possible explanation for this observation would be that the G_2 grating has slightly varying parameters over the area. These variations can arise due to the fabrication process. By tilting the grating, different areas of the G_2 grating are investigated. Therefore, a possible explanation is that some areas of the G_2 grating fit the G_1 better in some places than in others.
It can be concluded, that with the investigated setup the highest visibilities can be achieved by tilting the grating in the negative direction and shifting the grating to slight positive values of $\Delta\text{mov}_{\text{horiz}}$. For the PHELIX experiment can be concluded, that tilting the grating in negative direction is preferable compared to a positive tilt.

4.5 Area of reconstruction and the impact on the reconstructed images

Grating based phase contrast imaging can be only done where the grating structures of G_1 and G_2 overlap. The portable interferometer has a sensitive area of $\approx 25\text{cm}^2$. Some objects are small and do not cover the whole sensitive area. In this case the reconstruction area can be chosen freely. The reconstruction area can be chosen narrow around the object, loosely fitting or spanning the whole sensitive area. In this section it is investigated whether the mere choice of the reconstruction area influences the reconstructed image.

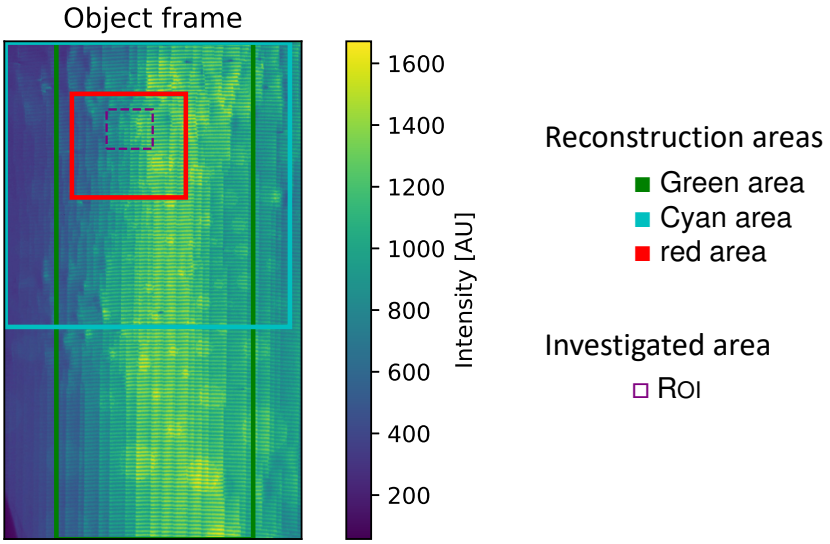

Fig. 4.13: Object frame of the hole target with a visualization of the three different reconstruction areas. The areas are marked exemplarily in an object frame. The purple framed area is the RoI, which is used to compare the reconstructed images.

For this investigation three reconstruction areas are chosen. They differ in shape and size. These three areas are reconstructed and compared in a small RoI. This RoI lies in each of the reconstruction areas. This evaluation is done for the 28 measurement points shown in Figure 4.11. The three used reconstruction areas and the RoI are shown in Figure 4.13. The green, cyan and red frames enclose the reconstruction areas. The purple frame encloses the RoI.

In this RoI the mean visibility, the transmission image and the DPC image is compared. At first the mean visibility values are compared. The results are shown in Figure 4.14. Each box indicates one measurement. The measurements is similarly performed as the ones used in section 4.4. The horizontal axis shows the relative movement of the horizontal linear stage $\Delta\text{mov}_{\text{horiz}}$. The vertical axis shows the movement of the vertical linear stage $\Delta\text{mov}_{\text{vert}}$. For every measurement point three visibility values are determined resulting from the different reconstruction areas. These values are printed onto each other. The

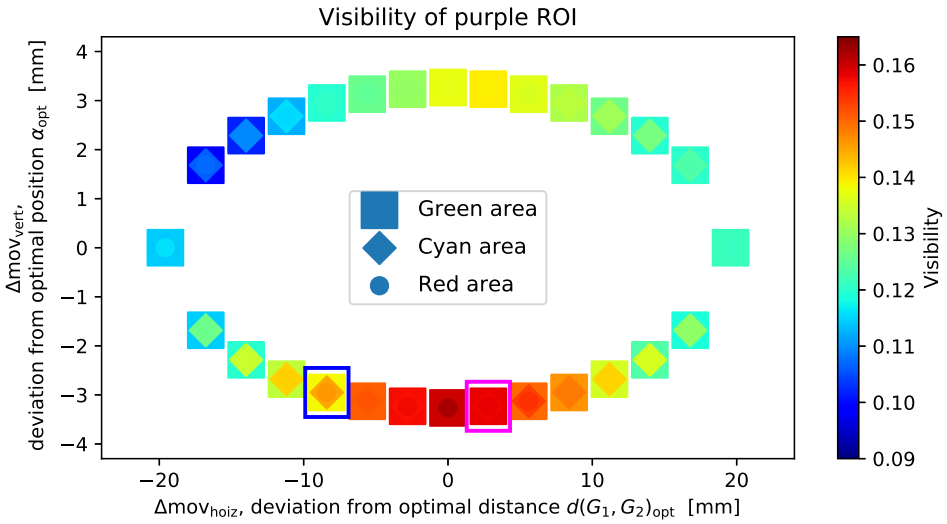

Fig. 4.14: Visualization of the determined visibility values for different orientations of the grating and different reconstruction areas. The figure shows the moiré visibility relative to the selected positions of the horizontal and vertical linear actor. The results of the different reconstruction areas are printed into each other. The two framed measuring points are examined exemplarily.

square marker corresponds to the green reconstruction area shown in Figure 4.13. The diamond shaped marker corresponds to the cyan reconstruction area and the round marker to the red reconstruction area. The code indicates the mean visibility. Dark red refers to a visibility of 0.16, dark blue to a visibility of 0.09 . Only the different visibility values within one measuring point is compared. It can be seen that ten measurement points don't show any or hardly any difference in the determined visibility. The remaining fourteen measurements show a difference in the visibility. This difference is for some points stronger than for others. The most and largest differences can be seen between the visibilities of the green area, compared to the cyan area. A difference between the cyan and the read area appears only a few times. A difference in the visibility between all three areas is hardly observable. It is remarkable that the differences almost exclusively occur outside the optimal distance $d(G_1, G_2)_{\text{opt}}$. For negative values of $\Delta\text{mov}_{\text{vert}}$, the visibility values differ more and often, compared to positive values of $\Delta\text{mov}_{\text{vert}}$. The visibility values already indicate, that the selection of the reconstruction area might effect the reconstructed images. Hence, two measurement points are selected for further investigations. These points are selected with respect to the deviation in the visibility. The first point does not show a significant difference of the visibility within the investigated RoI. The second point shows a difference. In Figure 4.14 the first point is pink framed and the second is blue framed. For these points the visibility values are stated in appendix A on page 89 in the appendix. It is remarkable that the color code is very sensitive to small deviation. Even deviations in the sub per mille are visible.

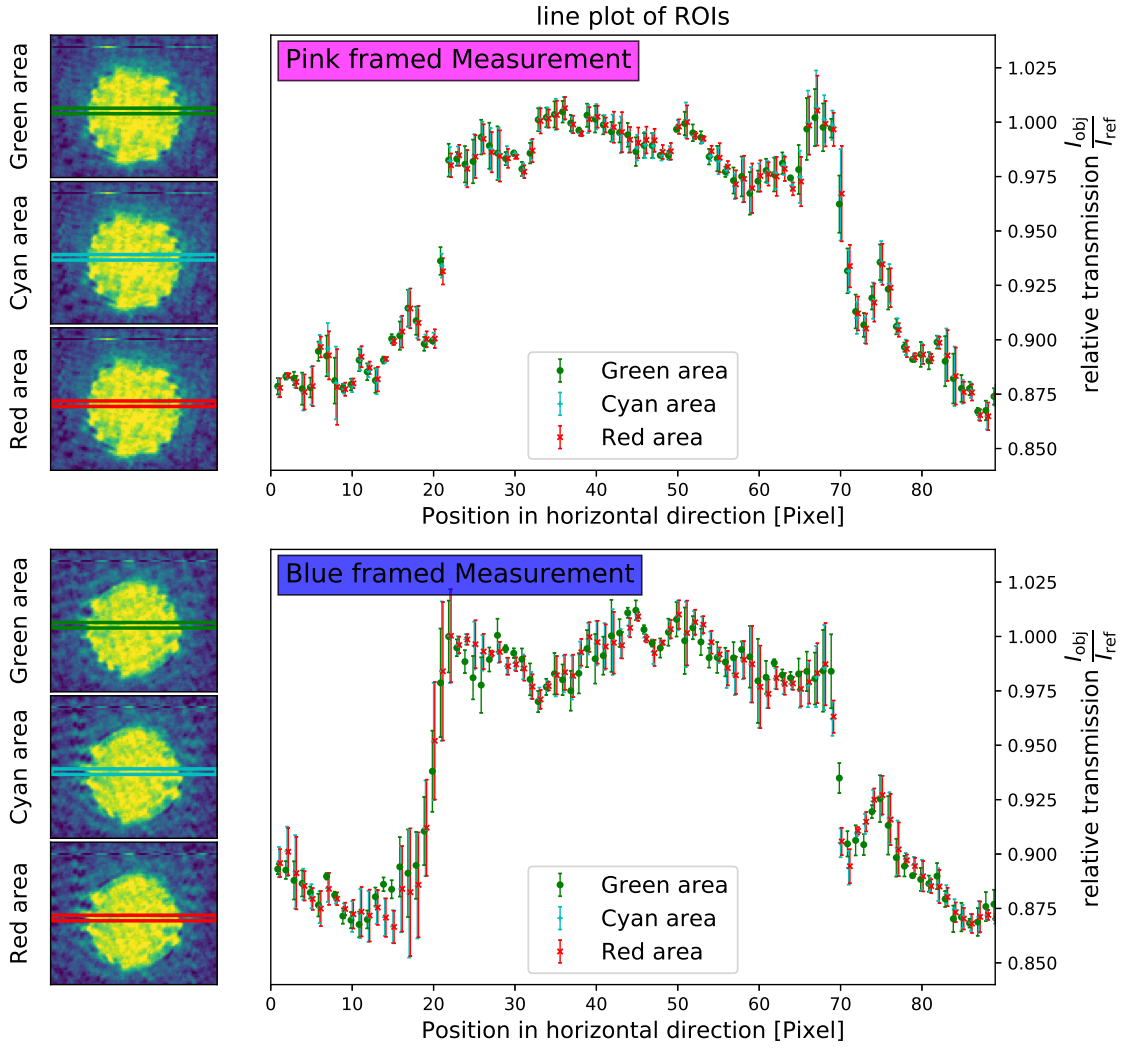

Fig. 4.15: The upper half of the figure shows the evaluation of the pink marked ROI in Figure 4.14, the lower the blue marked.
Left: Reconstructed transmission images of purple ROI. The images are generated from the same measurements but with different reconstruction areas, see Figure 4.13. The frames mark the chosen ROI, which is used to generate the line plot on the right side. The ROI spans 3 Pixels vertically and the whole image horizontally.
Right: The line plot shows the arithmetic mean of the ROI. The error bars indicate the standard deviation. A slight offset is added to the x-values for a better comparability.

In the next step, the transmission and DPC images are compared. This is done for the two selected measurement points. The comparison is done in two steps. At first the mere appearance of the reconstructed images are compared. Then pixel values of a small subarea are compared. This is done with a line plot. This comparison is combined for transmission image in Figure 4.15. The upper half of the figure shows the pink marked measurement point, the lower half the blue measurement point. At first the pink framed measurement point is investigated. The first image on the left side shows the reconstruction of the green

area. The second shows the cyan and third image shows the red area. Comparing the three transmission images with the naked eye no difference can be seen. So, a more precise comparison is done. The line plot on the right shows the mean values of the framed area in the images on the left. The errorbars represent the standard deviation. The horizontal axis of the line plot indicates the position in the corresponding image on the left. The vertical axis shows the relative transmission. The colors of the markers match with the color of the frames on the left. The three relative transmission values match within tiny fluctuations of $\approx 0.005\,\%$ well. The standard deviation is also almost the same. So, no differences can be observed between the three relative transmission values. This corresponds to the circumstance, that the visibility values are also the same at this point.
Moving on to the lower half of Figure 4.15, the blue framed measurement. Again, the three transmission images on the left side look the same. By taking a look at the line plot on the right side a deviation of the relative transmission can be seen. While the relative transmission values and the standard deviation of the cyan and red area are almost identical, the transmission values of the green reconstruction area differ from the two other values at two ranges. The deviations are located on the left side just before the relative transmission increases (pixels 10 to 18) and on the right side in the range of decreasing relative intensity (pixels 60 to 75). The differences between the relative transmission values are in the order of $\approx 0.03\,\%$. The hole target decreases the relative transmission of $\approx 0.125\,\%$. Comparing this value with the difference of $\approx 0.03\,\%$, the deviation is small.
The same comparison is done for the Dpc images. Figure 4.16 shows the same evaluation of the Dpc images, as already explained for the transmission image in Figure 4.15. At first the pink frame measurement is compared (upper half of the figure). The three Dpc images on the left side look the same. The line plots of the differential phase on the right side also match. The difference between differential phase signal of the cyan and red area fluctuates by $\approx 0.015\,\mathrm{rad}$. The differential phase signal of the green area fluctuates relative to the cyan and red area on average by about $\approx 0.025\,\mathrm{rad}$. At the positions of the peaks, the fluctuation increases up to $\approx 0.1\,\mathrm{rad}$. By taking a look at the figure, the deviation is hardy noticeable. For all three reconstruction areas the calculated standard deviation is within a fluctuation of $\approx 0.005\,\mathrm{rad}$ almost the same. So, no significant differences between the three differential phase signals can be seen.
Now the blue framed measurement is compared. The three Dpc images on the left side look the same. Evaluating these images in the framed area with the line plot on the right side, differences in the differential phases can be seen. While the differential phase of the cyan and red reconstruction area is within a deviation of $\approx 0.1\,\mathrm{rad}$ almost the same, the differential phase of the green area differs from the two. This deviation is significantly visible in the two peaks. In the first peak the lowest differential phase signal of the green area is $-0.51\,\mathrm{rad}$ and for the two other areas $-0.31\,\mathrm{rad}$. The amplitudes differ by $0.2\,\mathrm{rad}$. In the second peak the highest differential phase signal of the green area is $0.94\,\mathrm{rad}$ and

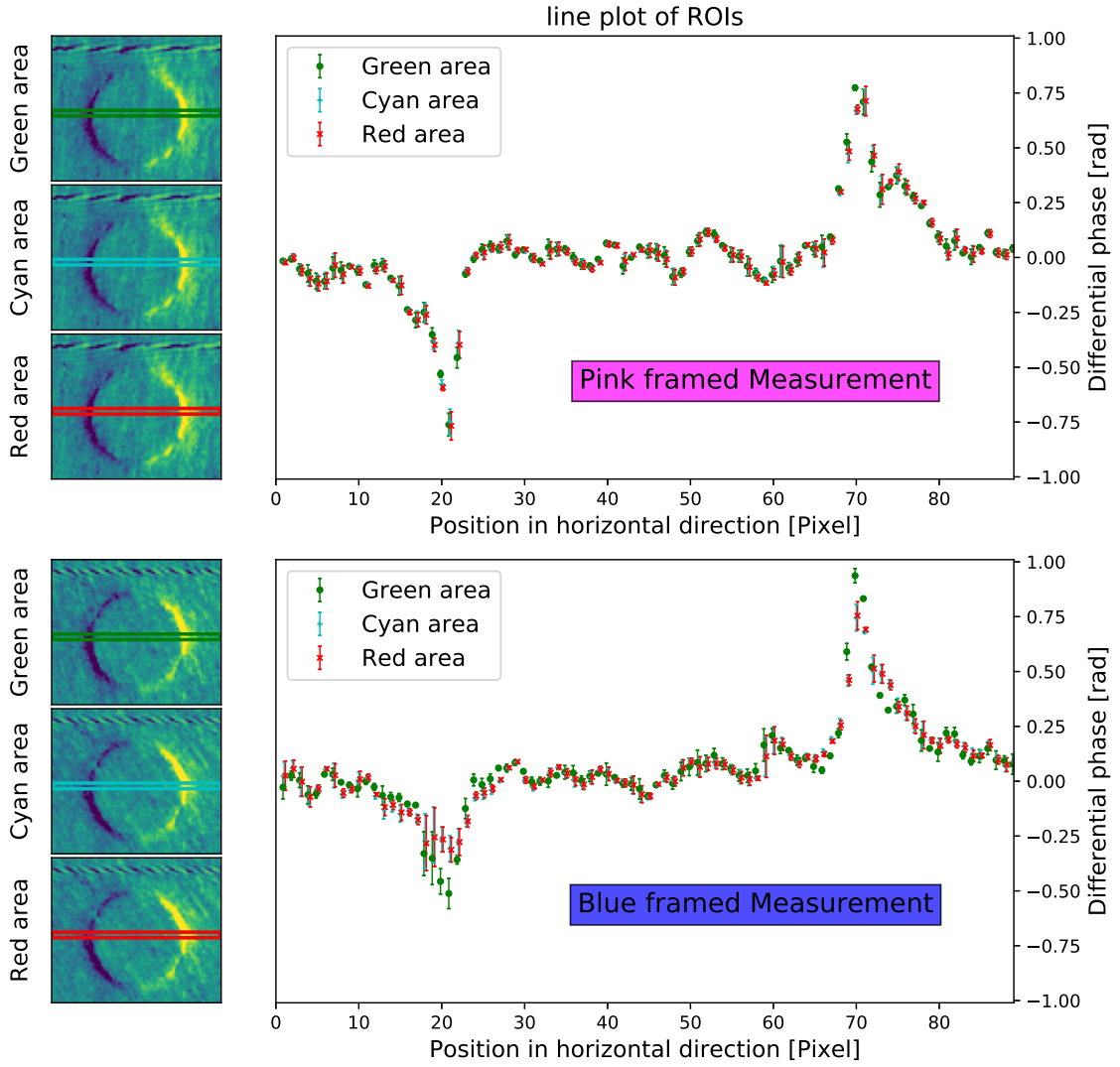

Fig. 4.16: The upper half of the figure shows the evaluation of the pink marked ROI in Figure 4.14, the lower the blue marked.
Left: Reconstructed DPC images of purple ROI. The images are generated from the same measurements but with different reconstruction areas, see Figure 4.13. The frames mark the chosen ROI, which is used to generate the line plot on the right side. The ROI spans 3 Pixels vertically and the whole image horizontally.
Right: The line plot shows the arithmetic mean of the ROI. The error bars indicate the standard deviation. A slight offset is added to the x-values for a better comparability.

for the two other areas 0.78 rad. Here, the amplitudes differ by 0.16 rad. This difference is visible in the numbers and is also significantly visible in the line plot of the differential phase. Outside of the peaks the deviation between the green and the two other reconstruction areas is ≈ 0.05 rad. Still, for all three reconstruction areas, the standard deviations is within a deviation of ≈ 0.01 rad the same.

By taking a look at the line plots of the blue and pink framed measurements, it can be seen, that the line plots differ in their appearance. This difference is significantly larger compared to the differences that result from the choice of the reconstruction Roi. The systematic investigation of this effect is in not done in this thesis, as this would be beyond the scope of this thesis.
The comparison of the visibility, the transmission and Dpc image shows, that the reconstruction area influences the reconstructed images. This statement was verified by investigating further measurement points. Hence, the tendency can possibly be expended to a more general statement. A difference in the Dpc and transmission image is noticeable in the measurement points, where the visibility shows a difference. For all measurements investigated here, the overall appearance of the reconstructed images is not influenced. So, if the reconstruction images are only required for qualitative statements, the effect is negligible small. The observed difference becomes more relevant when quantitative statements are made. This is of special interest where e.g. unknown plasma density distributions in shocked matter is investigated with GbPci.

5 Application at the beam time experiment

In the previous two chapters, a portable interferometer was designed and characterized. This was all done with respect to gain the best possible starting condition for the beam time experiment. In this chapter, it is evaluated whether the assumption made for conceptualizing the interferometer improve the performance. The evaluation of the mechanical characteristics of the portable interferometer is conducted in section 5.1. In section 5.2, shadowing and visibility maps of a laboratory measurement are compared with a measurement from the PHELIX beam time. Finally reconstructed images of backlighter measurements are presented and analyzed in section 5.3.

5.1 Mechanical reliability of the portable setup

During the beam time experiment, the grating combinations $G_1^{(B)}$, $G_2^{(B)}$ and $G_1^{(B)}$, $G_2^{(C)}$ were used. These gratings had to be exchanged during the beam time. Transporting the interferometer and changing the gratings can cause misalignment. To reduce the magnitude of a possible misalignment, a transportation box was specifically made for this purpose. This box is built from wood and lined with polystyrene to damp vibrations. Changing the gratings without great effort is only possible with an mechanically robust, precise and sturdy interferometer. The alignment of every installed grating combination has to be verified at the PHELIX facility. For the first grating combination, the fast alignment method, proposed in [SLA+19], was used. The alignment of the second grating set is evaluated, similar to the fast alignment method, by comparing reference frames. The measurements at the PHELIX facility allows to evaluate the mechanical design of the interferometer.
The principle of the fast alignment method is as follows. At first, a moiré map is prepared. Then, the already aligned interferometer is transported. Due to the transportation, the interferometer might detune slightly. At the destination a reference frame is acquired. By comparing this reference image with the moiré map, the magnitude of misalignment can be determined. By knowing this, the moiré pattern can be adjusted within one step to the desired pattern.
In the x-ray laboratory of the ECAP facility, the grating combination $G_1^{(B)}$, $G_2^{(B)}$ is adjusted to the optimal positions $d(G_1, G_2)_{\text{opt}}$ and α_{opt}. These grating positions result in a moiré pattern with the largest possible period (see section 4.1). With the first backlighter shots at the PHELIX facility, reference frames are acquired. These images can be used for checking the alignment of the interferometer. The reference frame and the moiré map of the grating combination is shown in Figure 5.1. Since a comparison with the first picture is hardly possible, the picture of the second shot is shown in the figure. Between the first and the second shot, the grating G_2 was moved by $+0.5\,\text{mm}$. The moiré map covers

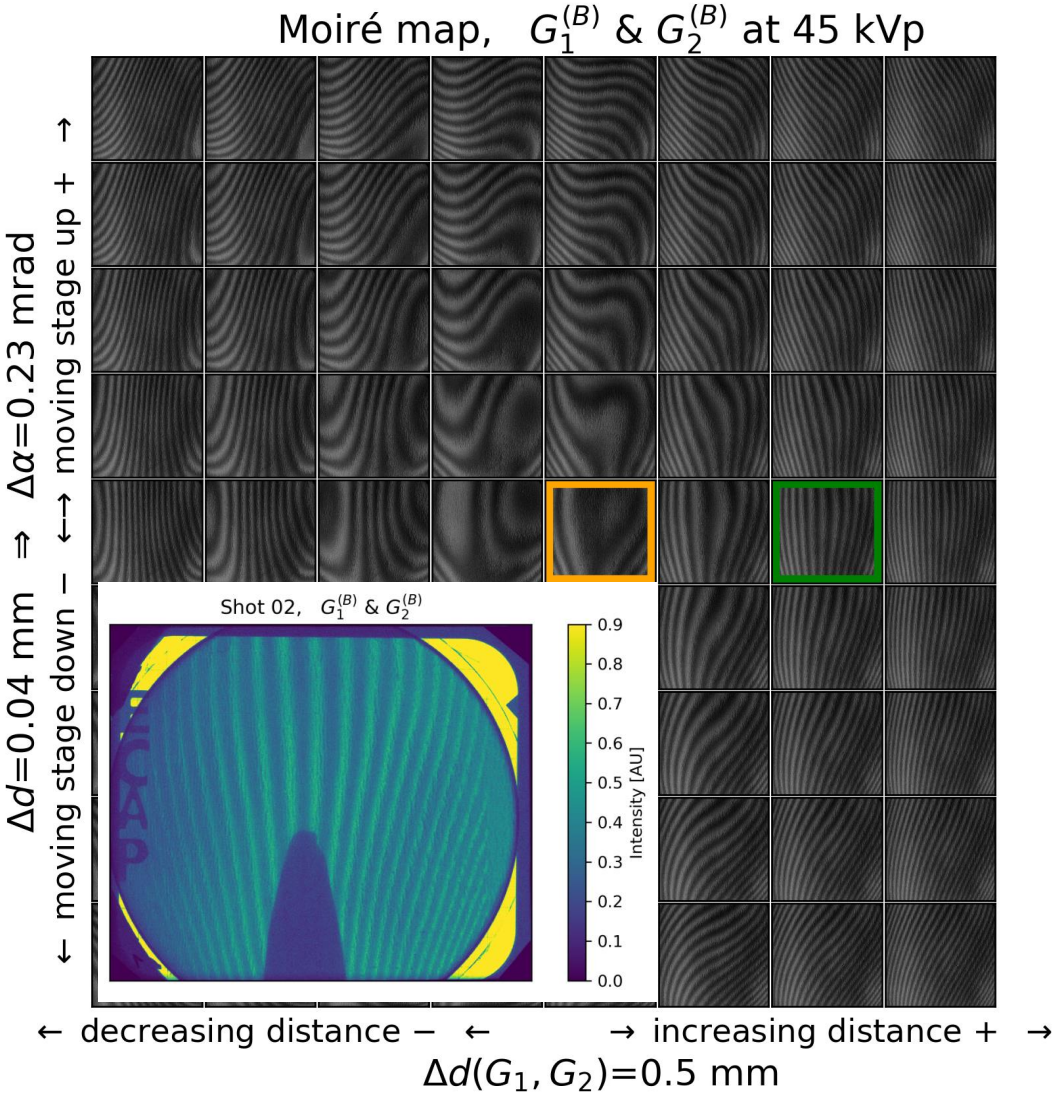

Fig. 5.1: Background: Moiré map of the grating combination $G_1^{(B)}$, $G_2^{(B)}$. The horizontal axis shows the change of distance between G_1 and G_2. The grating G_2 is shifted by 0.5 mm between each horizontal image. The vertical axis shows the relative angle α between the grating bars of G_1 and G_2. G_2 was tilted by 0.23 mrad between every vertical image. The orange frame marks adjusted position at the x-ray laboratory of the ECAP facility, The green frames marks the estimated position of the interferometer during the second shot at the PHELIX facility. Own figure, adapted from [SLA+19].
Foreground: Scan of the IP of the second shot at the PHELIX facility. The tip in the middle of the image is a needle which is used for finding the correct positions of the targets.

a deviation in the grating distance $d(G_1, G_2)$ of 3.5 mm on the horizontal axis and a change in the grating angle α of 2.06 mrad on the vertical axis. The steps between every horizontal image is 0.5 mm and between every vertical image 0.27 mrad. In the ECAP facility, the interferometer was adjusted to the orange framed image, the optimal position.

By comparing the image of the second shot with the images of the moiré map, it can be seen that the green framed image fits best. According to the step width between the images on the moiré map, the deviation between the green and the orange framed image is horizontally +1 mm and vertically 0 mrad. As between the first and second shot the horizontal linear stage was moved horizontally by +0.5 mm, the effective misalignment is ≈ 0.5 mm horizontally. A deviation in the vertical position is not noticeable. The deviation of the grating position is only that small due to the mechanical design and a safe transportation of the interferometer.

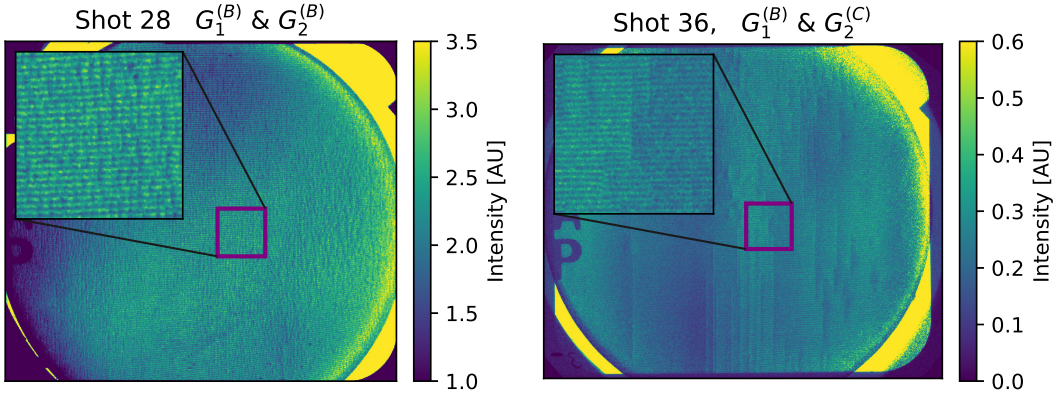

Fig. 5.2: Comparison of the adjusted moiré pattern with two different grating combinations. The image on the left side shows the finally adjusted moiré pattern of the grating combination $G_1^{(B)}$, $G_2^{(B)}$. The image on the right side shows the moiré pattern with the grating combination $G_1^{(B)}$, $G_2^{(C)}$ at the PHELIX facility.
The purple framed area is magnified to make the moiré pattern visible. Note: A pattern with a large period (10 to 30 fringes over the whole area) is probably visible. This is an additional moiré pattern which occurs due to the discrete pixels of the monitor or printer and the adjusted moiré pattern.

The here described procedure of changing the gratings and evaluating the alignment is based on the assumption that the portable interferometer is built in such a way that removing and mounting gratings does not change the relative positions between the gratings. All relevant grating combinations have to be aligned in the x-ray laboratory of the ECAP facility. The thereby determined optimal positions $d(G_1, G_2)_{\mathrm{opt}}$ and α_{opt} keep their validity even when the gratings are removed from the interferometer. For the transport the gratings can be transported separately. With the saved values of the relative positions of the gratings, the interferometer can be aligned instantly at any place. This allows to change the grating combinations during a beam time experiment. During the PHELIX beam time, it was possible to change the gratings and to adjust the desired moiré pattern without aquiring one single shot for the alignment process.
During the beam time, the grating combination was changed from $G_1^{(B)}$, $G_2^{(B)}$ to $G_1^{(B)}$, $G_2^{(C)}$. After mounting the new grating combination, both linear stages were referenced.

After that, the grating G_2 was moved to the optimal position. Now the gratings should be perfectly aligned. At this place, the alignment of the gratings could have been checked using the fast alignment method. But this step was skipped. The grating was instantly positioned in a way that the first shot with the new gratings can be used as a reference image for moiré imaging. Hence, the vertical stage was moved by $\Delta\text{mov}_{\text{vert}} = -3.2\,\text{mm}$ to get a moiré period of $\approx 7\,\text{ppp}$. As the negative tilt of the vertical linear stage exceeds the covered deviation range in the moiré map ($\Delta\text{mov}_{\text{vert}}^{\text{max}} = -0.16\,\text{mm}$), the alignment can not be verified using the moiré map. In this case, the reliability can be verified by comparing the moiré period and its orientation of the two used grating combinations. This works because the gratings $G_2^{(B)}$ and $G_2^{(C)}$ only differ in the used waver material. The grating parameters such as the period, the duty cycle and the grating height are identical (see table A.3 on page 88). Further the same relative values for $\Delta\text{mov}_{\text{vert}}$ and $\Delta\text{mov}_{\text{horiz}}$ were set. Thus, the resulting moiré pattern had to be identical if the setup is rigide. The comparison is done in Figure 5.2. The left image shows a reference image of the grating combination $G_1^{(B)}$, $G_2^{(B)}$. The right image shows a reference image of the grating combination $G_1^{(B)}$, $G_2^{(C)}$. The moiré pattern is too small to be visible in the large image. So the purple framed area is magnified. In this zoomed detail, the moiré pattern and its orientation can be compared. Both patterns are slightly tilted clockwise. A difference in the angle is not determinable with the naked eye. Even the pixel pitch of the tilt is the same for both images. The moiré period of the left image is determined to $7.0 \pm 0.1\,\text{ppp}$ and the period of the right image to $6.9 \pm 0.1\,\text{ppp}$. So, the moiré period is the same within the error.

Thus, it can be concluded that the starting point from which the grating was tilted corresponds to the optimal point. This showed that the optimal point can be stored reliably. The point does not lose its validity even after transport and grating change. The successful adjustment of the desired moiré pattern after the gratings were changed showed that the interferometer was built within the required mechanical precession and sturdiness. The grating frames in combination with the grating mounting bracket allowed a precise positioning with repeating accuracy. The chosen linear stages with its design resolution of $5\,\mu\text{m}$ allow a reliable positioning of the gratings on the scale of µm.

5.2 Shadowing, noise and the visibility

During the characterization process various grating frames with different curvatures had been investigated to decrease the shadowing of the grating $G_2^{(c)}$ (see section 4.2). During the beam time, the shadowing of this differs from the shadowing observed in the x-ray laboratories of the ECAP facility. In this section, possible effects of these differences are examined.

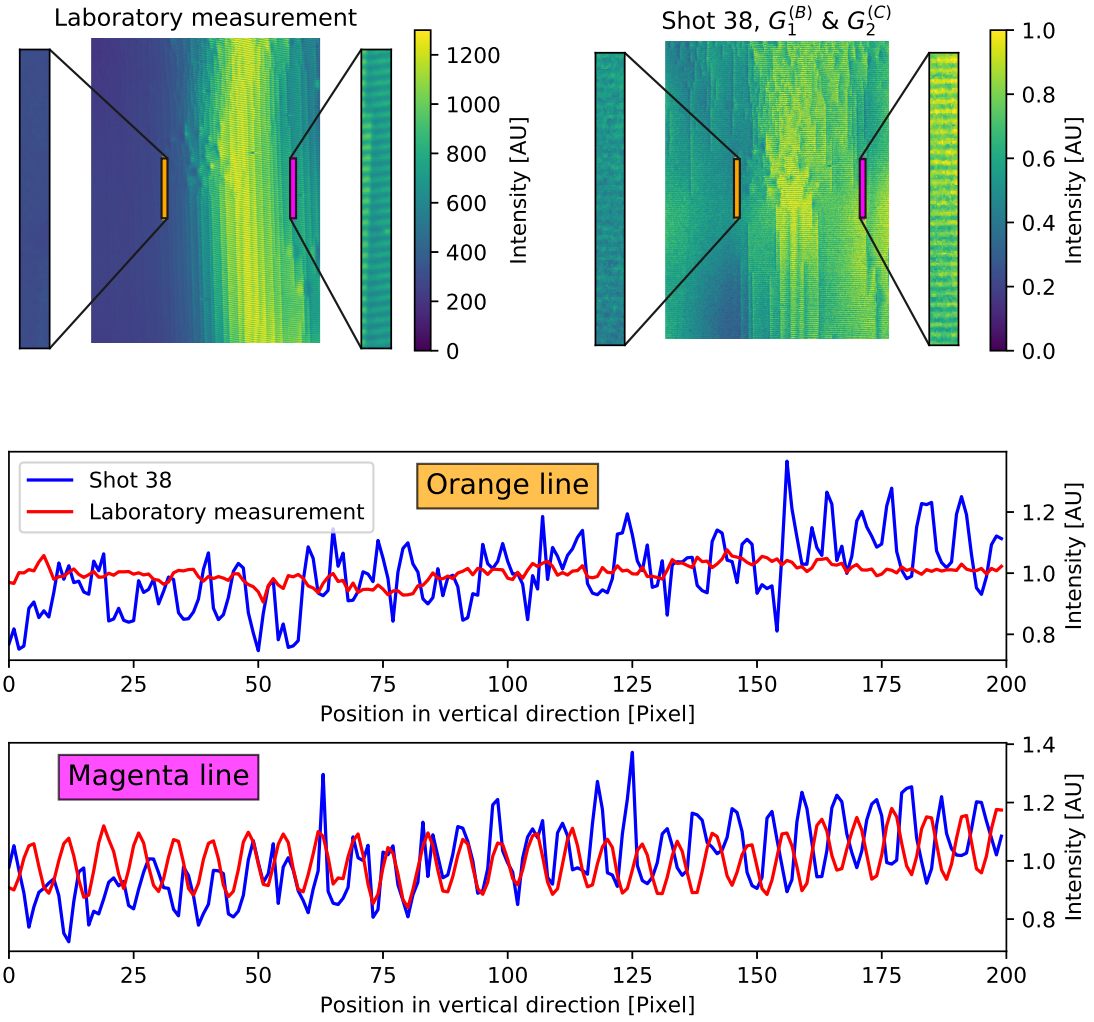

Fig. 5.3: Top: The image on the left shows the reference frame, acquired in the x-ray laboratory of the ECAP facility. The image on the right side shows shot 38 of the PHELIX beam time. The orange and magenta lines indicate the positions which pixels were used to generate the line plots below. The images at the sides of the images show the area around the orange and magenta line.
Bottom: Line plot of the pixels marked in the images above. The plot shows the values of 200 pixels parallel to the vertical axis. The values are normalized with the mean intensity of the selected pixels.

The reduction of shadowing results in a larger area of high visibility (see [Sch16]). Therefore, the visibility maps of the moiré patterns are compared in this section. As shot-to-shot fluctuations appears at the PHELIX facility, shot 38 is chosen, a reference frame with a good mean visibility. For the laboratory measurement, the x-ray tube was set to the microfocus mode, an acceleration voltage of 45 kVp set and a power of 4 W adjusted. Nine frames are acquired with an exposure time of 5 seconds per frame. To avoid any influences due to geometrical effects or different moiré periods, the relative positions of the grating G_2 are set to the same values for both measurements. Due to experimental reasons, the distance between the source and the detector was 943 ± 1 mm in the PHELIX facility and 947 ± 3 mm in the ECAP laboratory. The distance between the x-ray source and the G_1 grating was set to the same distances within the measurement precession. The upper half of Figure 5.3 shows the two reference frames. The image on the left displays the image acquired in the ECAP facility and the image on the right shows shot 38.
It can be seen that the laboratory measurement suffers from shadowing in the left half of the grating surface. In the image of shot 38 the shadowing is significantly lower. Still, the intensity decreases to the left side of the image. By comparing the appearance of both images, it is noticeable that the two images differ in their noise. This can be seen in the right zoom. The moiré fringes of shot 38 are not as sharp as the fringes of the laboratory measurement. To analyze the moiré pattern in a quantitative manner, two line plots are made. One shows the moiré pattern in an good illuminated area and the other in an area where shadowing is present. The positions are marked with orange and magenta lines in the image. The zooms at the left and at the right show the area around the chosen pixels. The line plots are shown in the lower half of Figure 5.3. The upper graph shows pixel values in the shadowed area. The lower graph depicts the pixel values of the good illuminated region. The horizontal axes indicate the vertical pixel position (from top to bottom). The vertical axes show the normalized intensity. For the normalization every pixel was scaled with the mean intensity value of the selected pixels. The blue line represents the values of shot 38 and the red line the values of the laboratory measurement. By analyzing the two intensity profiles in the upper plot, it can be seen that the relative intensity fluctuation for shot 38 is significantly larger compared to the laboratory measurement. At some points this fluctuation matches the moiré period. At other places no systematics can be recognized. The laboratory measurement shows no obvious systematic in the intensity fluctuation. For the magenta colored line the picture is different. The moiré pattern is clearly visible. Further, the relative amplitudes are in the same scale. Therefore, the reconstructed visibility values should be approximately the same.
At the left side of Figure 5.4, the reconstructed visibility map of the laboratory measurement can be seen and at the right side the map of shot 38. It can be seen that the right visibility map is more noisy compared to the left. Apart from that, the maps show a similar visibility distribution. The visibility is in both images low at the left side. A vertical stripe with

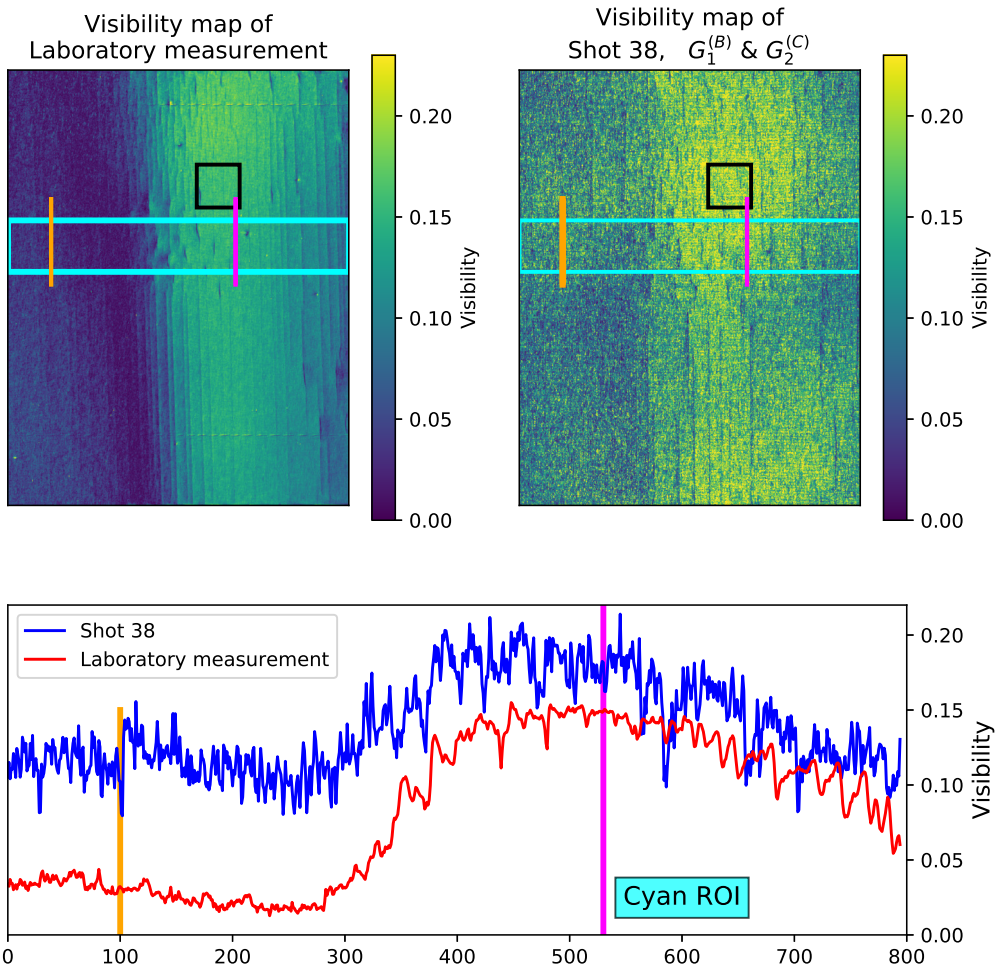

Fig. 5.4: Top: Calculated visibility map of the marked areas in Figure 5.3. The image on the left side shows the visibility map of the laboratory measurement. The right image shows the visibility map of shot 38. The orange and magenta lines depict the positions were the line plots in Figure 5.3 were generated.
Bottom: The line plot represents the arithmetic mean along the short side of the cyan RoI. The RoI spans the whole image horizontally and 120 pixels vertically.

higher visibility values is located right of the center. The visibility decreases at the far right again. By comparing both visibility maps with the naked eye, shot 38 seems to have higher visibility values compared to the laboratory measurement. To investigate this in a quantitative manner, the visibility is analyzed in two RoIs. A small black RoI and a elongated cyan RoI. In the black RoI the mean visibility, the standard deviation and the signal-to-noise ratio (SnR) is compared. Within the cyan RoIs, the visibility development is analyzed perpendicular to the vertically orientated grating bars. This comparison is displayed in Figure 5.4 below the two visibility maps. The line plot shows the mean visibility values along the short side of the RoI. Blue marks shot 38 and red the laboratory measurement. The horizontal axis indicate the position in the corresponding

images above, the vertical axis indicates the visibility. The standard deviation of the mean values is not shown, since the standard deviation is evaluated separately in the black Roi. By comparing the two graphs, it can be seen that the visibility of shot 38 seems to have an offset, compared to the laboratory measurement. This offset gets larger to the left side. Whereas, at the left side the visibility of the laboratory measurement almost vanishes, the visibility of shot 38 fluctuates around 0.1 . This results in approximately a factor of 5 higher visibility of shot 38.
The orange and magenta lines in the visibility maps and the line plot display the positions where the line plot of the intensity pattern is shown in Figure 5.3. At these points the visibility values of the moiré map can be compared with the expected values arising from the moiré pattern. In the line plot of the magenta line, see Figure 5.3, it can be clearly seen, that the amplitudes of the pattern are almost the same. Hence, the visibility values should be approximately the same. This is in good agreement with the mean visibility values shown in the line plot of Figure 5.4. There, the visibility values retrieved with the algorithm are approximately the same. In the laboratory measurement, no moiré pattern is observable in the zoomed area around the orange line. So, zero visibility is expected at this point in the visibility map. As mentioned, the line plot of the intensity at the orange line of shot 38 has a very noisy appearance, see Figure 5.3. A glance at the left zoomed area in the right image of Figure 5.3 shows, that a moiré pattern is present. But due the noise the moiré pattern has a very irregular appearance. Still, as a pattern is observable, a visibility will be retrieved along the line. These expectations are again compared with the mean visibilities shown in the line plot of Figure 5.4. At the position of the orange line, the visibility is ≈ 0.015 for the laboratory measurement and ≈ 0.10 for shot 38. Under consideration of the noise, the low visibility value for the laboratory matches well with the expected zero visibility. Same is valid for the visibility of shot 38. As expected, a non-vanishing mean visibility is retrieved which has high fluctuations from pixel to pixel due to the noisy moiré pattern from which it was reconstructed. A detailed analysis on the influence of photon flux and noise on the quality of reconstructed phase-contrast images acquired at the Phelix facility will be given in [Sch21] .
It should also be noted that it is difficult to reconstruct images in the area around the orange line of shot 38. Due to the high relative noise in this region, the moiré pattern will differ in this region significantly from shot to shot. Hence, it is tricky to evaluate whether the change in the moiré pattern is caused by an object or the noise. This means, that a high mean visibility does not necessarily indicate an area for good reconstruction especially when it is subjected to high fluctuations and noise.
As mentioned before, the standard deviation respectively the noise is analyzed in the black Roi. Therefore, the area was chosen that the visibility values appear almost constant. This ensures that the calculated standard deviation results only from noise in the visibility.

A measure that quantifies the noise of a signal is the so-called signal-to-noise ratio (SNR). It is given according to [Buz11] by

$$\text{SNR} = \frac{\mu}{\sigma}, \tag{5.1}$$

with μ as the signal mean value and σ the standard deviation. A high SNR value means that the signal is large compared to the noise. Small values, on the other hand, indicate a large noise compared to the signal. This means for the visibility, that large SNR values indicate a constant moiré period, whereas small SNR values indicate large fluctuations in the moiré pattern. Thus, during selecting regions for image reconstruction, it is worth taking the SNR value into account.
The mean visibility, the standard deviation and the SNR is displayed in Table 5.1. The tabulated values confirm the visual impression. The mean visibility of shot 38 is higher compared to the visibiliy of the laboratory measurement. But the standard deviation is higher by a factor of approximately 4. As the mean visibility differs only slightly, the SNR value for shot 38 is significantly smaller by the factor of approximately 3.

	Visibility of black ROI		
	mean	std.	SNR
Laboratory measurement	0.155	0.014	11.1
Shot 38	0.197	0.055	3.6

Tab. 5.1: Mean visibility, standard deviation and SNR values of the moiré pattern within the black ROI, framed in Figure 4.14.

This comparison showed, that visibility maps which are reconstructed from noisy measurements should be interpreted with care. At the right side of the grating, where the illumination is uniformly, the reconstructed visibility values were in the right scale. At the left side of the gratings the visibility values were overestimated due to the noise.
So, in the area left of center the actual visibility is still low for the measurements performed at the PHELIX facility. Nevertheless, on the outer left edge of shot 38 in Figure 5.3 a moiré pattern can be seen, where in the laboratory measurement no pattern is visible. This means, the shadowing was at the PHELIX facility lower as in the laboratory measurement. One possible explanation is that the waver changed its shape due to mechanical stress, caused by the vacuum at the PHELIX facility or vibrations or thermal fluctuations. This effect could also explain the increasing amount of vertical cracks in the grating surface of the $G_2^{(C)}$ (Compare in Figure 5.3 Shot 38 form Feb. 2020 and Laboratory measurement from Oct. 2020).

5.3 Backlighter measurements

Finally, reconstructed transmission and Dpc images from backlighter measurements are presented and analyzed. The hole target was chosen as a test sample. The reconstructed images will be evaluated qualitatively. A direct comparison with laboratory measurements is not performed. This is based on the fact that due to the different x-ray spectra, different phase shifts and transmission will occur. In addition to that, Ips were used at the Phelix facility. As no Ip scanner is available in the x-ray laboratories of the Ecap facility, a digital detector has to be used. Hence, a quantitative comparison is even more difficult.

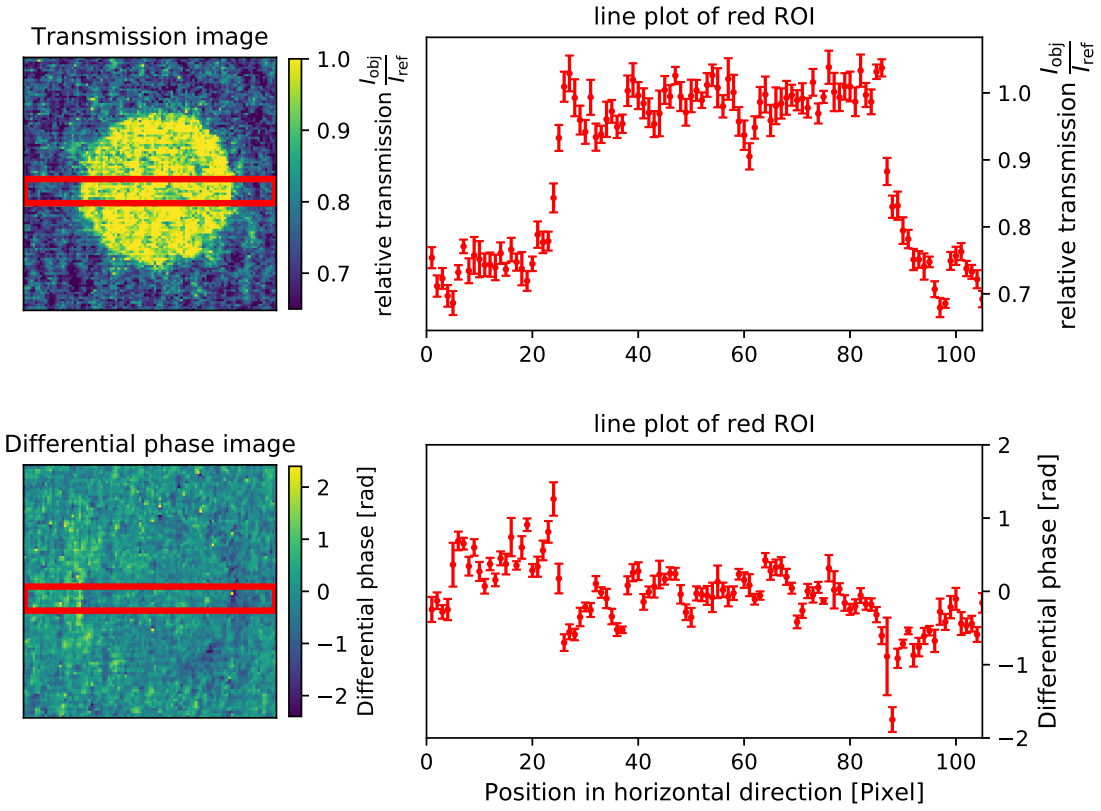

Fig. 5.5: Left: Reconstructed transmission image (top) and Dpc image (bottom) of the hole target (see section 4.3). The image are reconstructed using shot 46 (reference) and shot 42 (object) of the manual setup (see section 3.1).
Right: The line plot shows the mean values along the short side of the Roi. The error bars indicate the standard error. The used Roi spans the whole image horizontally and 10 pixels vertically.

The manual setup was used for the measurements (see section 3.1). The grating combination $G_1^{(A)}$, $G_2^{(B)}$ was mounted and a moiré period of 9 ppp adjusted. The reference frame was acquired at shot 46 and the object frame at shot 42. The evaluation of the reconstructed images is performed as explained in section 4.5. At first, the appearance of the reconstructed image is assessed followed by the examination of a Roi using a line plot. So, the overall

shape can be qualitatively compared with the laboratory measurements of section 4.5. On the left side of Figure 5.5 the reconstructed images are depicted. The transmission image can be seen above and the Dpc image below. The red frame indicates which pixels are used to generate the line plot on the right. The horizontal axis of the line plots indicates the position in the corresponding image on the left. The vertical axis of the upper line plot shows the relative transmission, the vertical axis of the lower line plot the differential phase. The markers show the arithmetic mean of the vertical Pixel values. The errorbars represent the standard error.
In the transmission image, the chosen Roi shows one hole of the hole target. The hole and the surrounding material show a constant intensity. The inner area of the hole has a relative transmission of approximately one. Outside the hole, the relative transmission decreases by $\approx 30\,\%$. The edge of the hole is clearly visible. Similar to the reconstructed visibility map (see Figure 5.4), the image is noisy. By taking a look at the transmission images in Figure 4.15 on page 65, it can be seen, that the appearance of the retrieved transmission images of the holes match well, apart of the noise. The same holds for the line plot on the right side. As discussed in section 4.3, an artificial frequency, imprinted onto the signal, is visible.
In the Dpc image the edges of the circle are not clearly visible. The differential phase signal almost vanishes at the top and bottom of the hole. To the left and to the right, the differential phase is more apparent. The line plot on the right side confirms this impression. The two edges of the hole are clearly visible in the differential phase. Comparing this with Figure 4.16 on page 67, it is apparent that overall shape of the line plot matches well with the laboratory measurements. Only in the laboratory Dpc image, the edges can be seen slightly better.
These reconstructed images and the qualitative comparison carried out here show that with this setup very similar and comparable images can be reconstructed for measurements performed at a backlighter source.

6 Conclusion

Core of this thesis was the design of a portable interferometer. This interferometer was used successfully during the beam time at the PHELIX facility. It was shown that the interferometer is highly precise as well as sturdy. This makes the portable interferometer reliable.

Besides these qualities of the interferometer, care was taken that it can be used in a wide field of applications. The realized detector mounting method allows an easy and quick change between different digital x-ray detectors and imaging plates. This is of particular advantage if different detectors are used. The large sample stage allows a precise placement of various target setups due to the hole grid and the large area. The bracket design of the grating mount enables a flexible adjustment to fit the measures of the present and previously used grating frames. This allows old and new gratings to be easily installed in the interferometer.

For the beam time at the PHELIX facility, eight grating combinations were available. During the characterization process of the interferometer, a systematic routine was applied and refined to assess the quality of the grating combination. This process included the acquisition of moiré maps, which could be used later for evaluating the positioning precision of the interferometer. Furthermore, the visibility of the moiré pattern depending on the G_2 position of a fixed moiré period was investigated. It was observed that for negative tilts of the G_2 grating the visibility is systematically higher, compared to positive tilts.

Two different image reconstruction methods for moiré imaging are available, one published by Takeda in 1982 [TIK82] and one modified version published by Seifert in 2018 [SGL+18]. Investigating these methods, it appeared that short moiré periods are preferable for both reconstruction algorithms. The newer method leads to sharper reconstructed images for the investigated target. Subsequently, the newer method was used.

Applying the portable interferometer at the PHELIX beam time showed that the mechanical requirements were met. Transporting and installing the interferometer only caused a minimal misalignment, which could be easily corrected with the fast alignment method. Additionally, the successful change of the gratings during the experimental phase must be emphasized at this point. Already the first backlighter shot after changing the grating set could be used as an reference frame for moiré imaging. In preparation for the change, the grating combination was aligned in the ECAP facility and the corresponding positions saved.

The ability of changing the gratings promises advantages. A conceivable application would be to prepare two sets of gratings with different design energies. This allows to use different backlighter target wires, for example. Due to their different characteristic x-ray spectra the

phase shift and attenuation of the object will differ. This will help to further improve the retrieved phase shift and thus the electron density distribution of the investigated target.

Acknowledgments

Finally, I would like to thank all those who supported me during my master thesis. My special thanks goes to

- Prof. Dr. Gisela Anton for the assignment of this thesis and giving me scientific input for the experiments.
- my supervisors Bernhard Akstaller and Max Schuster who answered all my questions personally and via Zoom, guided me through each stage of the thesis and gave me one or another lesson in programming.
- Andreas Wolf, Fabian Hoffman and Veronika Ludwig for their steady patience and availability to answer my questions.
- Andreas Wolf, Bernhard Akstaller, Elise Pongratz, Martin Schreiner and Max Schuster for proofreading this thesis.
- the whole Laboratory Astrophysics & Phase-Contrast Imaging group for a relaxed, friendly and productive atmosphere at the Ecap and Phelix facility.
- Martin Schreiner who worked with me to convert my handmade drawings of the interferometers into Cad models and provided me with very nice renderings of the interferometer.
- the entire crew of the mechanical workshop who manufactured the interferometer.
- Alfred Kaluza and Henry Schott who built the transport boxes and x-ray shielding of the interferometers in a spontaneous effort.
- Dr. Pascal Meyer from the Karlsruhe Nano Micro facility who fabricated and provided the investigated gratings.
- Dr. Paul Neumayer from the Gsi institute who answered all my questions concerning the Phelix facility and the plasma physics which raised during the beam time.
- my parents, who financed my entire studies.
- My family and my girlfriend, who are always at my side and helped me with words and deeds.

Without your efforts this thesis would not be available in this quality.

A Appendix

Additional plots

Phase shift of the G_1 phase grating

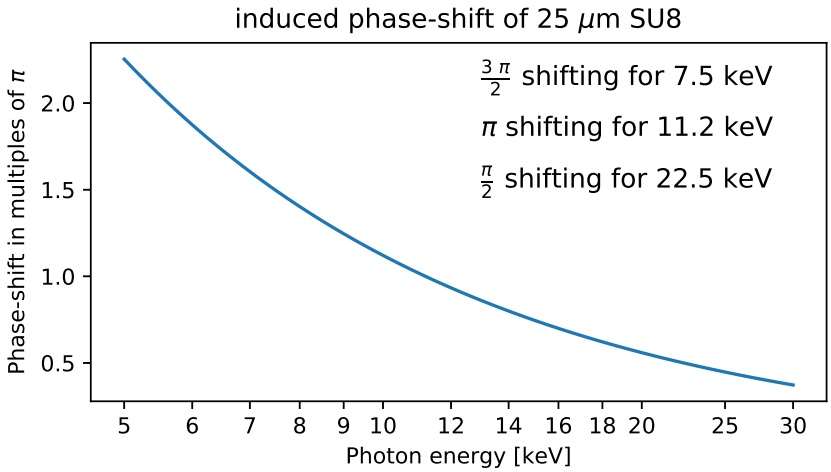

Fig. A.1: Phase shift induced from the grating G_1.

The plot in Figure A.1 shows the induced phase-shift of the used G_1 grating. The chemical constitution of the used material was provided by the manufacturer. The SU-8 photoresist, which was used for the grating consist of

$$5\%\ C_4H_6O_2$$
$$95\%\ C_{87}H_{98}O_{16}$$

and has got a density of $1.25\,\frac{\mathrm{g}}{\mathrm{cm}^3}$. The phase shift was calculated using Equation 2.11, which reads

$$\Delta\varphi = -\frac{2\pi}{\lambda}\delta(\lambda)\cdot d.$$

With the photon wavelength λ, the refractive index decrement $\delta(\lambda)$ and the grating height $d = 25\,\mu\mathrm{m}$. The values for the refractive index decrement $\delta(\lambda)$ were taken from [HGD93].

Transmission of different covering materials for the Ips

The plot in Figure A.2 shows the wavelength dependent absorbing behavior of possible covering materials for the imaging plates. A 0.5 mm thick PMMA sheet is compared with a 0.0008 mm Aluminum foil. The used foil was purchased at Kroff in Swiss and fabricated from alloy 8079. The values for calculating the transmissions taken from [HGD93].

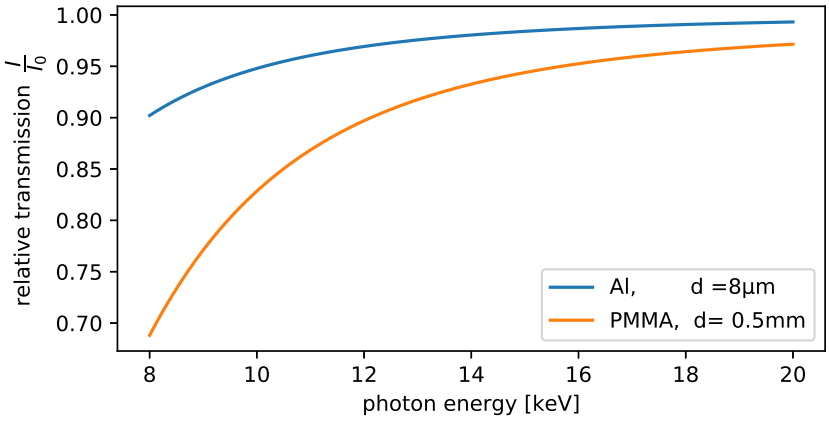

Fig. A.2: Energy dependent transmission of x-ray through different matter.

Transmission of used shielding material

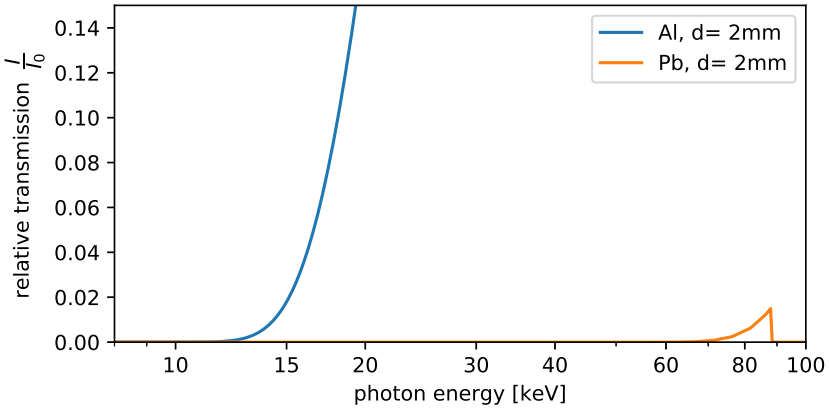

Fig. A.3: Energy dependent transmission of x-ray through different matter.

The plot in Figure A.3 shows the energy dependent relative absorption of the used shielding material. The mass attenuation coefficients for aluminum were taken from [HGD93], the values for the lead from [Cha00]. A density of 2.7 $\frac{\text{g}}{\text{cm}^3}$ for aluminum and 11.34 $\frac{\text{g}}{\text{cm}^3}$ for lead was assumed.

Bar chart of Visibility for selection of the grating combination

The visibility values were manually determined using Equation 2.24. The required values were calculated by taking the average of four maxima and minima, respectively. To increase the clarity, the error bars have been omitted.

(a)

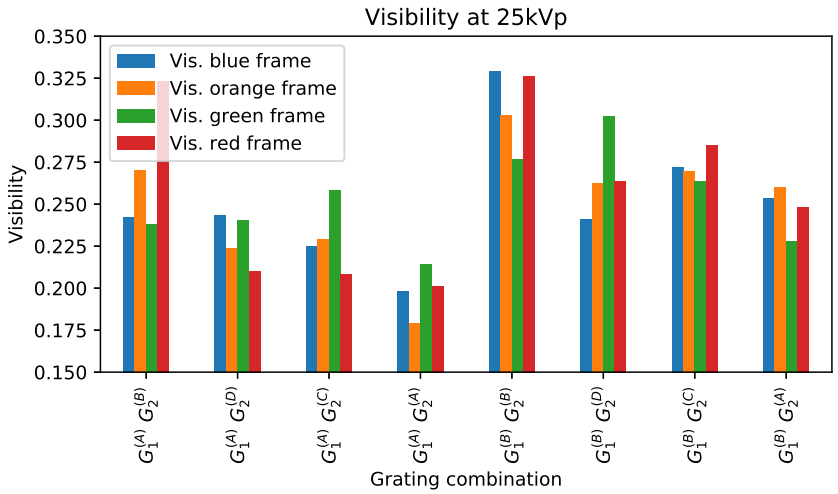

(b)

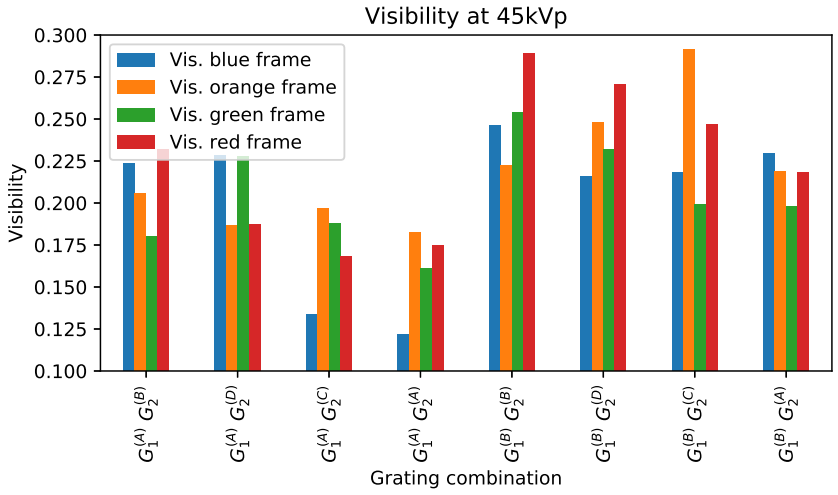

Fig. A.4: Bar chart of the visibility of the colored reference frames in Figure 4.1. The colors of the bars match the frames in the moiré map. The acceleration voltage is for (a) 25 kVp and for (b) 45 kVp.

Fourier spectra, masked with the new method

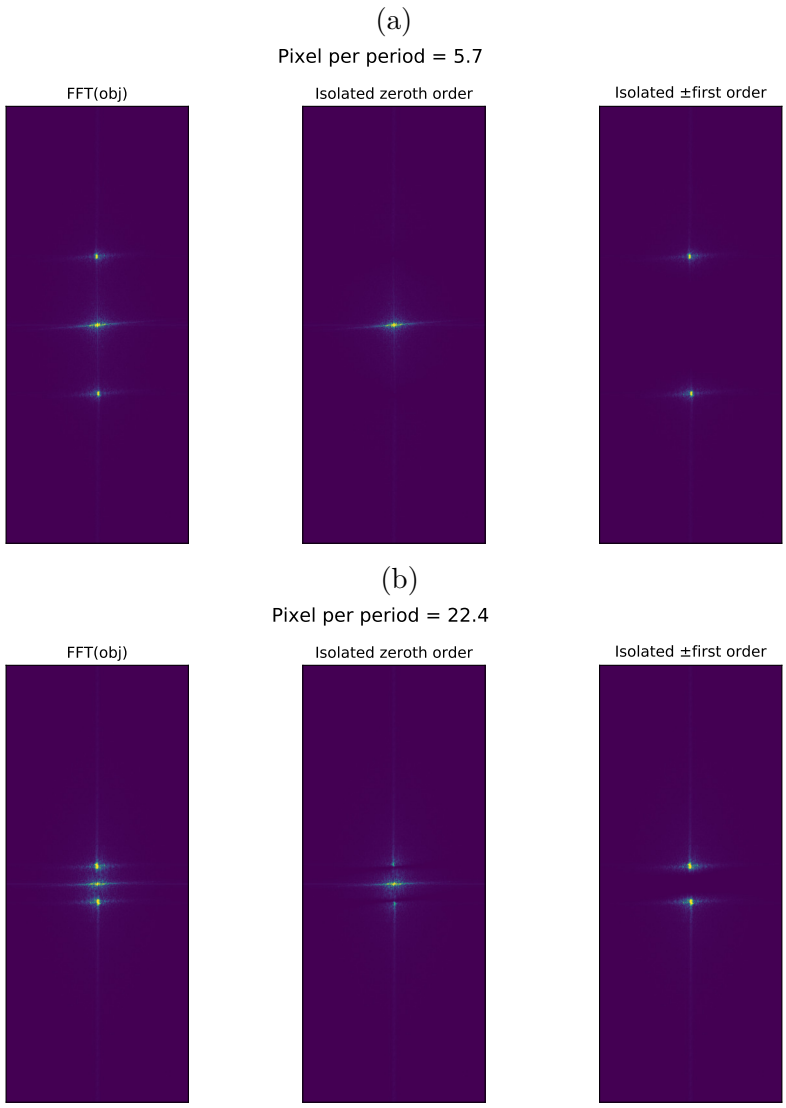

Fig. A.5: Visualization of the Fourier spectra and the masked areas used to generate the thee image modalities. (a) shows the spectra of a reference frame with a moiré period of 5.7 ppp. (b) shows the spectra of a reference frame with 22.4 ppp. The first column shows the full spectra. The second the isolated zeroth order and the third column the isolated first order peaks.

Additional Tables

Specs of the linear stages

The tabulated values are taken from the manufacturer's data sheets. They are linked in the corresponding name, or can be found on the manufacturer's website.

	Horizontal linear actor	vertical linear actor
Name	VT-80 50 PK245 MLS 10-6	VT-80 25 PK245 MLS 10-6
manufacturer	Physik Instrumente	Physik Instrumente
model	6230V62000	6230V61000
travel range [mm]	50	25
design resolution [µm]	5	5
mimimum incremental motion [µm]	0.2	0.2
unidirectional repeatability [µm]	0.4	0.4
bidirectional repeatability [µm]	±10	±10
vacuum suitability [mBar]	10^{-6}	10^{-6}

Tab. A.1: Overview over the motorized linear stage parameters. The linear stage is driven by a step motor. The stages only differ in their length.

	Horizontal linear actor	vertical linear actor
Name	LT-60	MT-60
manufacturer	owis	owis
Model	31.064.1031.V6	31.063.1581.V6
Travel range [mm]	100	15
spindle pitch [mm]	1	
graduation of scale [µm]	10	5
tilting moment [Nm]	10	9
setting sensity [µm]		1

Tab. A.2: Overview over the manual linear stage parameters. The horizontal linear actor has got no scale, as it is a linear stage. The vertical linear actor is a measuring stage and thus has got a scale.

List of investigated gratings and their specification

	G_1 phase gratings		G_2 absorption gratings			
alias name	$G_1^{(A)}$	$G_1^{(B)}$	$G_2^{(A)}$	$G_2^{(B)}$	$G_2^{(C)}$	$G_2^{(D)}$
fabrication name	1929	8078	G03	1626	8077	4169
thickness waver [µm]	500	500	500	500	500	400
waver material	Polyimide		graphite	graphite	conductive varnish (Vespel)	graphite
material grating bars	SU-8	SU-8	gold	gold	gold	gold
grating height [µm]	25	25	150	150	150	> 150
period [µm]	10	10	6	6	6	6
shape active area [mm]	rectangular, 50×50		rectangular, 45×70	round, $d = 70$		
duty cycle	0.5	0.5	0.55-0.6	0.55-0.6	0.55-0.6	0.55-0.6
special characteristics			cloud appearance of moiré, partly defect grating surface	strong cloud appearance of moiré	cracks in grating structure parallel to grating bars	cloud appearance of moiré, wavy thickness

Tab. A.3: Table of all known parameters of the investigated gratings. All G_2 gratings were not stripped. This means that the gaps between the golden grating bars are filled with photo resist.

Visibility values of marked measurement point in Figure 4.14

Visibility	Pink framed point		Blue framed point	
	mean	std.	mean	std.
Green area	0.1580	0.0135	0.1384	0.0123
Cyan area	0.1577	0.0141	0.1449	0.0130
Red area	0.1582	0.0141	0.1460	0.0130

Tab. A.4: Mean visibility and standard deviation values of the moiré pattern within the RoI of the measurement points framed in Figure 4.14.

The standard error of the visibility is not stated for two reasons. The RoI spans 89×76 pixels. A standard error, calculated by $\sigma/\sqrt{\#\text{Pixels}}$ would vanish. Further, the visibility is not constant over the whole RoI. An error indication would suggest that the visibility is constant.

Bibliography

[Ami09] Amidror, Isaac: The Theory of the Moiré Phenomenon. Springer-Verlag GmbH, 2009. – ISBN 9781848821811

[BAB+10] Bagnoud, Vincent ; Aurand, B ; Blazevic, A ; Borneis, S ; Bruske, C ; Ecker, B ; Eisenbarth, U ; Fils, J ; Frank, A ; Gaul, E u. a.: Commissioning and early experiments of the PHELIX facility. In: Applied Physics B 100 (2010), Nr. 1, S. 137–150

[BH65] Bonse, UetMHART ; Hart, M: An X-ray interferometer. In: Applied Physics Letters 6 (1965), Nr. 8, S. 155–156

[BK96] Berry, M. V. ; Klein, S.: Integer, fractional and fractal Talbot effects. In: Journal of Modern Optics 43 (1996), Nr. 10, 2139-2164. http://dx.doi.org/10.1080/09500349608232876. – DOI 10.1080/09500349608232876

[BKSW10] Bennett, E ; Kopace, R ; Stein, A ; Wen, H: A grating-based single-shot x-ray phase contrast and diffraction method for in vivo imaging. In: In: Medical Physics 37 (2010), Nr. 11, S. 6047–6054. http://dx.doi.org/10.1118/1.3501311.-DOI10.1118/1.3501311. – DOI 10.1118/1.3501311.–DOI10.1118/1.3501311

[Buz11] Buzug, Thorsten M.: Computed tomography. In: Springer Handbook of Medical Technology. Springer, 2011, S. 311–342

[BZL+12] Bevins, N ; Zambelli, J ; Li, K ; Qi, Z ; Chen, G.-H: Multicontrast x-ray computed tomography imaging using Talbot-Lau interferometry withoutphase stepping. In: Medical Physics 39 (2012), Nr. 1, S. 424–428. http://dx.doi.org/10.1118/1.3672163.-DOI10.1118/1.3672163. – DOI 10.1118/1.3672163.–DOI10.1118/1.3672163

[CGM+97] Cloetens, P ; Guigay, J ; Martino, C ; Baruchel, J ; Schlenker, M: Fractional Talbot imaging of phase gratings with hard x rays. In: Opt. Lett 22 (1997), S. 1059–1061

[Cha00] Chantler, C. T.: Detailed Tabulation of Atomic Form Factors, Photoelectric Absorption and Scattering Cross Section, and Mass Attenuation Coefficients in the Vicinity of Absorption Edges in the Soft X-Ray (Z=30–36, Z=60–89, E=0.1 keV–10 keV), Addressing Convergence Issues of Earlier Work. In: Journal of Physical and Chemical Reference Data 29 (2000), Nr. 4, 597-1056. http://dx.doi.org/10.1063/1.1321055. – DOI 10.1063/1.1321055

[DBC12] Diemoz, PC ; Bravin, A ; Coan, P: Theoretical comparison of three X-ray phase-contrast imaging techniques: propagation-based imaging, analyzer-based imaging and grating interferometry. In: Optics express 20 (2012), Nr. 3, S. 2789–2805

[Dem18] Demtröder, Wolfgang: Experimentalphysik 2. Springer-Verlag GmbH, 2018 https://www.ebook.de/de/product/31029958/wolfgang_demtroeder_experimentalphysik_2.html. – ISBN 3662557894

[Die19] Dietrich, Lisa: Entwicklung und Charakterisierung vonTestobjekten für die Phasenkontraströntgenbildgebung. 2019

[DM11] Des Mcmorrow, Jens Als-Nielsen: Elements of Modern X-Ray Physics. WILEY, 2011 https://www.ebook.de/de/product/14773530/des_mcmorrow_jens_als_nielsen_elements_of_modern_x_ray_physics.html. – ISBN 0470973943

[EBS+07] Engelhardt, Martin ; Baumann, Joachim ; Schuster, Manfred ; Kottler, Christian ; Pfeiffer, Franz ; Bunk, Oliver ; David, Christian: High-resolution differential phase contrast imaging using a magnifying projection geometry with a microfocus x-ray source. In: Applied Physics Letters 90 (2007), Nr. 22, 224101. http://dx.doi.org/10.1063/1.2743928. – DOI 10.1063/1.2743928

[FMMS12] Fiksel, G ; Marshall, FJ ; Mileham, C ; Stoeckl, C: Note: Spatial resolution of Fuji BAS-TR and BAS-SR imaging plates. In: Review of Scientific Instruments 83 (2012), Nr. 8, S. 086103

[FRS04] Foord, ME ; Reisman, DB ; Springer, PT: Determining the equation-of-state isentrope in an isochoric heated plasma. In: Review of scientific instruments 75 (2004), Nr. 8, S. 2586–2589

[Gö20] Götte, Stefan ; GSI Helmholtzzentrum für Schwerionenforschung GmbH (Hrsg.): PHELIX laser facility. https://www.gsi.de/en/work/research/appamml/plasma_physicsphelix/phelix.htm. Version: 2020. – Accessed Oct. 20, 2020

[Gal17] Gallersdörfer, Michael: Untersuchungen zur Nutzung des Moiré-Effektes für die gitterbasierte Phasenkontrast-Röntgenbildgebung, Masters Thesis, 2017

[HG09] Hügel, Helmut ; Graf, Thomas: Laser in der Fertigung. Bd. 2. Springer, 2009

[HGD93] In: Henke, B ; Gullikson, E ; Davis, J: X-ray interactions: photoabsorption, scattering, transmission, and reflection at E=50-30000 eV. 1993, 181–342

[Hof18] Hofmann, Fabian: Modeling and Correcting Moiré Artifacts in Grating-Based Phase-Contrast X-Ray Imaging, Masters Thesis, 2018

[Imaa] Imaging, Teledyne R.: Scintillator Options for Shad-o-Box Cameras, `https://www.teledynedalsa.com/en/products/imaging/industrial-x-ray/shad-o-box-hs/`. – Accessed Oct. 25, 2020

[Imab] Imaging, Teledyne R. ; Teledyne Digital Imaging US, Inc. A B. o. (Hrsg.): Shad-o-Box HS Product Family Datasheet. `https://www.teledynedalsa.com/en/products/imaging/industrial-x-ray/shad-o-box-hs/`. – Accessed Oct. 25, 2020

[Kev97] Kevles, Bettyann: Naked to the bone: medical imaging in the twentieth century. Rutgers University Press, 1997

[LSH+19] Ludwig, Veronika ; Seifert, Maria ; Hauke, Christian ; Hellbach, Katharina ; Horn, Florian ; Pelzer, Georg ; Radicke, Marcus ; Rieger, Jens ; Sutter, Sven-Martin ; Michel, Thilo ; Anton, Gisela: Exploration of different x-ray Talbot–Lau setups for dark-field lung imaging examined in a porcine lung. In: Physics in Medicine & Biology 64 (2019), mar, Nr. 6, 065013. `http://dx.doi.org/10.1088/1361-6560/ab051c`. – DOI 10.1088/1361–6560/ab051c

[Lud20] Ludwig, Veronika: Development of image acquisition andalignment methods for X-ray dark-fieldand phase-contrast imaging, Diss., 2020

[Mes15] Meschede, Dieter: Gerthsen physik. Springer-Verlag, 2015

[MMD+09] Marshall, FJ ; McKenty, PW ; Delettrez, JA ; Epstein, R ; Knauer, JP ; Smalyuk, VA ; Frenje, JA ; Li, CK ; Petrasso, RD ; Séguin, FH u. a.: Plasma-density determination from x-ray radiography of laser-driven spherical implosions. In: Physical review letters 102 (2009), Nr. 18, S. 185004

[MPR+11] Maddox, BR ; Park, HS ; Remington, BA ; Izumi, N ; Chen, S ; Chen, C ; Kimminau, G ; Ali, Z ; Haugh, MJ ; Ma, Q: High-energy x-ray backlighter spectrum measurements using calibrated image plates. In: Review of Scientific Instruments 82 (2011), Nr. 2, S. 023111

[NRE+09] Neumayer, P ; Rosmej, ON ; Ecker, B ; Hochhaus, D ; Zielbauer, B ; Aurand, B ; Kazakov, E ; Kühl, Th ; Stöhlker, Th: K-alpha backlighter optimization using high-energy picosecond laser pulses in experiments at the PHELIX laser facility. (2009)

[Pag06] Paganin, David: Coherent x-ray optics. Oxford New York : Oxford University Press, 2006. – ISBN 9780198567288

[Phy20] Physik Instrumente (PI) GmbH & Co. KG: Linear Stages 3D Model. Version: 2020. https://www.physikinstrumente.de/de/ Accessed Aug. 08, 2020

[Ray81] Rayleigh, John William S.: XXV. On copying diffraction-gratings, and on some phenomena connected therewith. 11 (1881), Nr. 67, 196-205. http://dx.doi.org/10.1080/14786448108626995. – DOI 10.1080/14786448108626995

[Rie17] Rieger, Jens: Experimentelle uns simulative Untersuchungen in der Talbot-Lau Röntgenbildgebund und ihre Anwendung in der Mammographie, Diss., 2017

[Rön96] Röntgen, Wilhelm C.: On a new kind of rays. In: Science 3 (1896), Nr. 59, S. 227–231

[Saf20] Saffer, Julian: X-Ray Phase-Contrast Imaging ofLaser-Driven Plasma Shocks, Masters Thesis, 2020

[Sch16] Schuster, Max: Design und Charakterisierung eines Talbot-Interferometers mit Mikrofokus-Röntgenröhre, Masters Thesis, 2016

[Sch21] Schuster, Max: Dissertation. 2021

[Sei20] Seifert, Maria: X-ray phase-contrast and dark-fieldimaging in single-shot and scanningmode, Diss., 2020

[SGH+17] Seifert, M. ; Gallersdörfer, M. ; Horn, Florian ; Ludwig, V. ; Schuster, M. ; Pelzer, G. ; Rieger, Jens ; Michel, Tissot ; Anton, G.: Measurement and simulative proof concerning the visibility loss in x-ray Talbot-Lau Moiré imaging. In: Journal of Instrumentation (2017)

[SGL+18] Seifert, Maria ; Gallersdörfer, Michael ; Ludwig, Veronika ; Schuster, Max ; Horn, Florian ; Pelzer, Georg ; Rieger, Jens ; Michel, Thilo ; Anton, Gisela: Improved Reconstruction Technique for Moiré Imaging Using an X-Ray Phase-Contrast Talbot–Lau Interferometer. In: Journal of Imaging 4 (2018), Nr. 5, S. 62

[SLA+19] Schuster, Max ; Ludwig, Veronika ; Akstaller, Bernhard ; Seifert, Maria ; Wolf, Andreas ; Michel, Thilo ; Neumayer, P. ; Funk, Stefan ; Anton, Gisela: A fast alignment method for grating-based X-ray phase-contrast imaging systems. In: Journal of Instrumentation 14

(2019). http://dx.doi.org/10.1088/1748-0221/14/08/P08003. – DOI 10.1088/1748–0221/14/08/P08003. – CRIS-Team Scopus Importer:2019-10-08

[Sul97] Suleski, Thomas J.: Generation of Lohmann images from binary-phase Talbot array illuminators. In: Applied Optics 36 (1997), Jul, Nr. 20, 4686–4691. http://dx.doi.org/10.1364/AO.36.004686. – DOI 10.1364/AO.36.004686

[SWC+] Seifert, M ; Weule, M. ; Cipiccia, S. ; Flenner ; Hagemann, S. ; J. ; Ludwig, V. ; Michel, T. ; Neumayer, P. ; Schuster, M. ; Wolf, A. ; Anton, G. ; Funk, S. ; Akstaller, B.: Evaluation of the Weighted Mean X-ray Energy for an Imaging System Via Propagation-Based Phase-Contrast Imaging. http://dx.doi.org/10.3390/jimaging6070063. – DOI 10.3390/jimaging6070063

[THH+11] Tommasini, R ; Hatchett, SP ; Hey, DS ; Iglesias, C ; Izumi, N ; Koch, JA ; Landen, OL ; MacKinnon, AJ ; Sorce, C ; Delettrez, JA u. a.: Development of Compton radiography of inertial confinement fusion implosions. In: Physics of Plasmas 18 (2011), Nr. 5, S. 056309

[Tho20] Thorlabs, Inc.: Smooth Bore Kinematic Mirror Mounts with Two Adjusters. https://www.thorlabs.com/newgrouppage9.cfm?objectgroup_id=1492. Version: 2020. – Accessed Aug. 06, 2020

[TIK82] Takeda, Mitsuo ; Ina, Hideki ; Kobayashi, Seiji: Fourier-transform method of fringe-pattern analysis for computer-based topography and interferometry. In: Journal of the Optical Society of America 72 (1982), Jan, Nr. 1, 156–160. http://dx.doi.org/10.1364/JOSA.72.000156. – DOI 10.1364/JOSA.72.000156

[TV09] Thompson, Albert C. ; Vaughan, Douglas: X-ray data booklet. Lawrence Berkeley National Laboratory, University of California Berkeley, CA, 2009 (3)

[WDD+] Weitkamp, Timm ; Diaz, Ana ; David, Christian ; Pfeiffer, Franz ; Stampanoni, Marco ; Cloetens, Peter ; Ziegler, Eric: X-ray phase imaging with a grating interferometer. http://dx.doi.org/10.1364/OPEX.13.006296. – DOI 10.1364/OPEX.13.006296

[WGLC] Wuhan Golden Laser Co., Ltd. ; Wuhan Golden Laser Co., Ltd. (Hrsg.): 6000W 8000W Fiber Laser Cutting Machine. https://www.goldenlaser.cc/6000w-8000w-fiber-laser-cutting-machine.html#panel4d. – Accessed Oct. 22, 2020

[Wol16] Wolf, Andreas: Untersuchungen zu einer iterativen CT-Rekonstruktion in der gitterbasierten Röntgenbildgebung, Masters Thesis, 2016

[XRL20] XRF Research, Inc (Hrsg.): XRF Spectra. http://www.xrfresearch.com/?s=pb. Version: 2020. – Accessed Aug. 06, 2020

[YL15] Yan, Aimin ; Liu, Xizeng Wu H.: A general theory of interference fringes in x-ray phase grating imaging. In: Medical physics 42 (2015), Nr. 6, S. 3036–3047

[YXL] YXLON International GmbH ; COMET Group (Hrsg.): YXLON FXEMicrofocus X-ray systems. https://peltecndt.com/wp-content/uploads/2020/06/Gamme-Tubes_FXE_EN1.pdf. – Accessed Nov. 01, 2020

[Zan13] Zang, Andrea: Uber die Erkennbarkeit fein verteiltenMikrokalks in der interferometrischenMammographie, Masters Thesis, 2013

[Zie20] Zielbauer, Bernhard ; GSI Helmholtzzentrum für Schwerionenforschung GmbH (Hrsg.): Petawatt target area. https://www.gsi.de/en/work/research/appamml/plasma_physicsphelix/phelix/phelix_pw_target_area.htm. Version: 2020. – Accessed Jun. 23, 2020

Erklärung

Hiermit bestätige ich feierlich, dass ich diese Arbeit selbstständig und nur unter Verwendung der angegebenen Hilfsmittel und Quellen angefertigt habe.

Nürnberg, den 01.11.2020

Stephan Schreiner